# Seamless Integration of Renewable Generation and Plug-in Electric Vehicles into the Electrical Grid

by

Soumya Kundu

A dissertation submitted in partial fulfillment
of the requirements for the degree of
Doctor of Philosophy
(Electrical Engineering: Systems)
in The University of Michigan
2013

Doctoral Committee:

Professor Ian A. Hiskens, Chair
Professor Jessy W. Grizzle
Professor Jeffrey L. Stein
Professor Duncan S. Callaway, UC Berkeley

© Soumya Kundu 2013

All Rights Reserved

To my family - Maa, Baba and Jit.

# ACKNOWLEDGEMENTS

Writing this section has been the most difficult job for me in this whole dissertation. How can I possibly express my true gratitude to those who have walked alongside me in the past couple of years and shared my moments of despair and delight? But I must try.

It has been a truly great experience here at University of Michigan, Ann Arbor. I never quite realized how fast these three years and eight months passed by. The studies, research and the life - the enjoyment has been to the fullest! I would like to thank all my professors, fellow grad students and the staff for their invaluable advice and ever-present support. Thanks to all my friends for making my stay here such a memorable experience! I enjoyed discussing topics ranging from homework assignments to recent global issues on power systems to hiking plans for summer to best dining places in AA to cricket (of course). I'll miss you all. A special thanks to Ms. Becky Turanski (Grad Student Coordinator, EE: Systems) for always being there with solutions to my problems, no matter how complicated those were!

When I first came here at Ann Arbor, I was apprehensive of how (or if ever) I was going to finish my PhD, which is often assigned (un-)deserved abbreviations such as Permanent Head Damage or Prepared for Happy Death. Looking back, I realize how very fortunate I was in having Professor Ian Hiskens as my PhD supervisor. It was such an excellent opportunity to learn from him the nuances of power systems and control. I loved working with him on some of the most fascinating research topics related to today's global energy crisis. He has been (and will continue to be) a 'mentor' in the truest sense. Thanks to Ian, I now know whom to look up to if I ever become a PhD supervisor myself! I would also like to thank all the nice people I had a chance to collaborate with, through the scope of the National Science Foundation's EFRI-RESIN project, and over the couple of summers I spent at CNLS, Los Alamos National Laboratory.

Now a few words on the greatest of all gifts, my family. I would not even try to put into words how important their role has been in the successful completion of my dissertation (and in my life), because no matter what or how much I write it all seems lame. But I would like to take this opportunity to thank my parents for teaching us (me and my brother) how to dream, and to make sincere efforts in the pursue of it, and for pulling us back up whenever we seemed to falter! Thanks for all the invaluable lessons I have learnt from them (and those that I am yet to learn - I 'promise' I will be punctual and I will not speed!). And, finally, the thing that I miss the most away from home - all those passionate debates with my talented younger brother (a scary statistician) on topics apparently fetched from some abstract faraway world, having no apparent day-to-day consequences, which usually end only with Maa's call for a delicious dinner!

Before I end this section, I must fulfill the promise I made to my friends sometime back. I thank MATLAB®, my awesome on-the-laptop laboratory, and all the excellent people behind the creation and maintenance of the vast set of engineering and mathematical tools available in it! This dissertation would have been a much harder job without them.

# TABLE OF CONTENTS

**CHAPTER**

# LIST OF FIGURES

**Figure**

# LIST OF TABLES

**Table**

# LIST OF APPENDICES

**Appendix**

# ABSTRACT

Seamless Integration of Renewable Generation and Plug-in Electric Vehicles into the Electrical Grid
by
Soumya Kundu

Chair: Professor Ian A. Hiskens

An imminent release of plug-in electric vehicles *en masse* will add substantial load to electrical power grids that are already operating near limits. Coordinated control of vehicle charging, however, can eliminate the need for expensive overhauls of grid infrastructure. Furthermore, the growing penetration of renewable energy sources provides an excellent opportunity to meet the increased electricity demand, but the challenge remains to tackle the variability and intermittency associated with renewable energy. Our research focuses on identifying and analyzing key issues regarding interactions between renewable generation, vehicle charging, and the power grid. In order to address these issues, we are designing control schemes that ensure seamless integration of newer forms of generation and load, while achieving satisfactory grid-level performance in areas such as loss minimization, voltage regulation, generation balancing and valley filling.

Feedback control oriented analytical models have been developed to regulate aggregate demand by certain time deferrable loads (thermostatic loads, plug-in electric vehicle chargers). It is shown that, via a hysteresis-based pulse-width modulated type control, a linearized system response model can be established from the evolution of probability distribution of states (thermostat temperature, battery state-of-charge) of loads. It is shown that grid-level objectives, such as generation tracking and valley filling, can be satisfied by using only the aggregate power as measurement. A framework is presented to study the impact of synchronization in plug-in electric vehicle chargers on the voltage resiliency of electrical grid. It is shown that a fault-induced synchronized tripping of chargers can cause critical over-voltage situations in a distribution feeder. A non-linear state-space model is developed that can truly capture the complex, easily synchronizable, dynamics of hysteresis-based loads. It is reported that, under certain control input signals, such load aggregation can display instability in the form of period-adding cascade. A control method is proposed that optimally allocates photo-voltaic inverter output in a de-centralized way to minimize line losses and voltage deviations. While optimality of this de-centralized control law is proved under certain assumptions, its validity in a more practical scenario is also discussed and possible modifications are suggested.

# CHAPTER I

# Introduction

*"With its array of gadgets and machines, all powered by energies that are destructive of land or air or water, and connected to work, market, school, recreation, etc., by gasoline engines, the modern home is a veritable factory of waste and destruction. "-Wendell Berry*[1]

Harsh words, no doubt! But there is definite truth in this. Residential sector consumes about 36% of global energy [3] and there is every indication that the residential energy consumption is only going to increase. Different surveys have forecasted that electricity demand growth in USA will be led by commercial and residential sectors [4, 5]. In USA, the total energy demand growth till 2035 has been estimated at 30% per annum, led by commercial (42%) and residential (24%) sectors [4]. Add to this the new type of load of plug-in electric vehicles (PEVs) are going to put on electrical grid, once they hit the market in large scale, and the future of power system . Today's electrical grid, with its largely ageing infrastructure, is going to be under extreme stress possibly leading to failure unless intelligent measures are taken to better manage an increasing demand. This rising demand is now coupled with alarmingly fast depleting fossil fuel (natural gas, coal, petroleum, etc.) reserves. Efforts are in place to increase energy production from renewable sources (hydro, biomass, wind, geothermal, solar, etc.). While renewables today constitute only 10% (hydro 6%, non-hydro 4%) of total electricity generation in USA, non-hydro renewables are expected to grow fast with wind- and bio-energy leading the way with 3% per annum rate till 2035 [6], [1]. Fig. 1.1 shows estimated growths of non-hydro renewable energy sources in USA. While this is indeed an encouraging scenario, the growth of renewables worldwide is faced with a variety of challenges, such as financial (high capital cost), policy-related (lack of long-term support towards new investments), and technological [7].

Within the scope of this thesis work, possible solutions will be proposed to overcome some of these technological challenges. Renewable generations are characteristically *intermittent* [8] and *non-dispatchable* [9], and cannot, in general, be relied upon for smooth and regulated supply at all times. For safe and reliable operation of the power grid, the generation has to meet the demand at all times. The current practice is largely to schedule conventional generation units (coal, hydro, natural gas) based on electrical load forecasts,

---

[1] Wendell Berry is an American writer, farmer and academic.

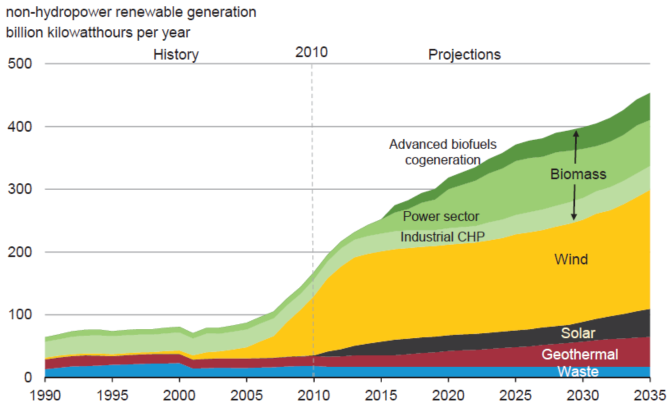

Figure 1.1: Projection of non-hydro renewable power generation in USA [1].

over both short term (tens of minutes) as well as long terms (days) [10]. Any adjustments in generation due to forecasting error are done real-time, e.g. via storage units (over-generation) or spinning and non-spinning reserves (under-generation). At low penetration levels, the daily variations in renewable generations can be dealt with similar to the load variations, by using available weather forecasts to dispatch existing conventional generation plants [7]. But clearly as more number of renewable sources penetrate the grid, the technique of forecast based generation scheduling would become increasingly difficult and unsustainable. The fluctuations of renewable generation are usually much faster than the ramp rates of conventional generators. A study by California Independent System Operator (CAISO) estimates maximum ramping requirement due to wind variability at 190 MW/min while 84% of its generation capability has a ramp rate less than 10 MW/min [11]. At large penetration levels, the fluctuations in renewable generation would become nearly impossible to be mitigated through scheduling of conventional generators. The variability and uncertainty associated with forecast would necessitate building of large amount of storage and spinning reserves. To be able to act as reserves, any additional back-up generation unit is forced to operate at a low fraction of its full capacity most of the times. Apart from the capital cost, continuous running of these reserves will mean less-than-efficient energy generation as well as higher carbon emission [12].

This calls for a definite paradigm shift to deal with increased penetration of renewable energy into the electrical grid. Primary objective of this thesis work is to address this changing grid scenario and explore ways to help in smooth integration of renewable energy into existing power system, at the same time accommodating an increasing electricity demand through load-control measures, without calling for an infrastructural overhaul. Quoting from [7],

*"Small-scale wind and solar photovoltaic systems create the potential for adding thousands of generating sources to the nation's distribution system. This would change fundamental engineering calculations about maintaining the delicate balance between supply and demand that must be constantly maintained in order to ensure the reliability and in-*

*tegrity of the electric system. This requires special steps to manage the power swings and new peaks, and requires additional balancing units.”*

## 1.1 Demand-side Control

Control of electrical loads actually presents a better alternative than building additional generation reserves to mitigate variability in renewable energy [12–14]. Load control is a faster and more efficient way of dealing with fluctuations in renewable generation, in addition to relieving the grid of financial burden of setting up new reserve capacity. Renewable generation units (e.g. photovoltaic cells) are spatially distributed across the grid thereby further encouraging electrical loads participation in balancing supply and demand. Probably the most important characteristic sought in electrical loads in consideration for generation-balancing support is *time-flexibility* [12]. Domestic appliances that satisfy this requirement are air-conditioners, space and water heaters, etc., exact operations of which can be altered without causing any perceptible change (or degradation) in their end-use performance. In a 2005 survey [15] in USA, air-conditioning loads contributed to 8%, while space and water heating contributed to 61% of total residential energy use. Heating and cooling type loads are only going to increase over the next few decades as shown in Fig. 1.2.

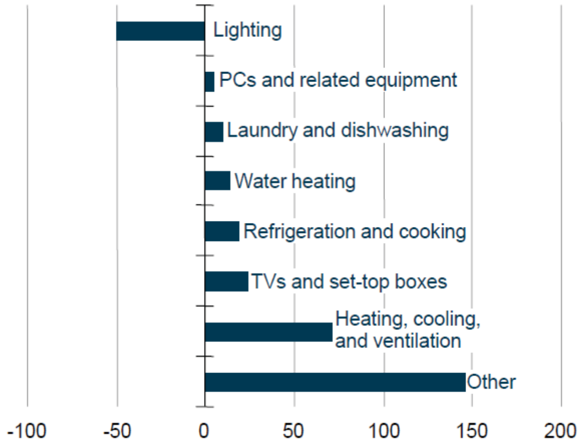

Figure 1.2: Projection of change (billion killowatthours) in residential electricity use in the period 2009-2035 [2].

In the scope of this thesis work, the electrical loads considered for demand-side control will be broadly referred to as *thermostatically-controlled-loads* (TCLs). Operation of such loads are governed by a thermostat which maintains its temperature within a hysteresis deadband about a set-point temperature. Air-conditioners are example of cooling type TCL, whose temperature decreases when they draw power. Because these TCL loads are on/off loads and not subject to the ramping limits of conventional thermal generation, they can be fully deployed on the time scale of the latency of the communication system used to access them, e.g. $\sim$0.3 minutes [14, 16–19]. However one primary challenge in designing demand side control techniques is that because an accurate model needs to know the states of operation of the electrical loads, it can run into the danger of being termed as invasive of customer privacy. Already there have been concerns raised on the intrusive nature of a two-way communication between the load co-ordinator and the electricity customer [20–23].

Research into the behavior of TCLs began with the work of [24] and [25], who proposed models to capture the hybrid dynamics of each thermostat in the population. The aggregate dynamic response of such loads was investigated by [26], who derived a coupled ordinary and partial differential equation (Fokker-Planck equation) model. The model was derived by first assuming a homogeneous group of thermostats (all thermostats having the same parameters), and then extended using perturbation analysis to obtain the model for a non-homogeneous group of thermostats. In [27], a discrete-time model of the dynamics of the temperatures of individual thermostats was derived, assuming no external random influence. That work was later extended by [28] to introduce random influences and heterogeneity. Although the traditional focus has been on direct load control methods that directly interrupt power to all loads, recent work in [29] proposed hysteresis-based control by manipulating the thermostat setpoint of all loads in the population with a common signal. While it is difficult to keep track of the temperature and power demands of individual loads in the population, the probability of each load being in a given state (ON - drawing power or OFF - not drawing any power) can be estimated rather accurately. System identification techniques were used in [29] to obtain an aggregate linear TCL model, which was then employed in a minimum variance control law to demonstrate the load following capability of a population of TCLs. In a related work [30], the authors showed that by allowing some “smartness” into battery chargers (equally applicable to other ON/OFF type of loads) a stochastic control strategy can be used to perform frequency regulations in a robust and decentralized manner.

However still there are open challenges in the context of load control. Designing a good demand control requires an accurate model of the demand response. While an accurate response model can be derived using coupled ordinary and partial differentiated equations [26], it is not useful from a control designer’s perspective. In more recent times, a lot of important studies have been done on building a control-oriented model of hysteresis-based loads [29, 31–34]. But due to system complexity, either a system identification based approach has been undertaken, or simplifying assumptions are made that lead to an approximate analytical model which is then coupled with feedback to eliminate modeling errors. However, as studies show, such load control techniques are often associated with highly nonlinear dynamics, often a result of some synchronization of loads operation.

## 1.2 Plug-in Electric Vehicles Charging Load

Many market research reports suggest that by 2020, vehicles that acquire energy from the grid, which will be henceforth referred to as as plug-in electric vehicles (PEVs), may well account for around 20% of total automobile sales in the USA [35–37], at which stage PEVs will account for 3-6% of the total electricity demand. It is likely that financial incentives will encourage charging overnight, when background non-PEV demand is less than the average [38], e.g. the overnight "valley" hours. Therefore, it may be concluded that during overnight hours, PEV charging load will contribute a significant proportion of the total demand on residential distribution feeders. At this stage a synchronized or un-regulated charging of PEVs could potentially cause issues that affect *resiliency* of the power grid. Although the interpretation of the term "resiliency" could vary, in this context it could mean power grid's adaptability under unforeseen change in grid structure. More specifically, when PEV charging load is a significant portion of the total load on the grid, synchronized behavior of PEV chargers can create instability in the grid, similar to fault-induced delayed voltage recovery (FIDVR) [39] of residential air-conditioner compressors leading to cascading voltage collapse. Although un-regulated charging of a large fleet of PEVs can pose concerns for the ageing and near-saturated grid infrastructure [40, 41], regulating the charging process may actually be beneficial to the grid.

Research is being carried out on different techniques of controlling a group of PEV chargers, at both distribution and transmission level. At the distribution level, optimal control algorithms have been studied to address the concerns that uncoordinated charging can lead to power losses and voltage deviations, worsen the grid load factor [42–45], or even cause black-outs [46]. In [42] authors showed that by establishing a relation between the distribution feeder losses, load factor and load variance, it is possible to formulate a convex optimization problem to co-ordinate PEV charging in order to minimize system losses and voltage deviations. A real-time smart load management control for PEV charging was developed in [46] that takes into consideration time-varying market energy prices, PEV owner preferred charging time zone, as well as random plug-in of PEVs to minimize generation cost and power losses. Various optimization techniques, from linear programming [44], to quadratic and dynamic programming [43] have been used in obtaining an optimal charging mechanism which enables higher penetration of PEVs in the distribution feeder while satisfying the network operation criteria (losses, voltage profile, etc.). In [47], authors showed that roughly 50% reduction in number of replacements of overloaded components (transformers, cables) is possible with controlled PEV charging, thereby decreasing system operation cost. Decentralized incentive-based charging control algorithm was proposed in [48] to optimally shape the demand so as to avoid distribution transformer overheating. In a recent development, a grid-friendly charging control technology from Pacific Northwest National Laboratory, USA, that uses grid frequency to regulate vehicle charging process, is poised to be soon implemented [49].

At the transmission level, considering a large number of vehicles (say, tens of thousands), the primary objective and scope of the charging control change. Specifically, in this dissertation, the focus would be on the following two objectives-

A. fill the overnight demand "valley" thereby reducing daily "cycling" of power plants and hence operational cost [50], as well as improving life expectancy of distribution transformers [51], and

B. encourage higher utilization of wind power by performing faster generation-balancing [18, 52]. Especially since the wind velocity is generally high at night, a successful charging control algorithm can facilitate large integration of wind and PEVs into the grid.

Studies have considered different control architectures, such as a *centralized control scheme* where a central decision-making body supervises the operation of the loads making sure their end-use constraints are satisfied, or a *de-centralized control scheme* where each PEV charger will decide its charging scheme on it own ultimately trying to achieve some global optimal performance. Often, a hierarchical control architecture is a more realistic approach, whereby a nominal (or optimal) charging profile is determined by a system operator, and the participating PEV chargers then respond on their own to this centrally communicated charging profile. [53] proposed a two-level charging control algorithm that achieves valley filling, by optimal utilization of wind energy, and frequency regulation, via feedback control. In [54], the stochastic nature of the problem (such as, renewable generation, PEV battery charge levels, number of plugged-in PEVs, etc.) was taken into consideration in developing a semi-Markov decision process based optimal charging policy. A de-centralized price-based charging scheme was developed in [38], which was to shown to achieve a Nash equilibrium that corresponds to valley-filling. The charging strategy was proven to be optimal when the vehicle population is homogeneous or near-optimal when the population is heterogeneous. A de-centralized valley-filling charging strategy which is optimal for both homogeneous and heterogeneous loads was developed in [55].

Most of these studies, however, assume that the charging demand of the individual PEVs can be controlled in a continuous fashion, which may not be possible in practice. A more realistic approach seems to be that the PEV would be allowed to charge only at certain restricted power levels, where the actual charging demand is controlled via some pulse-width-modulated (PWM) signal. PWM based control signals can be used to regulate the charging current of the individual chargers, where the PWM signal is set by some external (central) controller [56, 57]. In [52], the authors used a similar approach coupled with a hysteresis-based charging strategy (inspired by thermostatic control in [29]) to achieve load following by PEVs. However an analytical model to predict the system dynamics is required to design an efficient control scheme that can perform demand shaping without risking any synchronization.

## 1.3 Distributed Photovoltaic Generators

Another interesting research direction is to devise ways of using reactive power capabilities of grid-connected distributed generation to improve performance of the electrical grid.

While on the transmission level there are different options of renewable energy generation (transmission-scale wind, concentrating solar power, large scale photovoltaic (PV)), at the distribution level the only viable option, currently, is residential PV generators. Many studies have been done over the past few years on the feasibility, advantages and challenges of distributed PV generators at the low/mid-voltage level. A relatively early study [58] looked at the possibility and opportunity of using reactive power capability of the power electronics interface associated with distributed generators to provide ancillary support such as spinning reserve, voltage regulation, etc. Impact of distributed PV generators on voltage profile have been studied in [59–63]. Voltage sensitivity of lines in response to dynamics of voltage-support-distributed-generators were analyzed in [60] to establish optimal design criteria of voltage-support-distributed-generators. In [61], pseudorandom time series of solar irradiance have been considered to measure the impact of fluctuating solar irradiance on the grid voltage. A high-level of PV penetration at middle voltage level grid under different loading scenarios and different orientations of solar panel were analyzed in [62] to study the impact on network power loss, voltage balance and peak load compensation. It was observed that in all network conditions a PV penetration equalling up to the load can be easily accommodated. In [63] authors demonstrated through analysis and experiment that a compromise based control method can added to distributed generation inverters to achieve somewhat competing objectives of voltage regulation and harmonic suppression.

Although, the current interconnection standards [64] prevent the use of reactive power capability of PV inverters, a lot of interest has been generated recently in coming up with control algorithms to regulate the reactive power injection/consumption from inverters associated with distributed PV generators. To mitigate fast voltage fluctuations on the feeder, de-centralized control schemes look more viable option [65–70]. This often presents the challenge of a trade-off between higher speed in distributed control against guaranteed optimality of centralized scheme. Nevertheless distributed control has its own advantages in terms of higher resilience [67] and less communication bandwidth requirement. *Multi-agent system* based de-centralized dispatch schemes have been proposed to utilize distributed energy resources in achieving optimal grid performances, such as voltage regulation [65, 66]. In [68, 69] local control schemes based on locally measurable variables (reactive power consumption, local node voltage) were compared against a globally optimal centralized dispatch scheme. Another interesting approach is to apply networked control systems and achieve optimality via information exchange between close neighboring resources [67, 70]. However this area still remains largely open as the correlation between the locally observable variables and optimal reactive power dispatch is not yet fully understood and further research is required to formulate an optimal local control strategy. Often the actual power system network is sparse in terms of distributed generation resources, and communication between the resources could be unavailable. In such cases, a physically based correlation between the globally computed optimal variables and the local measurements can give better understanding of how a local optimal control law can be designed.

## 1.4 Overview of the Dissertation

The overarching goal of this thesis work lies in identifying many challenges associated with the fast changing electrical grid structure initiated by integration of renewable energy sources, ever-increasing electricity demand, and large scale penetration of plug-in electric vehicles, and investigating new control algorithms to smoothen the process of integration of these new elements. And an efficient control law requires an accurate system model. While many studies are being carried out in related topics, the primary focus of this dissertation is to take a physically based approach to understanding the complex interplay of varied dynamics. More specifically this dissertation will address the challenges in designing model-based feedback control scheme for large number of electrical loads, control-oriented charging scheme of plug-in electric vehicle chargers, impact of load synchronization on electrical grid, and distributed control of photo-voltaic inverters in a feeder.

In Chapter II an analytical approach is taken to model the evolution of probability distribution of a large aggregation of thermostatic loads. It is showed how this model can be linearized in order to use a feedback control law which enforces the demand to track supply fluctuations. Chapter III discusses how a hysteresis-based charging mechanism can enable a group of PEV chargers to perform similar ancillary services via feedback control. The impact of synchronization in PEV chargers, initiated by a fault-induced tripping, on the voltage resiliency of electrical grid is studied in Chapter IV. In Chapter V a state-space based modeling technique is presented which can truly capture the dynamics of a group of hysteresis-controlled chargers. With the help of this model, the behavior of the group of PEV chargers to a wide range of control input is observed. A distributed control method is proposed in Chapter VI that aims to optimally choose photo-voltaic inverter output in order to minimize line losses and voltage deviations. The challenges in designing such an optimal local control law in a practical scenario are discussed and possible modifications are suggested. Finally the dissertation is concluded in Chapter VII.

# CHAPTER II

# Setpoint Control of Thermostatically-controlled-loads

In this chapter the specific modeling and control approach undertaken in the thesis to regulate aggregate power demand of thermostatically-controlled-loads (TCLs), often referred to as simply 'thermostatic loads', will be discussed. Natural examples of such loads are air-conditioners, water heaters. These loads are quite abundant in any residential area, usually large in number but small in size (each drawing only a fraction of a kilo-Watt power over its duty cycle). It can be shown, that when these loads are considered in aggregation, even through small control efforts a significant change in total power demand can be initiated. In other words, such aggregate thermostatic loads have the capacity of significant anciallary services (peak load shaving, generation following) without effecting any perceptible change to the end-user experience.

Specifically in this work, a centralized type of control mechanism is considered where the temperature setpoints of all the participating TCLs are changed uniformly by the same control signal sent from a central co-ordinator. The job of this central co-ordinator is to measure the aggregate power demand by the aggregation of TCLs and dispatch the control signal in order to regulate the aggregate demand. To be able to compute the control law the central co-ordinator needs to use an accurate enough model for the response of aggregate demand to control input, coupled with a feedback control law. One of the big advantages of using electrical loads for ancillary services is their responsiveness to control signals. Advances in communication system ensures that communication delay between co-ordinator and the loads can be really small, only a fraction of a minute [14, 16–19], and thus it would be assumed in this work and control signals are sent to the participating TCLs at the interval of 1-min.

A transfer function is developed, which relates the changes in aggregate response of a homogeneous group of TCLs to disturbances that are applied uniformly to the thermostat setpoints of all TCLs. Starting from hybrid temperature dynamics of individual thermostats in the population, the steady-state probability distribution of loads being in the ON or OFF states are derived. When the temperature set-point is decreased uniformly across the population of TCLs more power will be drawn for cooling, i.e. the probability of a TCL being in the ON stat increases, and vice versa. Utilizing this observation, an input-

Table 2.1: Key symbols for Chapter II

| | |
|---|---|
| $N$ | number of TCLs |
| $\theta(t)$ | temperature ($^oC$) of a TCL at time $t$ |
| $\theta_{amb}$ | ambient temperature ($^oC$) |
| $\Delta$ | width of the temperature deadband ($^oC$) |
| $\theta_+$ | upper deadband limit ($^oC$) |
| $\theta_-$ | lower deadband limit ($^oC$) |
| $\theta_s(t)$ | temperature setpoint ($^oC$) at time $t$ |
| $C$ | thermal capacitance ($kWh/^oC$) |
| $R$ | thermal resistance ($^oC/kW$) |
| $P$ | power drawn ($kW$) by a TCL in its ON-state |
| $T_c$ | duration a TCL spends in cooling (ON) cycle in its steady state |
| $T_h$ | duration a TCL spends in heating (OFF) cycle in its steady state |
| $t_c(\theta)$ | duration an ON TCL takes from $\theta_+$ to $\theta$ |
| $t_h(\theta)$ | duration an OFF TCL takes from $\theta_-$ to $\theta$ |
| $N_c$ | number of ON TCLs in steady state |
| $N_h$ | number of OFF TCLs in steady state |
| $n_c(\theta)$ | steady-state number of ON TCLs having temperature in $[\theta, \theta_+]$ |
| $n_h(\theta)$ | steady-state number of ON TCLs having temperature in $[\theta_-, \theta]$ |
| $f_1(\theta)$ | steady-state probability density function of ON-state TCLs, $\theta \in [\theta_-, \theta_+]$ |
| $f_0(\theta)$ | steady-state probability density function of OFF-state TCLs, $\theta \in [\theta_-, \theta_+]$ |

output relationship between change in temperature set-point and change in aggregate power demand are developed based on steady-state probability distributions.

## 2.1 Thermal Dynamics of a TCL

The dynamic behavior of the temperature $\theta(t)$ of a thermostatically controlled cooling-load (TCL), in the ON and OFF state and in the absence of noise, can be modeled by [27],

$$\dot{\theta} = \begin{cases} -\frac{1}{CR}\left(\theta - \theta_{amb} + PR\right), & \text{ON state} \\ \\ -\frac{1}{CR}\left(\theta - \theta_{amb}\right), & \text{OFF state} \end{cases} \tag{2.1}$$

where the model parameters are listed in Table 2.1. The dynamics forces a TCL's temperature into a hysteresis deadband from $\theta_-$ to $\theta_+$ around the setpoint temperature $\theta_s = (\theta_- + \theta_+)/2$. A TCL switches its state from OFF to ON when its temperature increases to $\theta_+$ and from OFF to ON when temperature drops to $\theta_-$. Solution of Eqs. (2.1) with such boundary conditions is shown in Fig. 2.1 (top). Fig. 2.1 (bottom) shows that, at steady state, power consumption by a TCL switches between a constant and zero values, respectively in ON and OFF states. For a large *heterogeneous* ($C, R$ and $P$ values are different across the population) ensemble of TCLs, the aggregate power demand attains a steady state value [29]. In steady state, temperatures of all the TCLs would lie within the hysteresis deadband.

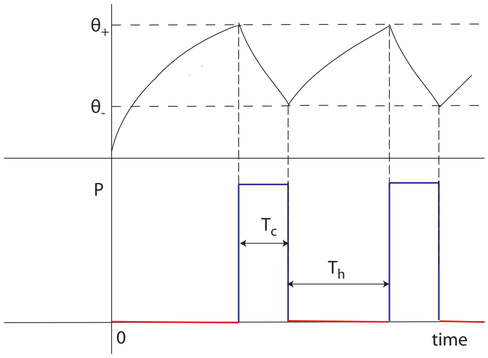

Figure 2.1: Dynamics of temperature of a thermostatic load.

## 2.2 Steady State Distribution of Loads

Solving (2.1), the durations a TCL spends in the cooling and heating cycles, $T_c$ and $T_h$ respectively, in the steady state can be found out as

$$T_c = CR \ln\left(\frac{PR + \theta_+ - \theta_{amb}}{PR + \theta_- - \theta_{amb}}\right) \tag{2.2a}$$

$$T_h = CR \ln\left(\frac{\theta_{amb} - \theta_-}{\theta_{amb} - \theta_+}\right) \tag{2.2b}$$

and, in general, time taken to reach some intermediate temperature $\theta_f \in [\theta_-, \theta_+]$ during the cooling and heating periods, $t_c(\theta_f)$ and $t_h(\theta_f)$ respectively, are,

$$t_c(\theta_f) = CR \ln\left(\frac{PR + \theta_+ - \theta_{amb}}{PR + \theta_f - \theta_{amb}}\right) \tag{2.3a}$$

$$t_h(\theta_f) = CR \ln\left(\frac{\theta_{amb} - \theta_-}{\theta_{amb} - \theta_f}\right). \tag{2.3b}$$

For a homogeneous[1] number of TCLs expected to be found in steady state within any temperature region inside the deadband is proportional to the time a TCL takes to sweep that temperature region. Accordingly, using the notations in Table 2.1, following relations hold

$$\frac{n_h(\theta)}{t_h(\theta)} = \frac{n_c(\theta)}{t_c(\theta)} = \frac{N_c}{T_c} = \frac{N_h}{T_h} = \frac{N}{T_c + T_h} \tag{2.4}$$

---

[1] All loads share the same values for parameters $\theta_{amb}$, $C$, $R$ and $P$.

where $N = N_c + N_h$. Defining, cumulative probability distributions of ON- and OFF-state loads, as

$$
\begin{aligned}
F_1(\theta) &:= Pr\{\text{“}a\ TCL\ is\ ON\text{”}\ and\ \text{“}its\ temperature\ is\ in\ [\theta_-, \theta]\text{”}\} \\
&= \frac{(N_c - n_c(\theta))}{N} \qquad (2.5a) \\
F_0(\theta) &:= Pr\{\text{“}a\ TCL\ is\ OFF\text{”}\ and\ \text{“}its\ temperature\ is\ in\ [\theta_-, \theta]\text{”}\} \\
&= \frac{(n_h(\theta))}{N} \qquad (2.5b)
\end{aligned}
$$

The ON- and OFF-state probability density functions, $f_1(\theta)$ and $f_0(\theta)$, can be now computed, using (2.1)

$$
\begin{aligned}
f_0(\theta) &= \frac{dF_0(\theta)}{d\theta} = \frac{CR}{(T_c + T_h)(\theta_{amb} - \theta)} \qquad (2.6a) \\
f_1(\theta) &= \frac{dF_1(\theta)}{d\theta} = \frac{CR}{(T_c + T_h)(PR + \theta - \theta_{amb})} \qquad (2.6b)
\end{aligned}
$$

These estimates are shown to match closely with the Monte-Carlo simulation Figure 2.2.

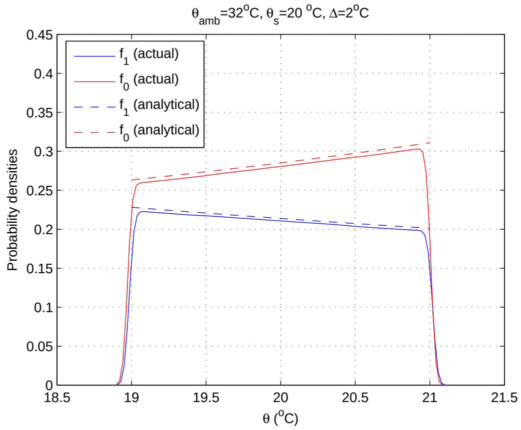

Figure 2.2: Steady state densities.

## 2.3 Setpoint Variation

Figure 2.3 shows the change in the aggregate power consumption of a population of TCLs for a small step change in the setpoint of all devices, while keeping deadband width unchanged. The goal is to derive the input-output relation between change in setpoint temperature and the resulting change in population's power demand. This will be done by studying the changes in the steady state probability distributions (Figure 2.4) initiated by the shift in temperature deadband. Let's assume that the deadband is shifted by an amount

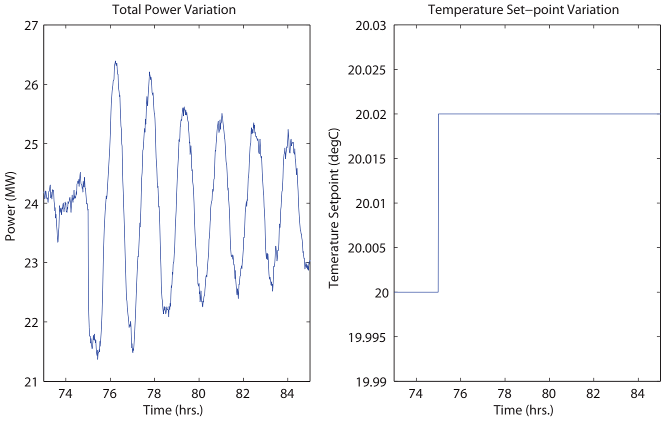

Figure 2.3: Change in aggregate power consumption due to a step change in temperature setpoint.

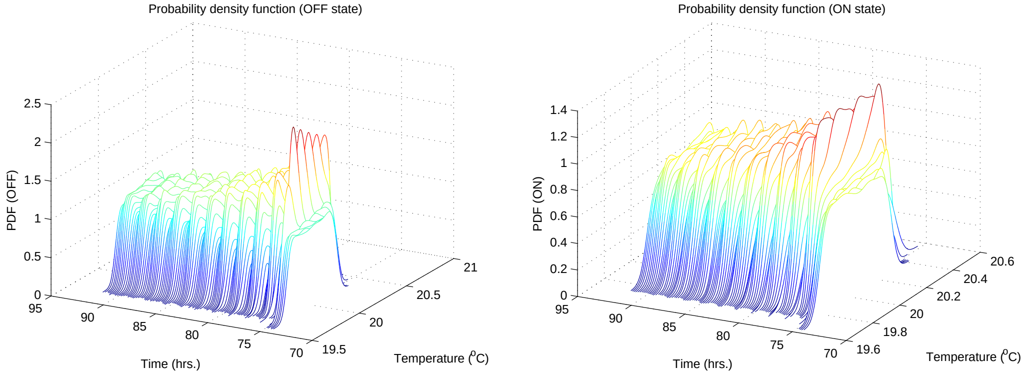

(a) OFF-state distribution.

(b) ON-state distribution.

Figure 2.4: Variation in distribution of loads due to setpoint disturbance.

$\delta$ from $[\theta_-^0, \theta_+^0]$ to $[\theta_-, \theta_+]$, with the deadband width $\Delta$ remaining unchanged. To compute the change in steady state power consumption, we would focus on four different TCL starting conditions, $a$-$d$ in Figure 2.5, immediately after the step change in setpoint. Let's denote the temperatures of loads at points $a$, $b$, $c$ and $d$ by $\theta_a$, $\theta_b$, $\theta_c$ and $\theta_d$, respectively, at the time of initiation of setpoint disturbance. The power consumption $g_a(t, \tau_a)$ of the load at $a$ in response to setpoint change is shown in Figure 2.6(a). All the loads in the OFF-state and having a temperature between $\theta_-$ and $\theta_+^0$ at the instant when the deadband shift occurs will have power waveforms similar in nature to $g_a(t, \tau_a)$. Thus the load at $a$ typifies the behavior of all the loads lying on the OFF-state density curve between $\theta_-$ and $\theta_+^0$. The same argument applies for loads at points $b$, $c$ and $d$. Figures 2.6(a)-2.6(d) illustrate the general nature of the power waveforms of the loads in all four regions, marked by $a$, $b$, $c$ and $d$ in Figure 2.5. Aggregate demand response is nothing but summation of demand response of TCLs lying in these four sections on the probability curves. Hence the aim is to separately compute the aggregate demand responses of all the TCLs in these four regions and then sum these up. Laplace transform of $g_a(t, \tau_a)$ is given by (Appendix A)

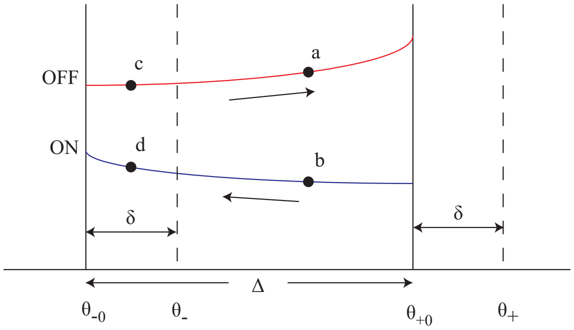

Figure 2.5: Different points of interest on the density curves.

$$\mathbf{G}_a(s, \tau_a) = e^{-s\tau_a}\mathbf{G}(s); \quad \tau_a = T_h - t_h(\theta_a)$$

where $\mathbf{G}(s) = \frac{P(1-e^{-sT_c})}{s(1-e^{-s(T_c+T_h)})}$. Averaging over all such loads (represented by $a$) on the OFF density curve between temperatures $\theta_-$ and $\theta_+^0$, we obtain the Laplace transform of the average power demand,

$$\mathbf{P}_a(s) = \int_{\theta_-}^{\theta_+^0} f_0(\theta_a)\mathbf{G}_a(s, \tau_a)d\theta_a \tag{2.7}$$

In a similar way, Laplace transforms of demand response of the TCLs at points $b$, $c$ and

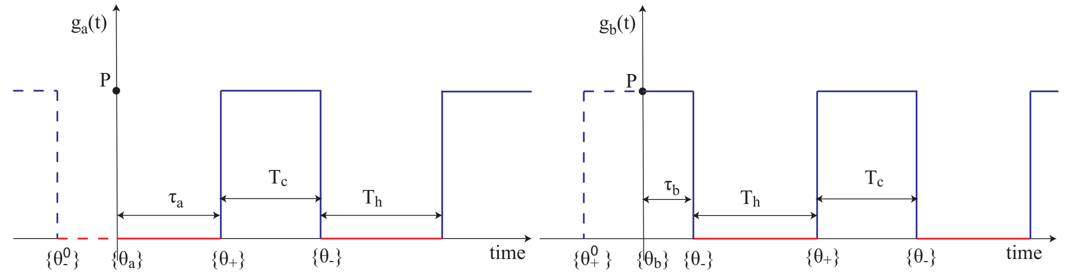

(a) Power waveform at point $a$.

(b) Power waveform at point $b$.

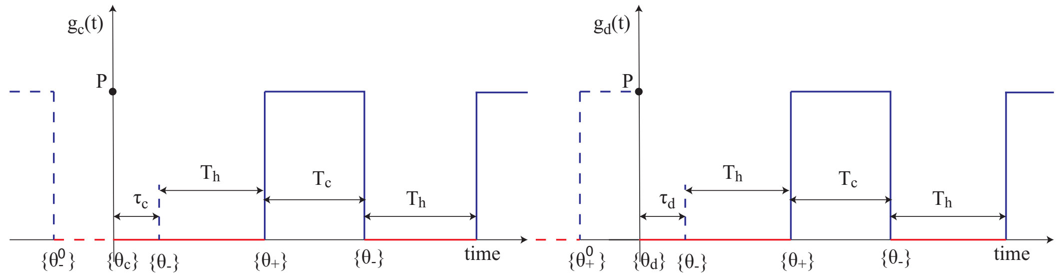

(c) Power waveform at point $c$.

(d) Power waveform at point $d$.

Figure 2.6: Power waveforms at four different points marked in Figure 2.5.

$d$ can be computed as (Appendix A),

$$\mathbf{G}_b(s,\tau_b) = \left(e^{s(T_c-\tau_b)}\mathbf{G}(s) - \frac{P}{s}\left(e^{s(T_c-\tau_b)}-1\right)\right), \quad \tau_b = T_c - t_c(\theta_b) \tag{2.8a}$$

$$\mathbf{G}_c(s,\tau_c) = e^{-s(T_h+\tau_c)}\mathbf{G}(s), \quad \tau_c = CR\ln\left(\frac{\theta_{amb}-\theta_-}{\theta_{amb}-\theta_c}\right) \tag{2.8b}$$

$$\mathbf{G}_d(s,\tau_d) = e^{-s(T_h+\tau_d)}\mathbf{G}(s), \quad \tau_d = CR\ln\left(\frac{\theta_{amb}-\theta_d}{\theta_{amb}-\theta_-}\right) \tag{2.8c}$$

and the average power demands of all the loads in the regions marked by $b,\ c$ and $d$ as,

$$\mathbf{P}_b(s) = \int_{\theta_-}^{\theta_+^0} f_1(\theta_b)\mathbf{G}_b(s,\tau_b)d\theta_b \tag{2.9a}$$

$$\mathbf{P}_c(s) = \int_{\theta_-^0}^{\theta_-} f_0(\theta_c)\mathbf{G}_c(s,\tau_c)d\theta_c \tag{2.9b}$$

$$\mathbf{P}_d(s) = \int_{\theta_-^0}^{\theta_-} f_1(\theta_d)\mathbf{G}_d(s,\tau_d)d\theta_d. \tag{2.9c}$$

The average power demand of the whole population becomes,

$$\mathbf{P}_{avg}(s) = \mathbf{P}_a(s) + \mathbf{P}_b(s) + \mathbf{P}_c(s) + \mathbf{P}_d(s). \tag{2.10}$$

Using (2.7), (2.9a), (2.9b) and (2.9c) we obtain an expression for $\mathbf{P}_{avg}(s)$ that is rather complex. It is hard, and perhaps even impossible, to obtain the inverse Laplace transform. However, with the assistance of MATHEMATICA®, $\mathbf{P}_{avg}(s)$ may be expanded as a series in $s$. It is assumed that,

A. *The deadband width is small, i.e.* $\Delta \ll (\theta_s - \theta_{amb} + PR)$ and $\Delta \ll (\theta_{amb} - \theta_s)$

B. *The shift in deadband is small relative to the deadband width, i.e.* $\delta \ll \Delta$

The steady-state power consumption is given by

$$P_{avg,ss} \approx \frac{(\theta_{amb} - \theta_+)N}{\eta R},$$

where $\eta$ is the electrical efficiency of the cooling equipment. The aggregate demand response, linearized around the steady state value $P_{avg,ss}$, becomes

$$\mathbf{P}_{tot}(s) \approx -\left(\frac{d}{s} + \frac{\omega A_\Delta}{s^2 + \omega^2}\right)\delta \tag{2.11}$$

where

$$\begin{aligned} A_\Delta &= \frac{5\sqrt{15}C(\theta_{amb} - \theta_+)(PR - \theta_{amb} + \theta_+)}{\eta\big(P^2R^2 + 3PR(\theta_{amb} - \theta_+) - 3(\theta_{amb} - \theta_+)^2\big)^{3/2}} \\ &\qquad \times \frac{(3PR - \theta_{amb} + \theta_+)N}{(T_{c0} + T_{h0})}, \\ \omega &= \frac{2\sqrt{15}(\theta_{amb} - \theta_+)(PR - \theta_{amb} + \theta_+)}{CR\Delta\sqrt{P^2R^2 + 3PR(\theta_{amb} - \theta_+) - 3(\theta_{amb} - \theta_+)^2}}, \\ d &= \frac{N}{\eta R}. \end{aligned}$$

and $T_{c0}$ and $T_{h0}$ are the pre-disturbance steady-state cooling and heating times, respectively. The transfer function for this linear model is,

$$\mathbf{T}(s) = \frac{\mathbf{P}_{tot}(s)}{\delta/s} = -\Big(d + \frac{A_\Delta \omega s}{s^2 + \omega^2}\Big).$$

Due to the assumptions of low-noise and homogeneity, our analytical model is undamped. The actual system, on the other hand, experiences both heterogeneity and noise, and therefore will exhibit a damped response. In order to capture that effect, we have chosen to add a damping term $\sigma$ (to be estimated on-line) into the model, giving

$$\mathbf{T}(s) = -\Big(d + \frac{s\omega A_\Delta}{(s + \sigma)^2 + \omega^2}\Big). \tag{2.12}$$

Figure 2.7 shows a comparison between the response calculated from the model (2.12) and the true response to a step change in the setpoint obtained from simulation. A damping coefficient of 0.002 $\text{min}^{-1}$ was added, as that value gave a close match to the decay in the actual system response.

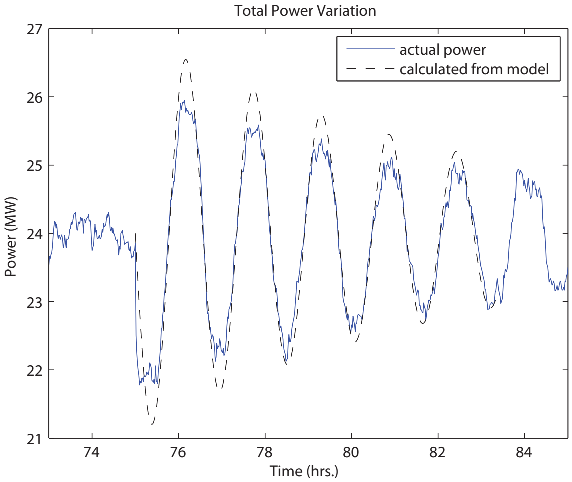

Figure 2.7: Comparison of the approximate model with the actual simulation, for the same setpoint disturbance as in Figure 2.3.

## 2.4 Control Law

The TCL load controller, described by the transfer function (2.12), can also be expressed in state-space form,

$$\begin{aligned} \dot{x} &= \mathbf{A}x + \mathbf{B}u \\ y &= \mathbf{C}x + \mathbf{D}u \end{aligned}$$

where the input $u(t)$ is the shift in the deadband of all TCLs, and the output $y(t)$ is the change in the total power demand from the steady-state value. The state-space matrices are given by

$$\mathbf{A} = \begin{bmatrix} -2\sigma & -\omega \\ \frac{\sigma^2+\omega^2}{\omega} & 0 \end{bmatrix}, \qquad \mathbf{B} = \begin{bmatrix} \omega A_\Delta \\ 0 \end{bmatrix},$$
$$\mathbf{C} = \begin{bmatrix} -1 & 0 \end{bmatrix}, \qquad \mathbf{D} = -d.$$

Our goal is to design a controller using the linear quadratic regulator (LQR) approach [71] to track an exogenous reference $y_d$. We observe that the system has an open-loop zero very close to the imaginary axis ($d \ll \omega A_\Delta$) and hence we need to use an integral controller. Considering the integral of the output error $e = (y - y_d)$, where $y_d$ is the reference, as the third state $w(t) = \int_0^t (y(\tau) - y_d(\tau))d\tau$ of the system, the modified state-space model becomes

$$\begin{aligned}\dot{\underline{x}} &= \underline{\mathbf{A}}\,\underline{x} + \underline{\mathbf{B}}u + \mathbf{E}\,y_d \\ y &= \underline{\mathbf{C}}\,\underline{x} + \underline{\mathbf{D}}u\end{aligned}$$

where $\underline{x} = [x \quad w]^\top$ and,

$$\underline{\mathbf{A}} = \begin{bmatrix}\mathbf{A} & \mathbf{0}_{2\times1} \\ \mathbf{C} & 0\end{bmatrix}, \qquad \underline{\mathbf{B}} = \begin{bmatrix}\mathbf{B} \\ \mathbf{D}\end{bmatrix}, \underline{\mathbf{C}} \qquad = \begin{bmatrix}\mathbf{C} & 0\end{bmatrix}, \underline{\mathbf{D}} \qquad = \mathbf{D}, \quad \mathbf{E} = \begin{bmatrix}\mathbf{0}_{2\times1} \\ -1\end{bmatrix}.$$

Minimizing the cost function

$$J = \int_0^\infty \big(\underline{x}(t)^\top Q \underline{x}(t) + u(t)^2 R\big) dt$$

where $Q \geq \mathbf{0}_{3\times3}$ and $R > 0$ are design variables, we obtain the optimal control law $u(t)$ of the form

$$u = -(\mathbf{K}\,\underline{x} + \mathbf{G}\,y_d),$$

with $\mathbf{G}$ a pre-compensator gain chosen to ensure unity DC gain. Since we can only measure the output $y(t)$ and the third state $w(t)$, the other two states are estimated using a linear quadratic estimator [71] which has the state-space form,

$$\begin{aligned}\dot{\hat{x}} &= \mathbf{A}\,\hat{x} + \mathbf{B}u + \mathbf{L}(y - y_d) \\ \hat{y} &= \mathbf{C}\,\hat{x} + \mathbf{D}u \\ u &= -\mathbf{K}\begin{bmatrix}\hat{x} \\ w\end{bmatrix} + \mathbf{G}\,y_d.\end{aligned}$$

The plots in Figure 2.8 show that the controller can be used to force the aggregate power demand of the TCL population to track a range of reference signals. Figure 2.9 shows that in presence of the feedback control action, the distribution of loads *almost* always remains close to steady state distribution, thereby holding the linearized model fairly valid under disturbances.

## 2.5 Summary

In this chapter an approach has been presented to analytically derive a transfer function relating the change in aggregate power demand of a population of TCLs to a change in thermostat setpoint applied to all TCLs in unison. A linear quadratic regulator designed on the aggregate response model forced the group of loads to track fluctuating trajectories, which could originate from renewable generation. The analysis has been based on the assumptions that the TCL population is homogeneous and that the noise level is insignificant.

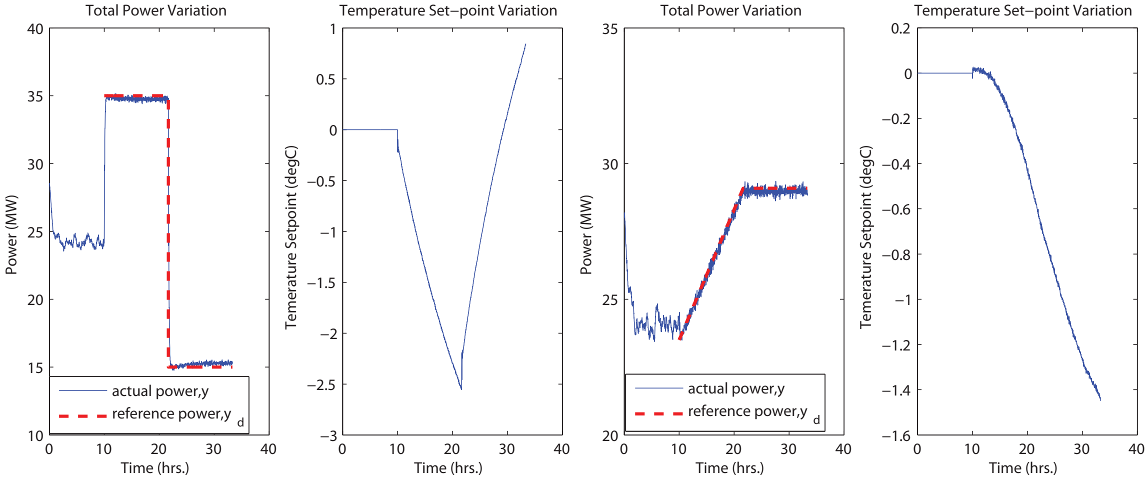

(a) Response to step reference and the control input. (b) Response to ramp reference and the control input.

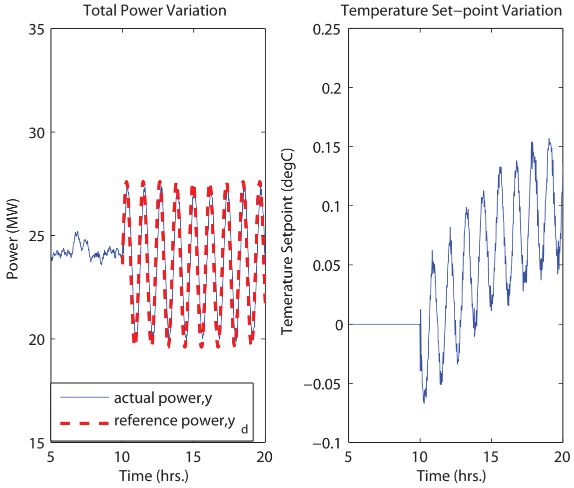

(c) Response to sinusoidal reference and the control input.

Figure 2.8: Reference tracking achieved through setpoint shift.

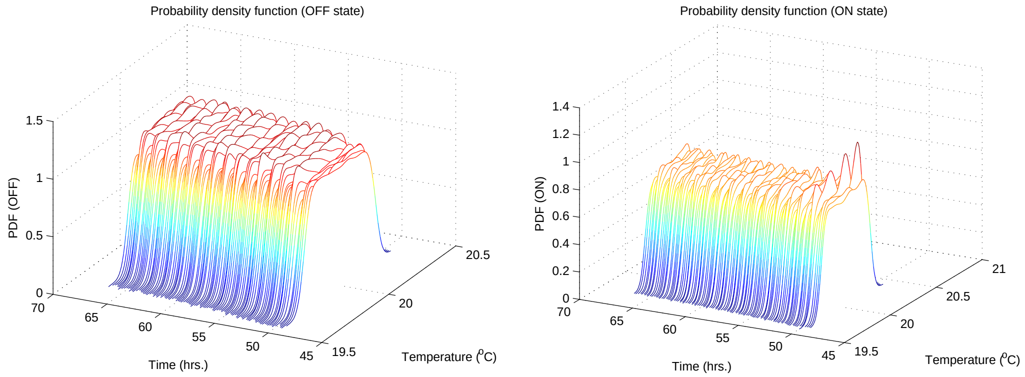

(a) OFF-state distribution. (b) ON-state distribution.

Figure 2.9: Variation in distribution of loads under the influence of the controller.

Further studies are required to incorporate the effects of heterogeneity and noise into the model. Those extensions are important for determining the damping coefficient. In extreme heterogeneity, possibly tracking performance would fail in absence of an accurate model. However, ongoing study [72] shows that different protocols could be generated such that the aggregate power demand is made to mitigate a sudden, and short, under-/over-generation of power without the need for detailed modeling and feedback control.

Performance of the hysteresis-based control designed in this chapter actually motivates further research on the feasibility of hysteresis-based control in plug-in electric vehicles charging load. Details of the development of hysteresis-based charging approach would be discussed in Chapter III.

# CHAPTER III

# Hysteresis-based Charging of Plug-in Electric Vehicles

In the scope of this thesis, all vehicles that derive their energy either partially or fully from the power grid would be termed as plug-in electric vehicles (PEVs). As PEVs start to penetrate the market in large numbers, PEV charging loads would become significant, at least on a localized level (e.g. in financially affluent neighborhoods). Due to price-based incentives, and convenience, most of these vehicles are going to be charged during off-peak hours, usually overnight. Often this PEV charging load is ‘deferrable’, since most customers only care about getting the vehicle fully charged by early morning. Thus potentially a large number of PEV chargers offer a significant energy resource to the utility that can be used to benefit grid operations (e.g. overnight ‘valley’ filling, generation balancing).

In Chapter II a modeling and control approach was discussed for a large group of thermostatic loads, in which the hysteresis band limits of the loads are moved by a central controller. Interestingly, similar control benefits can be also utilized in other hysteresis-based electric loads. While hysteresis-based control is a natural consequence of the inherent temperature dynamics in TCLs, such a mechanism can also be established for charging of a fleet of PEV chargers [52, 73]. Each vehicle charger is assigned a nominal state-of-charge (SoC) profile, which can be calculated from a ‘valley’ filling algorithm, or could a simple linear trajectory such that the vehicle gets fully charged by a stipulated time. A hysteresis-band is then introduced around the nominal SoC curve, such that the actual SoC follows the nominal SoC profile within the tolerance of the hysteresis deadband width, thereby giving rise to a charging process that resembles a pulse-width-modulated electrical power profile (a sequence of power ON and power OFF intervals).

Once a hysteresis based charging process is set up, a similar modeling approach as in Chapter II can be taken to develop a linearized response model for the PEV charging loads. A Lyapunov based feedback control law is designed to perform reference tracking by the aggregate of PEV chargers. Performance of the controller is tested against reference demand profiles representative of ‘valley’ filling, peak-shaving and fluctuating generation.

Table 3.1: Key symbols for Chapter III

| | |
|---|---|
| $N$ | number of PEVs |
| $SoC$ | state-of-charge ($kWh$) |
| $P_{max}$ | maximum charging rate ($kW$) |
| $P_{nom}$ | nominal charging rate ($kW$) |
| $E_{max}$ | battery charge capacity ($kWh$) |
| $\Delta$ | deadband width as a fraction of battery capacity |
| $t_0$ | the instant when charging starts |
| $t_f$ | the instant when charging completes |
| $N_{on}$ | number of "ON" PEVs in steady-state |
| $N_{off}$ | number of "OFF" PEVs in steady-state |
| $T_{on}$ | duration a PEV charger spends in ON cycle in steady-state |
| $T_{off}$ | duration a PEV charger spends in OFF cycle in steady-state |

## 3.1 Hysteresis-based Charging

The hysteresis-based charging of a PEV battery is developed assuming that the charging may take place only at two allowed rates [52]. The charger draws power at its maximum rate, $P_{max}$, when it is 'ON' and does not draw any power when it is 'OFF'. When PEV charger draws power (in ON state) its state-of-charge ($SoC$), also a measure of the energy consumed, increases linearly and during its OFF state the $SoC$ remains constant. The charging process stops when $SoC$ reaches the battery capacity, $E_{max}$. The sequence of ON and OFF states are decided by setting up a nominal charging trajectory and a small hysteresis band, a fraction $\Delta$ of the charge capacity, around the nominal trajectory such that during the whole charging process the $SoC$ always stays within the hysteresis band. The nominal trajectory is defined as the $SoC$ profile the charger would have if it were charged at a constant rate, $P_{nom}$, throughout the charging duration. After the charging process starts, at $t_0$, the charger turns OFF when its $SoC$ touches the upper deadband limit and remains OFF till its $SoC$ touches the lower deadband limit at which instant it switches back to ON state and this process continues till charging completes, at $t_f$. Fig. 3.1 shows a typical such charging profile.

To illustrate the situation, assuming a constant nominal charging rate, the nominal charge profile over the duration of charging, $[t_0, t_f]$, and the hysteresis deadband limits around it would be

$$SoC_{nom}(t) = (t - t_0)\,P_{nom}; \quad P_{nom} = \frac{E_{max}}{t_f - t_0} \tag{3.1a}$$

$$SoC_{+}(t) = (t - t_0)\,P_{nom} + E_{max}\Delta/2 \tag{3.1b}$$

$$SoC_{-}(t) = (t - t_0)\,P_{nom} - E_{max}\Delta/2 \tag{3.1c}$$

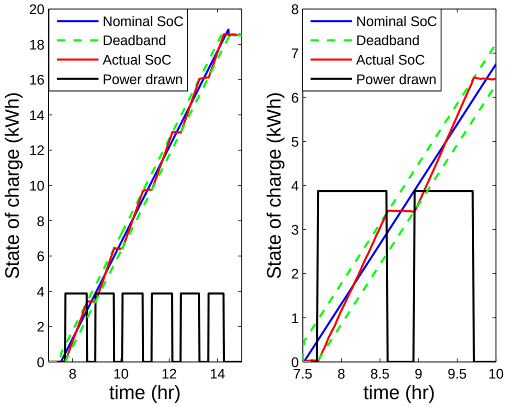

Figure 3.1: Hysteresis-based charging profile.

If $s(t)$ denotes the state of a charger and an assignment of $s(t) = 1$ when ON and $s(t) = 0$ when OFF is made, then the following dynamics governs the charging process

$$\dot{SoC}(t) = s(t)P_{max} \tag{3.2}$$

where

$$s(t) = \begin{cases} 1, & SoC(t) \leq SoC_{-}(t) \\ 0, & SoC(t) \geq SoC_{+}(t) \\ s(t-), & \text{otherwise.} \end{cases}$$

While the actual deadband width of a vehicle is proportional to its maximum charge capacity, the ratio of deadband width to charge capacity is the same for all. Defining a new variable

$$\widetilde{SoC}(t) = \frac{SoC(t) - SoC_{nom}(t)}{E_{max}} \tag{3.3}$$

which will be referred to as *normalized* $SoC$ henceforth, the dynamics in (3.2) can be modified as

$$\dot{\widetilde{SoC}}(t) = \frac{(s(t)P_{max} - P_{nom})}{E_{max}} \tag{3.4}$$

where

$$s(t) = \begin{cases} 1, & \widetilde{SoC}(t) \leq -\Delta/2 \\ 0, & \widetilde{SoC}(t) \geq \Delta/2 \\ s(t-), & \text{otherwise.} \end{cases}$$

This formulation helps in normalizing the hysteresis deadband. While the actual deadband shift with time being centered around $SoC_{nom}(t)$, the normalized deadband is static having a width $\Delta$, same for all, centered around zero.

If all the vehicles start charging at the same instant, $t_0$, the aggregate power demand would start with large oscillations which will ultimately settle down to a steady state aggregate demand level, as shown in Fig. 3.2(a)[1]. To analyze what happens during the cyclic ON and OFF states probability distribution of the normalized state-of-charge, $\widetilde{SoC}(t)$, is plotted in Fig. 3.2(b) and Fig. 3.2(c). Initially the ON probability density shows large peaks which move in the direction from lower deadband limit $-\Delta/2$ to upper deadband limit $+\Delta/2$ and appears as peaks in OFF probability density which move in the opposite direction. After a few cycles these peaks flatten out which corresponds to the steady state power demand in Fig. 3.2(a). However this oscillation can be avoided if the starting instant is allowed to be uniformly distributed over a time window of the order of the duration of a typical charging cycle (ON and OFF). Choosing $t_0$ to be uniformly distributed over a $50$ $min$ time window yields an aggregate power demand that shows minimal starting oscillation, as shown in Fig. 3.3(a). Fig. 3.3(b) and Fig. 3.3(c) show the corresponding evolution of probability density starting from the instant when all the PEVs have started charging.

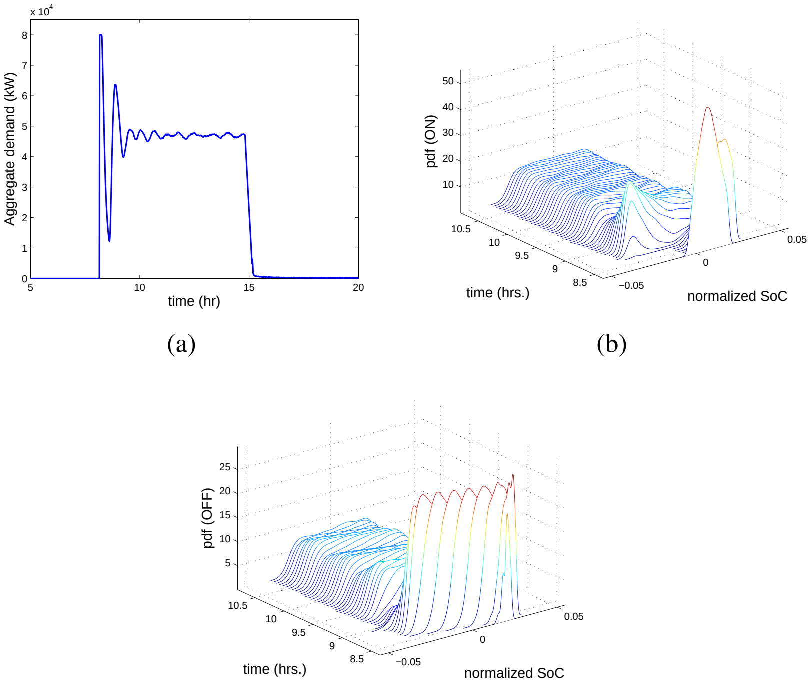

(a)

(b)

(c)

Figure 3.2: Aggregate response in hysteresis-based charging when the starting instant is same for all.

---

[1] Number of PEVs, $N$, is $20,000$. $E_{max}$ was chosen to be uniformly distributed over 12-20 $kWh$ and $P_{max}$ to be uniformly distributed over 3-5 $kW$. The deadband width is a fraction $\Delta = 0.05$ of $E_{max}$

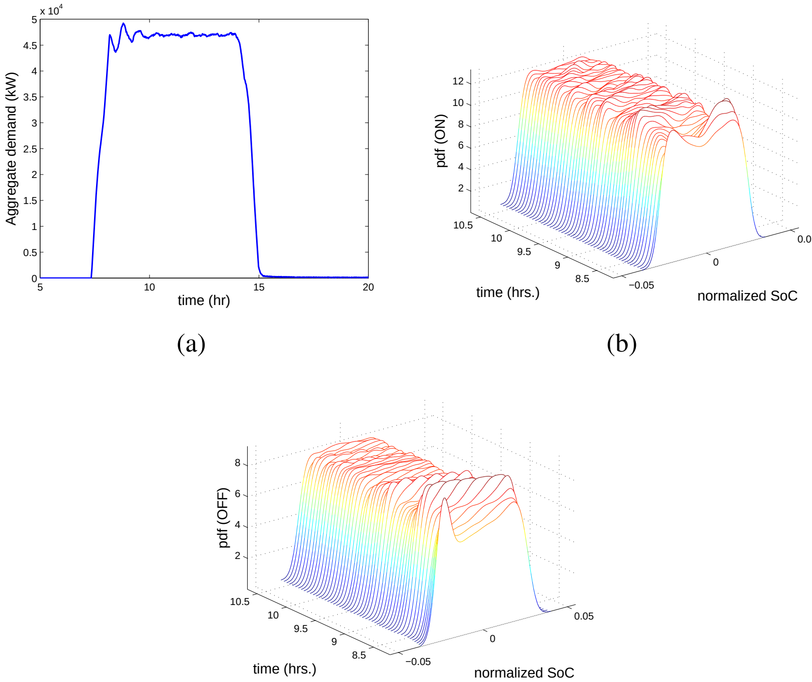

(a) (b)

(c)

Figure 3.3: Aggregate response in hysteresis-based charging when the starting instant is uniformly distributed.

## 3.2 Linearized State-space Model

The goal is to design a feedback control that regulates the aggregate power demand of PEVs by shifting the hysteresis deadband position while keeping the normalized width, $\Delta$, fixed. In this section, a linearized state-space model of the system is developed based on the steady state probability distribution of ON and OFF state chargers. The approach is similar to the one described in Chapter II. Section 3.2.1 derives an analytical estimation of the steady state probability distribution while Section 3.2.2 would build a system model linearized around the steady state distribution. Although the analysis presented here assumes that the system is *homogeneous* and *noise-free*, the Monte-Carlo simulation will consider a heterogenous system with some noise.

### 3.2.1 Steady State Probability Distribution

In the steady state the aggregate power consumption becomes (*almost*, for non-homogeneous noisy system) constant and hence the number of chargers in their ON state will be a constant number, $N_{on}$, and so will the number of chargers in OFF state, $N_{off} = N - N_{on}$. Since the rate of change of normalized state-of-charge, $\widetilde{SoC}(t)$, is constant (or independent of $\widetilde{SoC}(t)$) both in the ON and OFF state (from (3.4)), the probability distribution of ON and OFF-state chargers would have to be a uniform distribution between $[-\Delta/2, \Delta/2]$.

The values $N_{on}$ and $N_{off}$ can be found by equating the in-coming and out-going flux of probability at the boundaries of the normalized deadband $[-\Delta/2, \Delta/2]$. To maintain steady state distribution, the rate of departure of PEV chargers from ON state should be equal to the rate of departure of chargers from OFF state, i.e. from (3.4)

$$N_{on}\frac{P_{max}-P_{nom}}{E_{max}} = N_{off}\frac{P_{nom}}{E_{max}}.$$

Using $N_{on}+N_{off}=N$ gives,

$$N_{on} = \frac{NP_{nom}}{P_{max}}, \qquad N_{off} = \frac{N\left(P_{max}-P_{nom}\right)}{P_{max}}$$

and the probability density functions, $f_{on}$ and $f_{off}$ would be

$$f_{on} = \frac{P_{nom}}{P_{max}\Delta} \tag{3.5}$$

$$f_{off} = \frac{P_{max}-P_{nom}}{P_{max}\Delta} \tag{3.6}$$

Fig. 3.4 shows how the probability densities computed from (3.6) compare with the simulated steady state densities. The discrepancies could be attributed to the non-homogeneity and noise present in the simulated system.

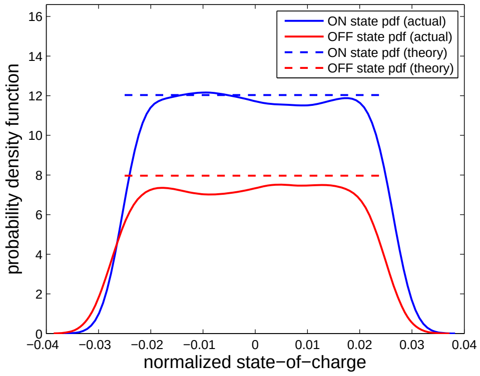

Figure 3.4: Probability distribution of $\widetilde{SoC}$ of vehicles in ON and OFF state.

### 3.2.2 Linearized Step Response

In this section we will build a linearized model of the system by analyzing the response of aggregate power demand to a step change in the nominal $SoC$ profile. Fig. 3.5(a) shows a typical response of the system of PEVs to a shift in the hysteresis deadband. To quantify this response in terms of the magnitude of shift, $\delta$, we will take a probabilistic approach, similar to the one in Chapter II. If we could sum up the responses of all the PEV chargers

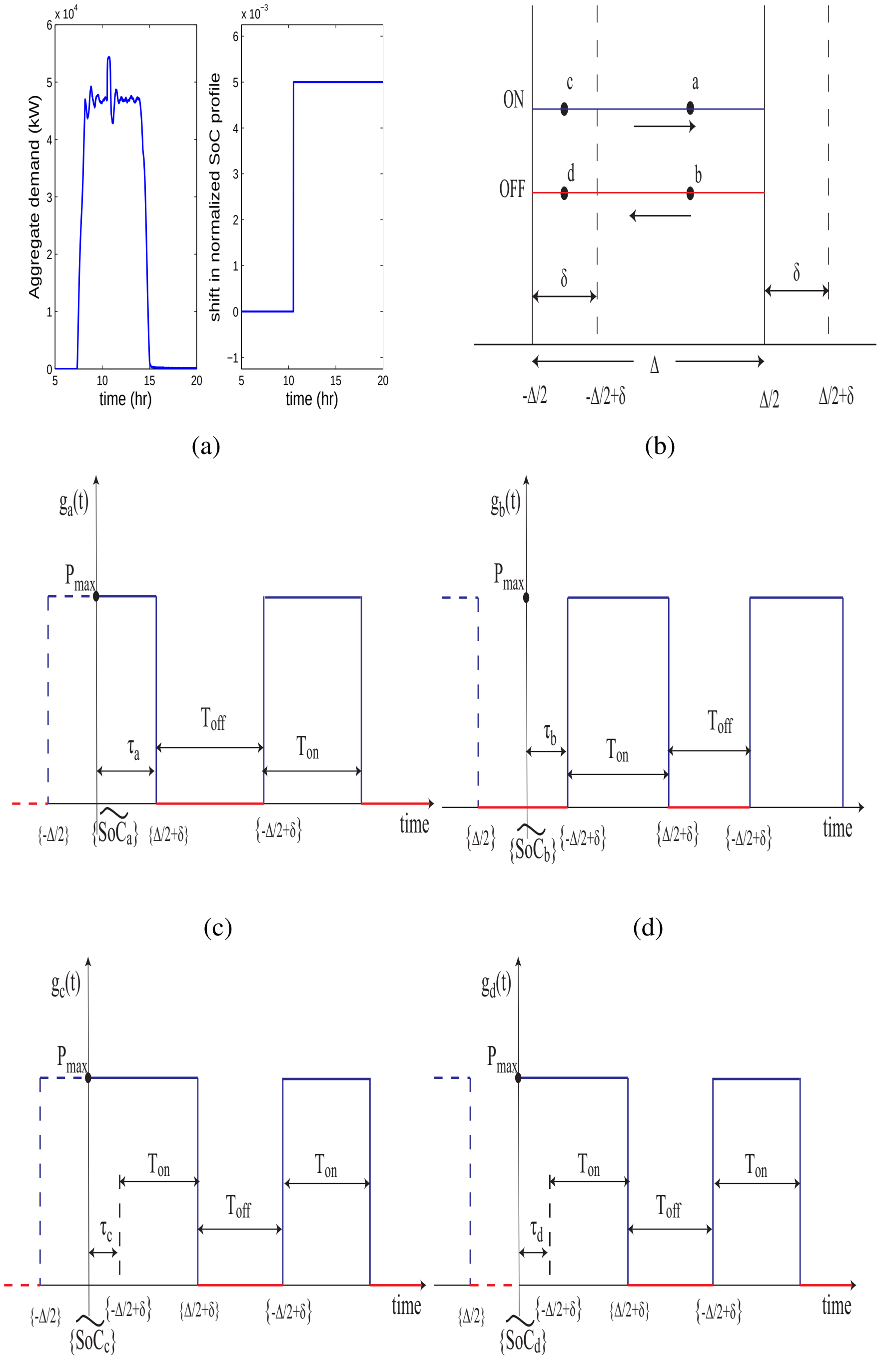

(a) (b)

(c) (d)

(e) (f)

Figure 3.5: Aggregate and individualistic response to a shift in deadband

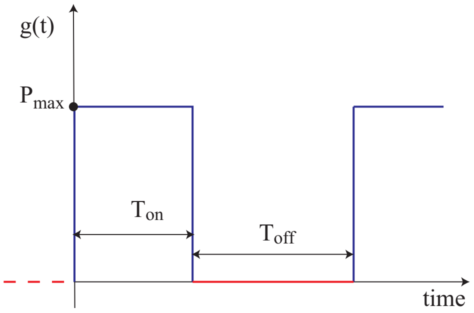

Figure 3.6: The reference square-wave $g(t)$.

in the population, we will quantify the aggregate response. In order to do that, we would split the probability density curves in four regions, as shown in Fig. 3.5(b):

A. *ON probability density curve between* $(-\Delta/2+\delta)$ *and* $\Delta/2$ (point '$a$')

B. *OFF probability density curve between* $(-\Delta/2+\delta)$ *and* $\Delta/2$ (point '$b$')

C. *ON probability density curve between* $-\Delta/2$ *and* $(-\Delta/2+\delta)$ (point '$c$')

D. *OFF probability density curve between* $-\Delta/2$ *and* $(-\Delta/2+\delta)$ (point '$d$')

Demand response of the PEV chargers lying in regions '$a-d$' to the shift in deadband would be similar to Figs. 3.5(c)-3.5(f). For example, a charger initially at '$a$', with a normalized state-of-charge $\widetilde{SoC}_a \in [-\Delta/2+\delta, \Delta/2]$, would stay ON for some time, $\tau_a$, and then continue with its natural OFF/ON sequence. Let us denote $T_{on}$ and $T_{off}$ as the time spent in ON and OFF states, respectively, in each cycle. The power response $g_a(t)$ in Fig. 3.5(c) is a time-shifted version of the square waveform $g(t)$ ($g(t)=0$ when $t<0$) in Fig. 3.6. Denoting Laplace transform of the waveform $g(t)$ as

$$\mathbf{G}(s) = \frac{P_{max}\left(1-e^{-sT_{on}}\right)}{s\left(1-e^{-s(T_{on}+T_{off})}\right)} \tag{3.7}$$

where, $T_{on}$ and $T_{off}$ are given by

$$T_{on} = \frac{E_{max}\Delta}{(P_{max}-P_{nom})}, \qquad T_{off} = \frac{E_{max}\Delta}{P_{nom}}, \tag{3.8}$$

we obtain the Laplace transform $\mathbf{G}_a(s)$ of $g_a(t) = g(t+T_{on}-\tau_a)\mathbf{1}(t)$, $\quad$ ($\mathbf{1}(t)$ : unit step) as

$$\mathbf{G}_a(s,\tau_a) = e^{s(T_{on}-\tau_a)}\mathbf{G}(s) - \frac{\left(e^{s(T_{on}-\tau_a)}-1\right)}{s}P_{max}$$

where

$$\tau_a = \frac{\Delta/2 + \delta - \widetilde{SoC}_a}{P_{max} - P_{nom}}$$

is the time taken to increase normalized state-of-charge from $\widetilde{SoC}_a$ to $(\Delta/2 + \delta)$. Similarly for other regions,

$$\mathbf{G}_b\left(s, \tau_b\right) = e^{-s\tau_b}\mathbf{G}(s); \quad \tau_b = \frac{\widetilde{SoC}_b + \Delta/2 - \delta}{P_{nom}} \tag{3.9a}$$

$$\mathbf{G}_c\left(s, \tau_c\right) = e^{-s\tau_c}\mathbf{G}(s) + \frac{(1 - e^{-s\tau_c})}{s}P_{max}; \quad \tau_c = \frac{-\Delta/2 + \delta - \widetilde{SoC}_c}{P_{max} - P_{nom}} \tag{3.9b}$$

$$\mathbf{G}_d\left(s, \tau_d\right) = e^{-s\tau_d}\mathbf{G}(s) + \frac{(1 - e^{-s\tau_d})}{s}P_{max}; \quad \tau_d = \frac{-\Delta/2 + \delta - \widetilde{SoC}_d}{P_{max} - P_{nom}} \tag{3.9c}$$

Aggregate response of all the chargers in the four regions '$a - d$' will be

$$\mathbf{P}_a(s) = N\int_{-\Delta/2+\delta}^{\Delta/2} f_{on}\mathbf{G}_a\left(s, \tau_a\right) d\widetilde{SoC}_a \tag{3.10}$$

$$\mathbf{P}_b(s) = N\int_{-\Delta/2+\delta}^{\Delta/2} f_{off}\mathbf{G}_b\left(s, \tau_b\right) d\widetilde{SoC}_b \tag{3.11}$$

$$\mathbf{P}_c(s) = N\int_{-\Delta/2}^{-\Delta/2+\delta} f_{on}\mathbf{G}_c\left(s, \tau_c\right) d\widetilde{SoC}_c \tag{3.12}$$

$$\mathbf{P}_d(s) = N\int_{-\Delta/2}^{-\Delta/2+\delta} f_{off}\mathbf{G}_d\left(s, \tau_d\right) d\widetilde{SoC}_d \tag{3.13}$$

and the whole population's aggregate response

$$\mathbf{P}_{tot}(s) = \left(\mathbf{P}_a(s) + \mathbf{P}_b(s) + \mathbf{P}_c(s) + \mathbf{P}_d(s)\right). \tag{3.14}$$

After linearizing about the steady-state power consumption $P_{ss} = N_{on}P_{max}$,

$$\widetilde{\mathbf{P}}_{tot}(s) = \mathbf{P}_{tot}(s) - \frac{P_{ss}}{s} \tag{3.15}$$

$$\approx \left(\frac{I_0}{s + \sigma'} + \frac{A_\Delta}{\left(s + \sigma\right)^2 + \omega^2}\right)\delta \tag{3.16}$$

with

$$I_0 = (P_{max} - P_{nom})\, N/\Delta \tag{3.17}$$

$$\omega = \frac{2\sqrt{15}P_{nom}\,(P_{max} - P_{nom})}{\Delta\sqrt{P_{max}^2 + 2P_{nom}P_{max} - 2P_{nom}^2}} \tag{3.18}$$

$$A_\Delta = \frac{10\sqrt{15}P_{nom}^2\,(P_{max} - P_{nom})^2\, N}{\Delta\,(P_{max}^2 + 2P_{nom}P_{max} - 2P_{nom}^2)^{3/2}}. \tag{3.19}$$

The transfer function of the response would be

$$\mathbf{T}(s) = \frac{s\ I_0}{s + \sigma'} + \frac{s\ A_\Delta}{(s+\sigma)^2 + \omega^2} \tag{3.20}$$

where $\sigma'$ and $\sigma$ are damping parameters associated with heterogeneity and noise and are to be estimated real-time [2]. This is the response to a *right* shift in deadband where the nominal $SoC$ profile increases. However, a similar analysis can be done for a *left* shift (i.e. $\delta < 0$) as well, in which case the transfer function comes out to have a similar form with $I_0 = P_{nom}N/\Delta$. Fig. 3.7(a) and Fig. 3.7(b) show the comparison of the model with the simulation for a right and left shift, respectively, of the deadband. The discrepancies in the two responses could be attributed to the non-homogeneity in the system.

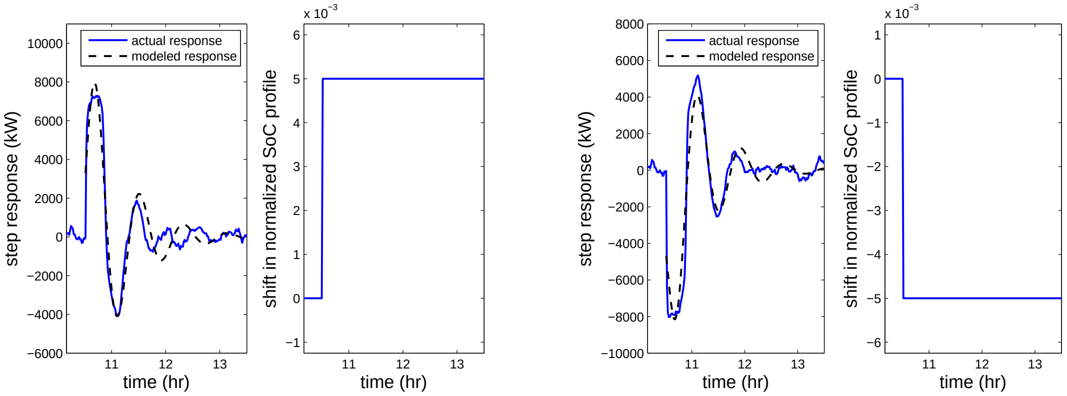

(a) Shifting the deadband towards right.

(b) Shifting the deadband towards right.

Figure 3.7: Comparison of the model performance with Monte-Carlo simulation.

---

[2] For this particular system, $\sigma' = 0.2$ and $\sigma = 0.025$.

## 3.3 Control Design and Results

### 3.3.1 Control Law

The system with transfer function (3.20) can be modeled into a state-space form as

$$\dot{x} = \mathbf{A}x + \mathbf{B}u \tag{3.21}$$

$$y = \mathbf{C}x + Du \tag{3.22}$$

where the input $u(t) \in \mathbb{R}$ is the shift in the deadband, and the output $y(t) \in \mathbb{R}$ is the aggregate power demand linearized about the steady-state value, $P_{ss}$, and the states are $x \in \mathbb{R}^{3\times 1}$. The state-space matrices are given by

$$\begin{aligned}
\mathbf{A} &= \begin{pmatrix} 0 & 0 & -\sigma^{'}\left(\sigma^2+\omega^2\right) \\ 1 & 0 & -\left(2\sigma\sigma^{'}+\sigma^2+\omega^2\right) \\ 0 & 1 & -\left(\sigma^{'}+2\sigma\right) \end{pmatrix} \\
\mathbf{B} &= \begin{pmatrix} -I_0\sigma^{'}\left(\sigma^2+\omega^2\right) \\ A_\Delta\omega\sigma^{'} - 2I_0\sigma\sigma^{'} \\ A_\Delta - I_0\sigma^{'} \end{pmatrix} \\
\mathbf{C} &= \begin{pmatrix} 0 & 0 & 1 \end{pmatrix} \\
D &= \begin{cases} \left(P_{max} - P_{nom}\right) N/\Delta, & u(t) \leq 0 \\ P_{nom} N/\Delta, & u(t) < 0 \end{cases}
\end{aligned}$$

To design the control law, a sliding surface $S(t)$ is defined [74]

$$S(t) := e(t) + c_i \int_0^t e\left(\tau\right) d\tau, \quad c_i > 0 \tag{3.23}$$

$$\text{where,} \quad e(t) = y(t) - y_d(t), \tag{3.24}$$

$y_d(t)$ being the desired linearized trajectory. The aim is to design a control input $u(t)$ that satisfies the relation $\dot{S}(t) = -\eta S(t), \eta > 0$. However because of the presence of the non-zero scalar $D$ in (3.22), $\dot{S}(t)$ will have both $u(t)$ and $\dot{u}(t)$. To resolve this, an estimate of $u(t)$ is calculated by equating $e(t) = 0$ and then the estimate is used to compute $\dot{u}$ from $\dot{S}(t) = -\eta S(t)$, according to

$$\hat{u}(t) = \frac{\left(y_d(t) - \mathbf{C}x(t)\right)}{D} \tag{3.25}$$

$$\dot{u}(t) = \frac{\left(-\eta S(t) - c_i e(t) + \dot{y}_d(t) - \mathbf{CA}x(t) - \mathbf{CB}\hat{u}(t)\right)}{D}. \tag{3.26}$$

Carefully choosing the design variables $\eta$ and $c_i$ will guarantee exponential convergence of the error $e(t)$ to zero (see Appendix B). A linear estimator has been used to estimate the state $x(t)$ appearing in (3.25)-(3.26).

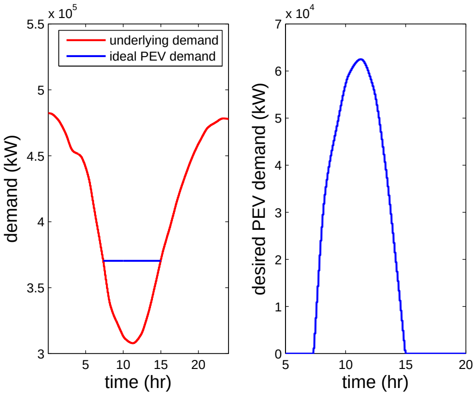

Figure 3.8: An ideal valley-filling profile.

### 3.3.2 Controller Performance

Fig. 3.8 (left) shows a typical overnight base demand (scaled down to suit our example) in summer for the region managed by the Midwest Independent System Operator (MISO). An ideal valley-filling charging strategy would be to fill the valley by a flat demand curve and at the same time ensure that all the vehicles are fully charged by a stipulated time (say, 8 AM or 20:00 hr. in this case). It is assumed that a complete knowledge of each vehicle - maximum charging rate and amount of charge required that night, is available. If $d(t)$ be the base (non-PEV) demand and $E_{max,i}$ the charge requirement of $i^{th}$ PEV, then the optimal *flat* demand level, $P_{des}$ and the optimal charging start and completion time instants, $t_0$ and $t_f$, can be computed by iteratively solving the relation

$$\int_{t_0}^{t_f} (P_{des} - d(t))\, dt = \sum_{i=1}^{N} E_{max,i} \tag{3.27}$$

And the valley-filling optimal PEV demand is then given by

$$y_d(t) = \begin{cases} P_{des} - d(t), & \text{if} \quad t \in [t_0,\ t_f] \\ 0, & otherwise \end{cases} \tag{3.28}$$

as shown in the in Fig. 3.8 (right). An alternative approach to determining the optimal charging trajectory $y_d$ is presented in [75]. In that case, all PEVs seek to minimize their charging costs, and in so doing achieve a Nash equilibrium that establishes the globally optimal charging trajectory.

Fig. 3.9 shows the closed loop performance of the controller for different reference trajectories and the corresponding control inputs. In Fig. 3.9(a) the aggregate PEV demand tracks the ideal valley-filling trajectory found in Fig. 3.8. Fig. 3.9(b) shows tracking of a reference trajectory which experiences a “step” decrease midway through the charging period. This situation could occur when there is a sudden increase in the non-PEV electricity demand or a sudden loss of a generator. In this case there is significant non-zero PEV demand beyond the optimal charge-completion time $t_f$. This non-zero power demand compensates for the reduced charging rates that occurred in response to the step decrease in the reference trajectory. In Fig. 3.9(c) the aggregate PEV demand tracks a fluctuating reference trajectory which may arise from wind generation.

It is interesting to note the large control input that is required towards the end of the charging process. This can be attributed to the fact that as the charge completion time approaches, more and more vehicles become fully charged and hence take no further part in the closed loop control. This results in a loss of controllability.

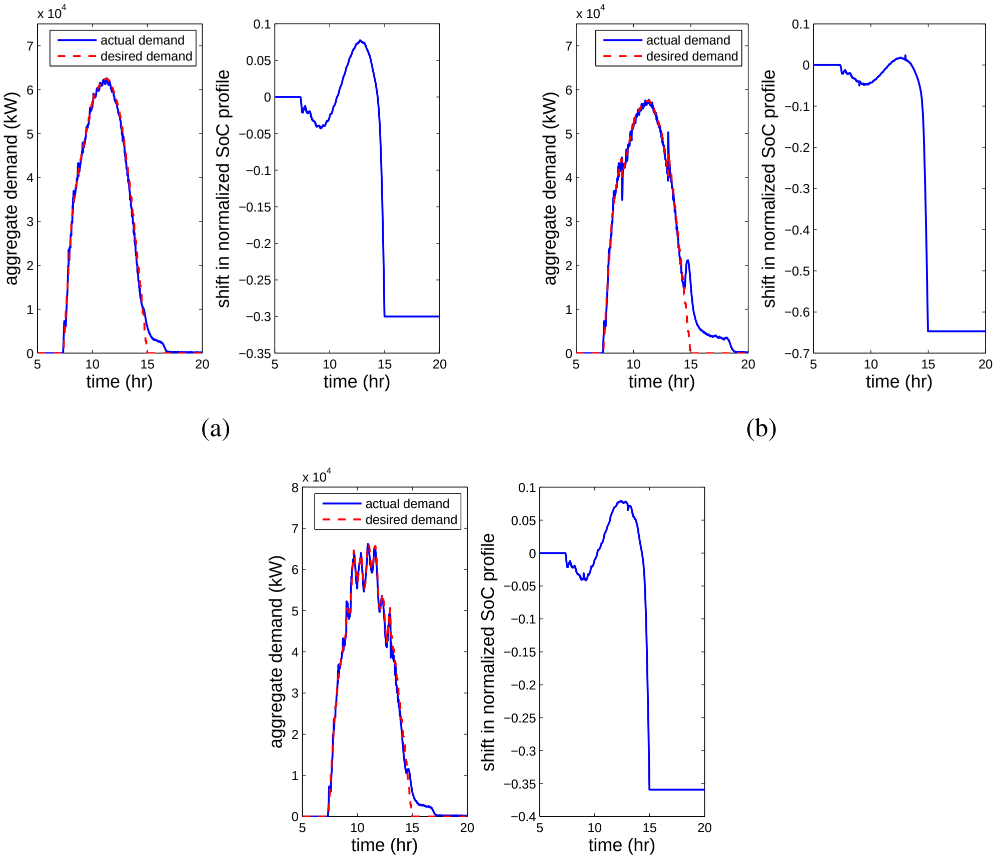

(a)

(b)

(c)

Figure 3.9: Tracking performance of the controller in response to varying trajectories.

## 3.4 Summary

In this work a large population of PEVs has been considered and it is assumed that a fairly complete knowledge of their battery's charge requirement and the maximum charging rate is available. A hysteresis-based charging method has been proposed. A linearized model of aggregate response of PEV chargers to a shift in the hysteresis deadband has been developed. A nonlinear feedback controller has been shown to fulfill the objectives of tracking a valley-filling PEV demand and fluctuations in generation. It has been observed that the controllability of the system is low towards the start and end of the charging duration. As the charge completion time approaches, more and more vehicles become fully charged and hence take no further part in the closed loop control thereby resulting in a loss of controllability. Further research should be done to address these issues and possibly come up with a better model to utilize the full potential of PEV charging.

# CHAPTER IV

# Analysis of Synchronized Tripping of PEV Chargers

Plug-in electric vehicle (PEV) charging equipment incorporates protection that ensures grid disturbances do not damage the charger or vehicle. When the grid voltage sags below 80% of nominal, under-voltage protection is likely to disconnect the charging load from the grid. Most PEV charging will occur overnight, when non-PEV load is at a minimum. PEV voltage-sag response, when synchronized across large numbers of PEVs, could result in the loss of a significant proportion of the total load. It is shown that this load loss can lead to unacceptably high voltages once the initiating event has been cleared. The objective is to explore the nature of this voltage-rise phenomenon and develop analysis tools to assist in determining PEV loading conditions that demarcate acceptable post-disturbance voltage response from unacceptable outcomes.

When electricity demand is composed of large numbers of similar devices, relatively benign events can synchronize their response, resulting in collective behavior that is potentially destabilizing, such as fault-induced delayed voltage recovery (FIDVR) [39], voltage-sag induced synchronized stalling of residential air-conditioner compressors may lead to a cascading form of voltage collapse. We show that if the penetration of PEV charging load is sufficiently high, synchronized tripping of PEV chargers may lead to unacceptably high voltages on distribution feeders. The response of PEV chargers to power quality events is governed by SAE Standard J2894 [76], which updates an earlier EPRI report [77]. But situations where voltage sags below 80%, but remains non-zero, are not explicitly covered by the standard. Such voltage sags are not uncommon on distribution systems. For example, FIDVR events generally occur when voltage falls to around 60-65% of nominal, as that is the voltage at which residential air-conditioner compressors tend to stall [78]. We therefore take the view that distribution networks will experience voltage sags that are sufficient to cause large numbers of PEV chargers to trip. Following such trips, J2894 recommends that restarting be delayed, so as to minimize the possibility of cold load pickup. Because of mostly overnight charging, PEV charging load could be a relatively high proportion of the total load on a distribution feeder during overnight hours. Accordingly, a voltage sag that tripped PEV chargers would cause a significant reduction in the load. Upon recovery from the voltage sag, the feeder would experience much lighter load, and consequently voltages

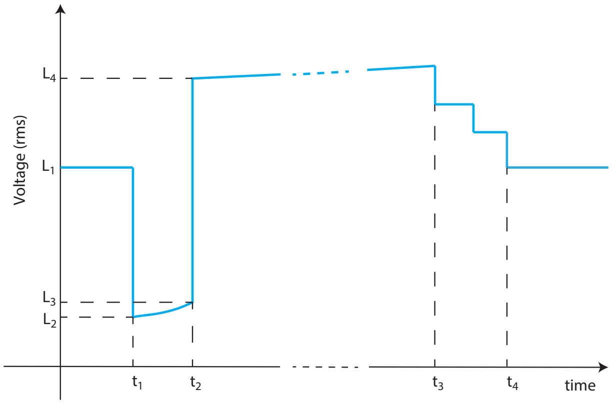

Figure 4.1: Post-fault voltage rise due to tripping of PEV chargers.

would rise above nominal. Shunt capacitors, which are common on distribution feeders, would further contribute to the post-sag voltage rise. A significant voltage rise, perhaps above $110\%$ of nominal, could cause other electrical equipment to trip. In fact, J2894 allows PEV chargers to trip for voltages above $110\%$ of nominal. The high voltages resulting from such a cascade could damage distribution equipment and the remaining load.

## 4.1 Motivating Example

A voltage sag is a relatively common occurrence that can happen due to many reasons, e.g. a distant fault in the grid, a sudden increase in load (high start-up current of many equipments). The response of PEV chargers to a voltage sag or a momentary outage is specified in the standards [76, 77]. An EV charger should be able to ride through a sag of $80\%$ nominal voltage for 2s and a momentary outage ($0\%$ nominal voltage) for 12 cycles. If the voltage sag (or outage) is longer than that, chargers are free to trip. Once tripped, the charging can be restarted only after a delay of at least 2 min and, moreover, the restart time has to be randomized over a period of several minutes (e.g. 10 min) to avoid any “cold load pick-up”. Hence on fault clearance the line voltage would increase beyond nominal because of the reduced electricity demand. Fig. 4.1 depicts a typical such scenario. On initiation of a voltage sag (or, a momentary outage) at time $t_1$ the line voltage drops from nominal level $L_1$ to some level $L_2$. If the sag continues for longer than a critical duration (e.g. 12 cycles in case of an outage) the PEV chargers on-line would trip resulting in a slight increase in line voltage from $L_2$ to $L_3$. Subsequently on fault clearance at time $t_3$ (typically after a few hundred milliseconds) the voltage recovers but, due to loss of load, increases to a level $L_4$ which is above the nominal $L_1$. Beyond this point the line voltage regulators would start to react. Usually in any distribution feeder, there would be a sequence of tap-changing regulators which react to voltage swings with a time delay of few tens of seconds [79–81]. While the fast regulators (often using inverse time delay) usually has a minimum time delay of 15 s, most of the line regulators would have a minimum time delay

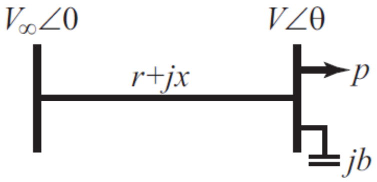

Figure 4.2: Two-bus network.

of 30-60 s. Depending on the time delay of the tap changers, at some time $t_4$, the voltage would start to fall back down to the nominal value, $L_1$, through a sequence of tap changes, with each tap-change action adding a inter-tap delay of typically a few seconds.

The simple two-bus network of Figure 4.2 will be used to provide an initial illustration of voltage rise associated with PEV charger tripping. For this simple system, the relationship between active power load $p$, susceptance $b$, and load-bus voltage $V$ can be written as,

$$F(p,b,V;r,x,V_\infty) = \Big((1-bx)^2 + (br)^2\Big)V^4 + \big(2pr - V_\infty^2\big)V^2 + p^2\big(r^2+x^2\big) = 0. \tag{4.1}$$

An outline of the derivation of (4.1) is provided in Appendix C. The relationship between $p$, $b$ and $V$ is shown graphically [1] in Figure 4.3, where each line corresponds to a particular value of voltage $V$, and can be thought of as a contour of the $(p,b,V)$-surface [82, 83].

We also desire base-case conditions of $p = 0.5$ pu and $V = 1.0$ pu. The capacitive susceptance required to achieve these loading conditions can be determine from (4.1) as $b = 0.46$ pu. This base-case point is identified on the surface of Figure 4.3. If the load power $p$ were to reduce, while holding susceptance $b$ constant, the operating point would move horizontally to the left, crossing contours of higher and higher voltage. For a sufficiently large loss of load $p$, the operating point would move to the unacceptable operating region where $V > 1.1$ pu. By setting $V = 1.1$ pu in (4.1), the value of load at which voltage becomes unacceptable can be found to be $p = 0.364$ pu. Therefore, in this example, if $(0.5-0.364)/0.5 = 27\%$ of the original load tripped, the voltage at the load bus would rise from 1.0 pu to 1.1 pu.

## 4.2 Basic Framework

In order to extend analysis from the two-bus case of Section 4.1 to realistic distribution feeders, we will consider the radial network structure shown in Figure 4.4. Node 1 denotes the substation bus at the source of the feeder, while load nodes $2,...,n$ are arranged so that node number increases along paths from the substation to the end nodes. The set of feeder nodes is given by $\mathcal{N} = \{1,...,n\}$. Let $\mathcal{C}$ be the set of all connections between nodes, so

---

[1] Parameter values are $V_\infty = 1.0$ pu, $r = 0.3$ pu and $x = 0.5$ pu.

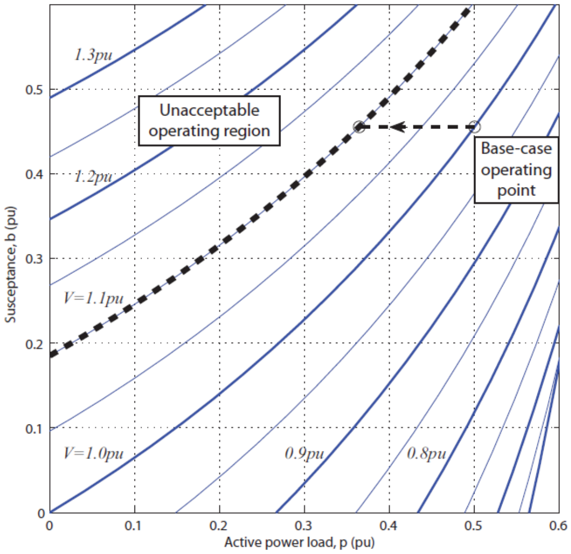

Figure 4.3: Relationship between load power $p$, susceptance $b$ and voltage $V$.

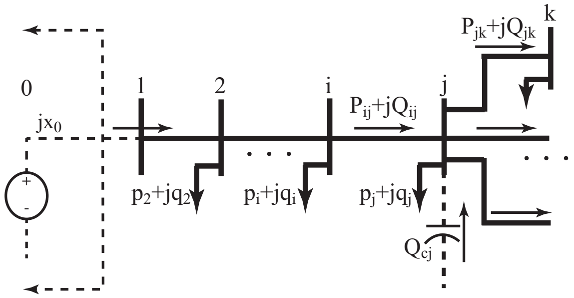

Figure 4.4: Radial structure of a distribution feeder.

that $(i, j) \in \mathcal{C}$ if a physical connection exists between nodes $i$ and $j$. We also define,

$$\mathcal{C}_i = \{j : (i, j) \in \mathcal{C}, i < j\}$$

as the set of all nodes that are connected "downstream" from node $i$. The complex power drawn by the load at node $i$ is denoted $p_i + jq_i$, whereas $P_{ij}$ and $Q_{ij}$ are the active and reactive power flowing from node $i$ towards node $j \in \mathcal{C}_i$ through the connecting branch $(i, j)$. The impedance of that branch is $z_{ij} = r_{ij} + jx_{ij}$.

We have modeled the load at each node as constant power, though it could just as easily be modeled as a combination of constant power, current and impedance, the familiar ZIP model [84]. The reactive power produced by a shunt capacitor $b_i$ at node $i$ is given by $Q_{ci} = b_i V_i^2$. A Thévenin equivalent has been used to model the grid from generation to the feeder source node 1. Source reactance is given by $x_0$, with source resistance neglected.

It is convenient to model radial feeders of the form shown in Figure 4.4 using the

*DistFlow* [85] recursive power flow equations,

$$P_{ij} = \sum_{k \in \mathcal{C}_j} P_{jk} + r_{ij}\left(P_{ij}^2 + Q_{ij}^2\right)/V_i^2 + p_j \tag{4.2}$$

$$Q_{ij} = \sum_{k \in \mathcal{C}_j} Q_{jk} + x_{ij}\left(P_{ij}^2 + Q_{ij}^2\right)/V_i^2 + q_j - b_j V_j^2 \tag{4.3}$$

$$V_j^2 = V_i^2 - 2\left(r_{ij}P_{ij} + x_{ij}Q_{ij}\right) + \frac{\left(r_{ij}^2 + x_{ij}^2\right)\left(P_{ij}^2 + Q_{ij}^2\right)}{V_i^2}. \tag{4.4}$$

For later use, we define,

$$\begin{aligned} \mathbf{P} &= \left\{P_{ij} : (i,j) \in \mathcal{C}\right\} \\ \mathbf{Q} &= \left\{Q_{ij} : (i,j) \in \mathcal{C}\right\} \\ V &= \left\{V_i : i \in \mathcal{N}\right\} \\ p &= \left\{p_i : i \in \mathcal{N}\right\} \\ q &= \left\{q_i : i \in \mathcal{N}\right\} \\ b &= \left\{b_i : i \in \mathcal{N}\right\}, \end{aligned}$$

and write (4.2)-(4.4) compactly as

$$F(\mathbf{P}, \mathbf{Q}, V; p, q, b) = 0.$$

The DistFlow equations (4.2)-(4.4) can be solved iteratively. Assuming a flat start, with $V_i = 1.0$ pu for all $i \in \mathcal{N}$, the flows $P_{ij}$ and $Q_{ij}$ can be computed using (4.2) and (4.3) by starting at the extremities of the feeder (the nodes farthest from the source) and working back towards the source. Those values can then be used in (4.4) to update voltages $V_i$, starting from the known source voltage $V_0 = 1.0$ pu, and proceeding outwards to the end nodes. The process is then repeated using the updated voltages.

The load at each node is comprised of both non-PEV base load and PEV charging load. We assume that the active power drawn by PEV chargers at node $i$ accounts for a fraction $\beta_i$ of the total active power consumption at that node. The power factor of the PEV charging load is $pf_i$.[2] Therefore the PEV load is given by,

$$p_{pev,i}(\beta_i) + jq_{pev,i}(\beta_i) = \beta_i p_i \left(1 + j\frac{\sqrt{1 - pf_i^2}}{pf_i}\right) \tag{4.5}$$

---

[2] In later studies, we will assume that all PEV charging loads have a power factor of $pf_i = 0.97$, which is consistent with [76]. This is not a restrictive assumption though.

and the non-PEV load is given by,

$$p_{npev,i}(\beta_i) + jq_{npev,i}(\beta_i) = (1-\beta_i)p_i + j\left(q_i - \beta_i p_i \frac{\sqrt{1-pf_i^2}}{pf_i}\right). \tag{4.6}$$

In later formulations, we will use the notation,

$$\begin{aligned} p_{npev}(\beta) &= \{p_{npev,i}(\beta_i); i \in \mathcal{N}\} \\ q_{npev}(\beta) &= \{q_{npev,i}(\beta_i); i \in \mathcal{N}\}. \end{aligned}$$

## 4.3 Problem Formulation

In the two-bus example considered in Section 4.1, determining the relationship between loss of load and consequent voltage rise involved a two-step process:

A. For a given total load (non-PEV plus PEV), the susceptance $b$ required to achieve the desired pre-disturbance voltage was determined.

B. With susceptance fixed at the value determined in step 1), the load reduction required for the voltage to reach the maximum allowable voltage of 1.1 pu was then calculated.

This process is straightforward for the two-bus case, and can be implemented by coupling together two copies of (4.1), with the pre-disturbance values for $p$ and $V$ specified in the first equation, and the voltage threshold $V = 1.1$ pu specified in the second equation. This results in two equations in two unknown variables, the susceptance $b$ and the reduced load $p_{red}$. The critical proportion of PEV charging load is then given by $\beta_{crit} = (p - p_{red})/p$. This formulation provides a direct mapping from $p$ to $\beta_{crit}$.

We desire such a mapping for general multi-node networks of the form shown in Figure 4.4. Some adaptation of the two-step process is required, with the following subsections describing a generalized approach.

### 4.3.1 Pre-disturbance conditions

In establishing pre-disturbance conditions, it is assumed that the feeder normally operates with all node voltages within allowable bounds, for example $\pm 2\%$ of nominal [86], and that power losses are minimized. These requirements can be achieved by placing shunt capacitor banks along the feeder. Capacitor placement and sizing strategies have been extensively studied, with both heuristic guidelines [87–89] and optimization techniques [85, 90] widely used. For our studies, we have adopted the approach suggested in [87], and sized the capacitors using an optimization formulation that minimizes line losses,

$$\min_{b} \quad \mathcal{L}(\mathbf{P}, \mathbf{Q}, V) = \sum_{(i,j)\in\mathcal{C}} r_{ij}\big(P_{ij}^2 + Q_{ij}^2\big)/V_i^2 \tag{4.7}$$

subject to

$$F(\mathbf{P}, \mathbf{Q}, V; p, q, b) = 0 \tag{4.8}$$

$$0.98 \leq V_i \leq 1.02, \qquad \forall i \in \mathcal{N}. \tag{4.9}$$

Reliable convergence was obtained through an iterative approach that makes use of CVX [91]. The voltage bounds may, however, occasionally lead to infeasibility. In such cases, they may need to be relaxed slightly.

### 4.3.2 Post-disturbance voltage rise

Under post-disturbance conditions, with some of the PEV load disconnected due to the voltage-sag event, voltages across the distribution feeder will tend to be higher than normal. It is assumed that the status of shunt capacitors does not change during the event, so the values of $b$ obtained from the optimization (4.7)-(4.9) will remain fixed. The goal is to determine the smallest loss of PEV charging load across the feeder that would cause the voltage at any of the nodes hit its limiting value of 1.1 pu. This problem can be addressed using the optimization formulation,

$$\min_{\beta} \quad \sum_{i \in \mathcal{N}} \beta_i p_i \tag{4.10}$$

subject to

$$F\big(\mathbf{P}, \mathbf{Q}, V; p_{npev}(\beta), q_{npev}(\beta), b\big) = 0 \tag{4.11}$$

$$\max\{V\} = 1.1. \tag{4.12}$$

To overcome the non-convexity inherent in (4.12), we constrain a single node voltage at a time, replacing (4.12) by a constraint of the form $V_i = 1.1$ pu. This is effective as usually only a few nodes are candidates for the highest voltage. If we force a node voltage to 1.1 pu, and notice that other nodes have higher voltages, then the optimization is repeated with the voltage constraint enforced for the node with the highest voltage. With some prior knowledge of likely high-voltage buses, we have found that this procedure only needs to be repeated once or twice.

## 4.4 Case Studies

Two distribution feeder examples will be used to illustrate, in a practical setting, the risk of overvoltages as PEV charging load increases. The first is an existing 23 kV feeder that has no lateral branches [87], and the second is the standard IEEE-34 distribution feeder [92].

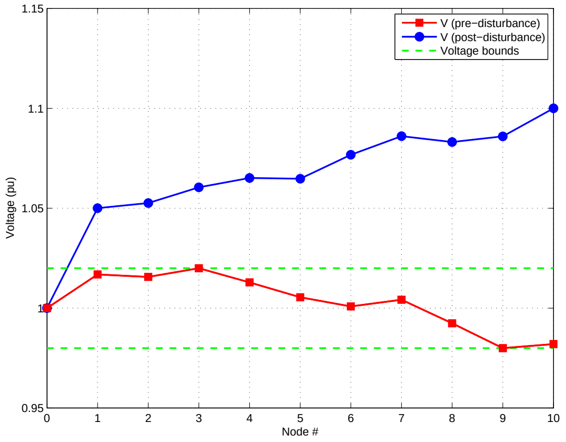

Figure 4.5: Pre- and post-disturbance voltage profile along the 10-node primary feeder.

### 4.4.1 23 kV 10-node primary feeder

The feeder data for this example were obtained from [87]. The feeder was modified to include the Thévenin equivalent representation of the grid, in accordance with Figure 4.4. The load was scaled up by 20% uniformly across the feeder to account for general load growth as well as increased penetration of PEVs. Shunt capacitors were placed at nodes 7 and 10 to ensure pre-disturbance voltages remained within allowable bounds of $\pm 2\%$. The base-case voltage profile is shown in Figure 4.5. It is clear that all voltages are acceptable prior to the loss of PEV charging load. Figure 4.5 also illustrates the rise in voltage that occurs when PEV load is disconnected. For this particular case, 31.8% of the load at every node was tripped. This resulted in the voltage at node 10, which is farthest from the substation, rising to exactly 1.1 pu.

To further investigate the characteristics of this feeder, three different scenarios have been considered.

#### 4.4.1.1 Uniform PEV charging load

For this case, it was assumed that the PEV charging load was spread uniformly across the feeder, such that the PEV load fraction $\beta_i$ was the same for every node. By setting $\beta_i = \hat{\beta}, \forall i \in \mathcal{N}$, the constraints (4.11)-(4.12) form a set of equations that has dimension equal to the number of variables. As a result, an iterative solution process, similar to that described in Section 4.2 for the DistFlow equations, can be used to directly find the critical value $\hat{\beta}_{crit}$ that corresponds to $\max(V) = 1.1$ pu.[3] This value separates acceptable cases ($\hat{\beta} < \hat{\beta}_{crit}$) from unacceptable situations ($\hat{\beta} > \hat{\beta}_{crit}$).

To explore different loading scenarios, for example daily load variations, the total load on the feeder was scaled from 100% to 135% of the load data given in [87]. Shunt ca-

---

[3] Constraint switching associated with (4.12) can be handled in a similar way to that described in Section 4.3.2.

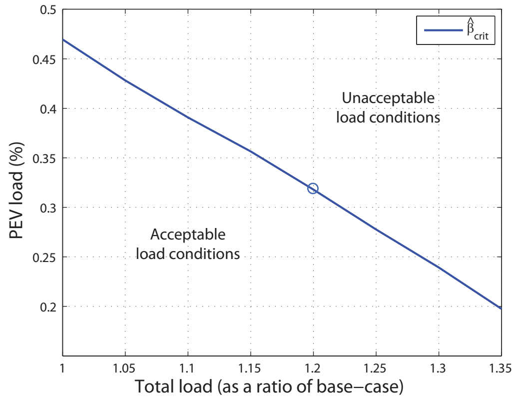

Figure 4.6: Allowable PEV load as total load increases, with $\beta_i$ uniform across the 10-node primary feeder.

pacitors were sized using (4.7)-(4.9) whenever they were required to improve the pre-disturbance voltage profile along the feeder. The value of $\hat{\beta}_{crit}$ was calculated at each loading level, and is plotted in Figure 4.6. The voltage profile shown in Figure 4.5 corresponds to the point marked '**o**' in Figure 4.6. Any point above the curve describes an unacceptable loading condition, as the post-disturbance voltage of at least one node exceeds 1.1 pu. Loading conditions below the curve result in acceptable post-disturbance voltages. It may be concluded from Figure 4.6 that for high loading levels, the rise in voltage following a disturbance may be excessive even when the PEV charging load penetration is quite low.

#### 4.4.1.2 Sensitivity to location

The location of PEV charging load along a distribution feeder has an important influence on post-disturbance voltage rise. The effect of load loss tends to become magnified as the distance from the substation increases. The relative significance of different locations can be determined through the use of (4.11)-(4.12). Consider an investigation of PEV load at two locations, nodes $i$ and $j$. The corresponding values of $\beta_i$ and $\beta_j$ are free variables in (4.11), while $\beta_k, k \neq i, j$, are fixed for all other nodes. This leads to (4.11)-(4.12) having one more variable than constraint. This under-determined set of equations describes a 1-manifold (or curve) which can be obtained using a continuation process [93]. The simplest approach is to assign a series of values to $\beta_i$ and use (4.11)-(4.12) to calculate the corresponding values for $\beta_j$. The resulting curve separates acceptable loading conditions (below the curve) from those that would leave the system vulnerable to post-disturbance overvoltages (above the curve).

This procedure was used to compare the relative importance of PEV loads at nodes 6 and 10 in the 10-node feeder. The results are shown in Figure 4.7 for two different background loading conditions, 1) all loads were scaled to 120% of their base-case values in [87], and 2) all loads were scaled by 130%. The proportion of PEV charging load at

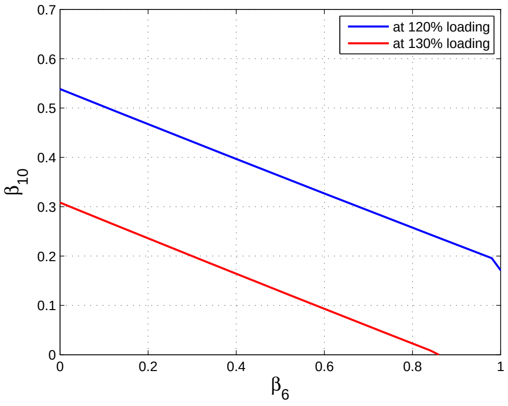

Figure 4.7: Sensitivity between $\beta_6$ and $\beta_{10}$ for two loading scenarios on the 10-node primary feeder.

all nodes other than 6 and 10 was held at $\beta_k = 0.25, k \neq 6, 10$. The relationship between $\beta_6$ and $\beta_{10}$ is very close to affine, with both lines in Figure 4.7 having slopes of approximately -0.36. It follows that the load at node 10 has a much more significant influence on the overvoltage phenomenon of interest. Even though the result is to be expected in this case, as node 10 is at the very end of the feeder, this process provides a valuable analysis tool for cases that are not so straightforward.

#### 4.4.1.3 Maximum vulnerability

The optimization formulation (4.10)-(4.12) determines the minimum PEV load loss necessary to cause unacceptable post-disturbance voltages. This effectively establishes the locations where loss of PEV load contributes most to voltage rise. Table 4.1 presents the results of this optimization for a range of background loading conditions, from the load profile given in [87] to a 35% increase beyond that base level. In all cases, it can be seen that the network is most vulnerable to overvoltages when PEV load is located near the remote end of the feeder. The proportion of PEV load relative to the total feeder load is given by $\sum_i \beta_i p_i / \sum_i p_i$, with values for the various loading conditions given in the last row of the table. For the 135% loading condition, overvoltage vulnerability occurs when PEV charging load accounts for only 8.9% of the total load. However problems will only arise if all that load is placed at the end of the feeder.

To explore a more reasonable distribution of PEV load, the optimization problem (4.10)-(4.12) was augmented by the additional constraint,

$$\beta_i \leq 0.5 \forall i \in \mathcal{N} \tag{4.13}$$

From the results in Table 4.2, tt is again clear that the network is more vulnerable to overvoltages when PEV loads are further from the substation. Based on the scenarios presented

Table 4.1: Minimum PEV charging load necessary to cause unacceptable post-disturbance voltages on the 10-node primary feeder.

| Node # | % loading | | | | | | | |
|---|---|---|---|---|---|---|---|---|
| | 100 | 105 | 110 | 115 | 120 | 125 | 130 | 135 |
| 2 | 0 | 0 | 0 | 0 | 0 | 0 | 0 | 0 |
| 3 | 0 | 0 | 0 | 0 | 0 | 0 | 0 | 0 |
| 4 | 0 | 0 | 0 | 0 | 0 | 0 | 0 | 0 |
| 5 | 0 | 0 | 0 | 0 | 0 | 0 | 0 | 0 |
| 6 | 0 | 0 | 0 | 0 | 0 | 0 | 0 | 0 |
| 7 | 0 | 0 | 0 | 0 | 0 | 0 | 0 | 0 |
| 8 | 0 | 0 | 0 | 0 | 0 | 0 | 0 | 0 |
| 9 | 0.845 | 0.60 | 0.382 | 0.184 | 0 | 0 | 0 | 0 |
| 10 | 1.0 | 1.0 | 1.0 | 1.0 | 0.982 | 0.875 | 0.775 | 0.672 |
| $\frac{\sum_i \beta_i p_i}{\sum_i p_i}$ | 0.200 | 0.180 | 0.163 | 0.147 | 0.130 | 0.116 | 0.103 | 0.089 |

in Table 4.2, a relatively small amount of PEV charging load is required for overvoltage vulnerability. Considering the 120% loading case, for example, unacceptable overvoltages may occur when only 17.2% of the load is due to PEV charging.

### 4.4.2 IEEE-34 test feeder

Similar analysis has been undertaken for the IEEE-34 distribution test feeder [92]. This is an actual 24.9 kV feeder in Arizona that is long and lightly loaded. PEV-induced overvoltage effects are more prominent in this feeder because of its long lines. Nodes 822 and 890 were chosen as shunt capacitor locations, whenever needed. Pre-fault acceptable voltage range (4.9) was relaxed a bit to $0.97 - 1.05\ pu$. Also a Thévenin equivalent, represented by node '0', of the higher-voltage grid was incorporated. For most part of the analysis a single-phase approximation of the three-phase feeder model has been used. We will henceforth do most of the analysis on the single-phase model, before finishing with a brief look into the three-phase case.

#### 4.4.2.1 Uniform PEV charging load

As in Section 4.4.1.1, this initial study assumed that PEV charging load was spread uniformly across the feeder, so $\beta_i = \hat{\beta}, \forall i \in \mathcal{N}$. Figure 4.8 shows the variation in the critical value $\hat{\beta}_{crit}$ as the total load on the feeder was decreased from 100% of the base case [92] to 70%. Recall that $\hat{\beta}_{crit}$ corresponds to a post-disturbance voltage profile where $\max\{V\} = 1.1$ pu. For each loading scenario, source node voltage and the regulator tap-ratios were adjusted to keep the substation voltage at $1.05\, p.u.$ and the voltages at nodes 850 and 832 close to $1.021\, p.u.$ and $1.035\, p.u.$, respectively. Figure 4.9 shows the pre- and post-disturbance voltage profiles for the case where load scaling is 100% and $\hat{\beta}_{crit} = 0.0764$.

Table 4.2: Repeat of Table 4.1, subject to the constraint $\beta_i \leq 0.5,\ \forall i$.

| Node # | % loading | | | | | | | |
|---|---|---|---|---|---|---|---|---|
| | 100 | 105 | 110 | 115 | 120 | 125 | 130 | 135 |
| 2 | 0 | 0 | 0 | 0 | 0 | 0 | 0 | 0 |
| 3 | 0.139 | 0 | 0 | 0 | 0 | 0 | 0 | 0 |
| 4 | 0.5 | 0 | 0 | 0 | 0 | 0 | 0 | 0 |
| 5 | 0.5 | 0.418 | 0 | 0 | 0 | 0 | 0 | 0 |
| 6 | 0.5 | 0.5 | 0.459 | 0.190 | 0 | 0 | 0 | 0 |
| 7 | 0.5 | 0.5 | 0.5 | 0.5 | 0.309 | 0 | 0 | 0 |
| 8 | 0.5 | 0.5 | 0.5 | 0.5 | 0.5 | 0.374 | 0.105 | 0 |
| 9 | 0.5 | 0.5 | 0.5 | 0.5 | 0.5 | 0.5 | 0.5 | 0.361 |
| 10 | 0.5 | 0.5 | 0.5 | 0.5 | 0.5 | 0.5 | 0.5 | 0.5 |
| $\frac{\sum_j \beta_j p_j}{\sum_j p_j}$ | 0.397 | 0.303 | 0.244 | 0.209 | 0.172 | 0.141 | 0.116 | 0.095 |

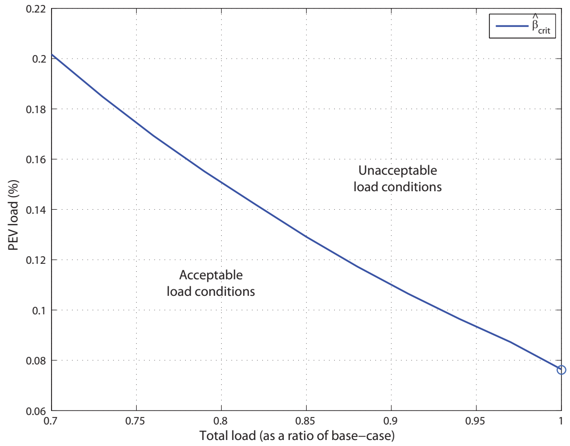

Figure 4.8: Allowable PEV load as total load increases, with $\beta_i$ uniform across the 34-node feeder.

This particular loading condition is identified on the curve in Figure 4.8 by a '**o**'.

#### 4.4.2.2 Sensitivity to location

The continuation process described in Section 4.4.1.2 was used to compare the relative importance of PEV loads at nodes 844 and 890, which are on different spurs of the 34-node feeder. The proportion of PEV load at all other nodes was held constant at $\beta_i = 0$. The results for two loading conditions, 70% and 80% of base case, are presented in Figure 4.10. As with the 10-node feeder, the relationship displayed in Figure 4.10 is almost affine. In this case, though, the lines have a slope of -0.85. It may be concluded that PEV load at both locations has almost the same influence on post-disturbance voltage rise.

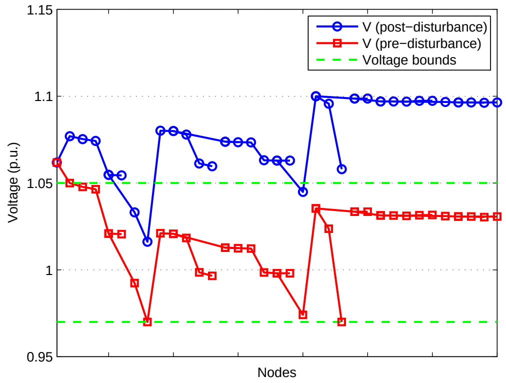

Figure 4.9: Pre- and post-disturbance voltage profile along the 34-node feeder.

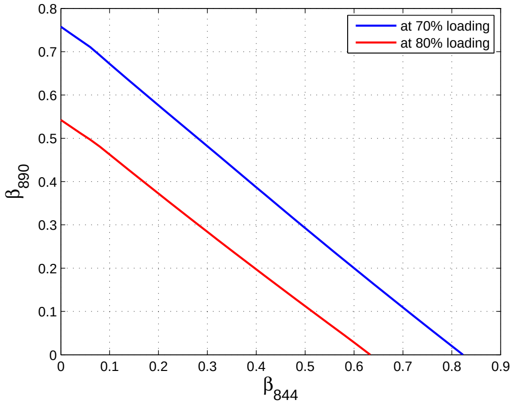

Figure 4.10: Sensitivity between $\beta_{844}$ and $\beta_{890}$ for two loading scenarios on the 34-node feeder.

#### 4.4.2.3 Maximum vulnerability

The results of the optimization (4.10)-(4.12) coupled with (4.13), for a range of loading conditions, are presented in Table 4.3. These results identify the locations where high penetration of PEV load makes the network most vulnerable to post-disturbance overvoltages. It is again clear that adding PEV charging load near the ends of the feeder maximizes vulnerability. For this particular case, the spurs associated with node 890 and with nodes 848-846-844 are most sensitive to PEV load loss. Required load drop amount at all other nodes remained zero across the selected load range, and hence were omitted from Table 4.3.

#### 4.4.2.4 Overvoltage on the three-phase model

So far the analyses have been done on the single-phase equivalent model. Figure 4.8 showed that at 100% loading, a load drop of 7.64% could result in voltage rise up to $1.1\ p.u.$. To simulate this scenario in the three-phase model, the shunt capacitor values

Table 4.3: Minimum PEV charging load necessary to cause unacceptable post-disturbance voltages on the 34-node feeder. With constraint $\beta_i \leq 0.5,\ \forall i$.

| Node $\#$ | $\%$ loading | | | | | | |
|---|---|---|---|---|---|---|---|
| | 70 | 75 | 80 | 85 | 90 | 95 | 100 |
| 844 | 0.231 | 0.113 | 0.007 | 0 | 0 | 0 | 0 |
| 846 | 0.5 | 0.5 | 0.5 | 0 | 0 | 0 | 0 |
| 848 | 0.5 | 0.5 | 0.5 | 0 | 0 | 0 | 0 |
| 890 | 0.5 | 0.5 | 0.5 | 0.456 | 0.382 | 0.319 | 0.258 |
| $\frac{\sum_i \beta_i p_i}{\sum_i p_i}$ | 0.184 | 0.135 | 0.090 | 0.061 | 0.051 | 0.043 | 0.034 |

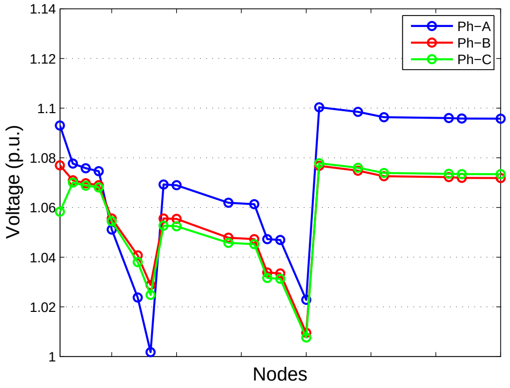

Figure 4.11: Post-fault phase voltages along the main feeder length when the load drop is uniformly 8% across three phases.

from the single-phase optimization were used alongwith adjustments in the source node voltage and regulator tap-ratios. Figure 4.11 shows the three phase-voltages along the main feeder length when a uniform PEV-induced load drop of 8% were applied across the feeder (for simplicity, the voltages on the laterals have not been shown). Post-fault voltage at phase-A of node 832 reaches $1.1\ p.u.$. However, if there is imbalance in the distribution of PEV-charging load across three phases, even a smaller load drop could potentially cause overvoltage issues. For example, Figure 4.12 shows a situation when 15% load on phase-A were dropped due to PEV-tripping but none of the base case loads were dropped on other phases. Voltage at phase-A of node 832 rises up to $1.1\ p.u.$ while other phase voltages remain nice, even though overall load drop in ths system is only about 5%.

## 4.5 Summary

It has been shown that potential overvoltage situations can be assessed using tools that are based on the power flow equations. This can be achieved by introducing variables $\beta_i$ to describe the proportion of PEV charging load at each node $i$. Three situations have been

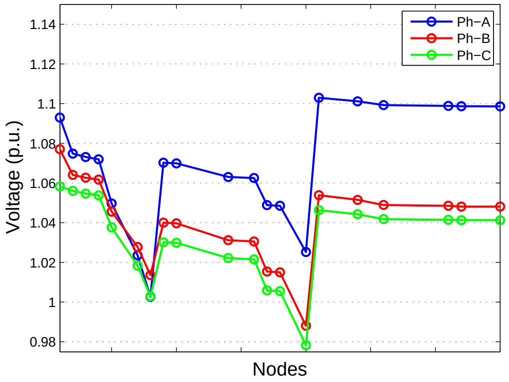

Figure 4.12: Post-fault phase voltages along the main feeder length when the load drop is concentrated at 15% on phase-A.

considered, 1) uniform distribution of PEV charging load across all loads, 2) sensitivity between various $\beta_i$, and 3) minimum charging load that can cause overvoltage issues. The outcome in each case demarcates between benign conditions where all post-disturbance voltages remain below 1.1 pu, and unacceptable situations where at least one node voltage rises above 1.1 pu.

This work has identified a potentially significant issue associated with synchronous behavior of PEV charging loads. When grid voltage sags below 80% of nominal, PEV chargers are likely to trip [76]. Voltage sags often affect entire distribution feeders, and may be even more widespread when initiated by an event on the transmission system. Study of realistic scenarios show that once the initiating event has been cleared, voltages may easily rise above 1.1 pu. This would result in further load tripping, including any remaining PEV chargers [76]. The resulting overvoltage conditions would damage electrical equipment and remaining loads.

# CHAPTER V

# Non-linear Dynamics of Hysteresis-based Control

The primary challenge in control of aggregate loads is the danger of synchronization of load response. For example, in hysteresis-based control a step change in control input can lead to large power swings (Chapters II and III), or a distant fault could lead to critical voltage rise (Chapter IV). Successful control design requires an accurate representation of the system dynamics. In the available hysteresis-based load control studies, usually some reasonable assumptions such as initial steady state, slow control input, 50% duty cycle, etc. [33, 34, 73, 94] are used to derive an analytical model, or the model is established through system identification techniques [29, 31, 32]. However a true analytical model that can capture the fast (often non-smooth) dynamics of the loads will help in designing more efficient control.

The work presented here specifically address the issue of non-linear dynamic behavior of hysteresis-based loads. While the focus of this chapter would be on PEV chargers, the analysis is applicable to other types of hysteresis-based loads, e.g. TCLs, as well. A state-space model is developed to accurately represent the system response to rather non-restrictive control input signals. The developed model is tested against a wide variety of control input, and is used to understand some interesting non-linear dynamic behaviors displayed by hysteresis-based loads.

## 5.1 Modeling

In modeling the aggregate demand response of PEV chargers, a homogeneous noise-free system would be considered. A typical charging profile is shown in Fig. 5.1 where the state-of-charge (SoC) always remains within the hysteresis deadband set up around a nominal SoC profile. While the deadband width was proportional to the maximum charge requirement ($E_{max}$) of the individual chargers, introducing a new state variable as the normalized SoC results in a normalized deadband spread symmetrically around zero [73]. The

Table 5.1: Key symbols for Chapter V

| | |
|---|---|
| $N_v$ | number of PEVs |
| $N$ | number of sections the deadband width is split in |
| $SoC$ | state-of-charge ($kWh$) |
| $\widetilde{SoC}$ | normalized state-of-charge |
| $P_{max}$ | maximum charging rate ($kW$) |
| $P_{nom}$ | nominal charging rate ($kW$) |
| $E_{max}$ | battery charge capacity ($kWh$) |
| $\Delta$ | deadband width as a fraction of battery capacity |
| $x_i(t)$ | number of chargers in $i^{th}$ bin |
| $u(t)$ | shift in normalized SoC profile over time |
| $v(t)$ | rate at which normalized SoC profile changes |

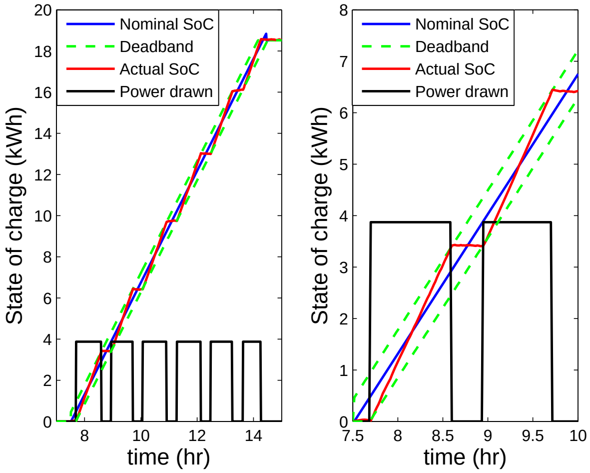

Figure 5.1: Hysteresis-based charging profile.

resulting normalized SoC ($\widetilde{SoC}$) dynamics was shown to be:

$$\dot{\widetilde{SoC}}(t) = \frac{(s(t)P_{max} - P_{nom})}{E_{max}} \tag{5.1}$$

$$\text{where,}\;\; s(t) = \begin{cases} 1, & \widetilde{SoC}(t) \leq -\Delta/2 \\ 0, & \widetilde{SoC}(t) \geq \Delta/2 \\ s(t^-), & \text{otherwise.} \end{cases}$$

and $s(t^-) = \lim_{\delta t \to 0^+} s(t - \delta t)$. With this formulation the width of the normalized deadband becomes $\Delta$. The rest of this chapter will dwell on the normalized deadband and normalized SoC, and henceforth, for simplicity, the term "normalized" will be dropped and "deadband" and "SoC" will be used to refer to "normalized deadband" and "normalized

SoC", respectively. Moreover, let two parameters, $\alpha_{on}$ and $\alpha_{off}$, be introduced as the rates of increase and decrease of (*normalized*) SoC, respectively. From (5.1) ,

$$\begin{aligned} \alpha_{on} &:= \frac{(P_{max} - P_{nom})}{E_{max}} \\ \alpha_{off} &:= -\frac{P_{nom}}{E_{max}} \end{aligned} \tag{5.2}$$

More generally, these rates $\alpha_{on}$ and $\alpha_{off}$ would be time-varying, $\alpha_{on}(t)$ and $\alpha_{off}(t)$. For example, when the nominal charging rate, $P_{nom}(t)$, is a time-varying parameter instead of a constant, $P_{nom}$, as shown in (5.1). However, in such cases, assuming that the variation is relatively small enough, average values, $\overline{\alpha}_{on}$ and $\overline{\alpha}_{off}$, could be used to account for the varying rates $\alpha_{on}(t)$ and $\alpha_{off}(t)$.

### 5.1.1 Case 1: All Chargers Inside the Deadband

The dynamics (5.1) forces all the PEV chargers to move inside the (*normalized*) deadband. Once a charger is inside the deadband, it will remain inside unless the deadband limits start moving about too quickly (it is alright if the deadband shifts slowly, as discussed in [31, 33]), or the charging completes. One approach in capturing the aggregate dynamics is to split the deadband width into N sections of equal width

$$\delta_{bin} := \Delta/\mathrm{N} \tag{5.3}$$

and notice the migration of chargers from one section to another. Considering that at any moment, some of the chargers lying within the deadband will be in ON-state while the rest in OFF-state, it is therefore useful to consider N number of bins of equal width each holding a (not necessarily equal) number of "ON" chargers and another N number of bins each holding a number of "OFF" chargers, while the number of chargers in those 2N bins determined from the probability distribution of the population's SoC. Fig. 5.2 presents a typical such scenario. The deadband is split up into N equal-width sections. The number of chargers, both in ON- and OFF-state, within those sections can be easily computed from the distribution of chargers over their SoC. Thus a bin of chargers (separately for ON- and OFF-state) is considered at each of those sections so that the height of bin represents the probability density of chargers (ON or OFF, respectively) inside that section. Bins numbered $1$ to N account for the ON-state chargers while bins numbered $\mathrm{N} + 1$ to $2\mathrm{N}$ account for the OFF-state chargers. The chargers in the ON-state are moving to the right (as their SoC increases) at a speed $\alpha_{on}$ and the OFF-state chargers are moving to the left at a rate $\alpha_{off}$. The dynamics (5.1) restricts that no ON-state charger can exist right to the boundary wall at the upper deadband limit, while no OFF-state charger may exist left to the boundary wall at the lower deadband limit. Any ON-state charger hitting the wall at the upper deadband limit instantly switches to OFF-state and any OFF-state charger upon hitting the wall at the lower deadband limit switches to ON-state.

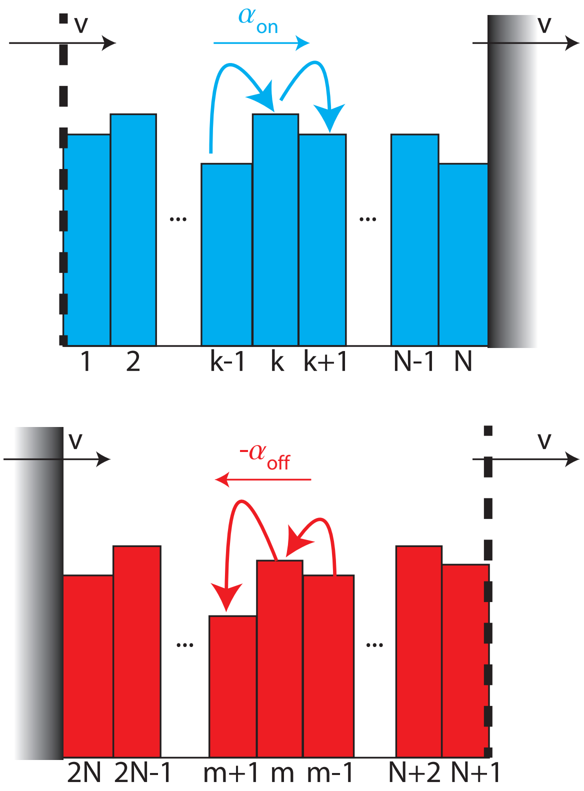

Figure 5.2: Inter-bin migration when all the loads are inside the deadband.

#### 5.1.1.1 Case 1A: Static Deadband

To start with, the deadband is assumed to be static, i.e. the deadband position (shift from nominal), $u(t)$, as well as the speed, $v(t) = \dot{u}(t)$, with which the deadband limits shift are both zero ($u(0) = 0, v(0) = 0$). Let the height of the $i^{th}$ bin, representing the probability density of chargers in that bin, at time $t$ be $x_i(t)$ $\forall i = 1, 2, 3, \ldots, 2\text{N}$. The probability that a PEV lies within the $i^{th}$ bin is then $x_i(t)\delta_{bin}$, and hence,

$$\delta_{bin} \sum_{i=1}^{2\text{N}} x_i(t) = 1.$$

Clearly the change in height $x_i(t)$ is nothing but the difference between inflow of chargers from $(i-1)^{th}$ bin and outflow of chargers from $i^{th}$ bin [33], for $i = 2, 3, \ldots, 2\text{N}$. While for $i = 1$, the inflow happens from the $2\text{N}^{th}$ bin. Taking care of the switching at the two deadband limits, the dynamics can be written as

$$\dot{x}_i(t)\delta_{bin} = \begin{cases} -x_{2\mathrm{N}}(t)\alpha_{off} - x_1(t)\alpha_{on}, & i = 1 \\ x_{i-1}(t)\alpha_{on} - x_i(t)\alpha_{on}, & i = 2, 3, \ldots, \mathrm{N} \\ x_{\mathrm{N}}(t)\alpha_{on} + x_{\mathrm{N}+1}(t)\alpha_{off}, & i = \mathrm{N}+1 \\ -x_{i-1}(t)\alpha_{off} + x_i(t)\alpha_{off}, & i = \mathrm{N}+2, \mathrm{N}+3, \ldots, 2\mathrm{N} \end{cases} \tag{5.4}$$

with the total power demand as

$$P_{tot}(t) = \mathrm{N}_v P_{max} \delta_{bin} \sum_{i=1}^{\mathrm{N}} x_i(t) \tag{5.5}$$

It is to be noted that $(\mathrm{N}+1)^{th}$ to $2\mathrm{N}^{th}$ bins correspond to OFF-state chargers and hence does not contribute to instantaneous power demand. This result holds when the deadband is static. However if the deadband starts to move, say with a rate $v(t)$, the effective rate at which the migrations take place would change. For example, if the deadband limits move with a rate $v = \alpha_{on}/2$ in the same direction as $\alpha_{on}$ (as shown in Fig. 5.2), the effective rate at which the ON-state chargers in $\mathrm{N}^{th}$ bin hit the upper limit would be $\alpha_{on}/2$ and the rate at which OFF-state chargers in $2\mathrm{N}^{th}$ bin hit the lower deadband limit would be $\alpha_{on}/2 - \alpha_{off}$.

#### 5.1.1.2 Case 1B: Slowly Moving Deadband

If the rate, $v(t)$, at which the deadband limits move is less in magnitude than the natural rates, $\alpha_{on}$ and $-\alpha_{off}$ (since $\alpha_{off} < 0$ by definition (5.2)), then the migrations would still keep taking place, but with adjusted rates as $(\alpha_{on} - v(t))$ and $(-\alpha_{off} + v(t))$ instead of $\alpha_{on}$ and $-\alpha_{off}$, respectively. Consequently, the dynamics of migration in (5.4) can be modifed to

$$\dot{x}_i(t)\delta_{bin} = \begin{cases} -\left(x_{2\mathrm{N}}(t)\left(\alpha_{off} - v(t)\right) + x_1(t)\left(\alpha_{on} - v(t)\right)\right), & i = 1 \\ \left(x_{i-1}(t) - x_i(t)\right)\left(\alpha_{on} - v(t)\right), & 2 \leq i \leq \mathrm{N} \\ \left(x_{\mathrm{N}}(t)\left(\alpha_{on} - v(t)\right) + x_{\mathrm{N}+1}(t)\left(\alpha_{off} - v(t)\right)\right), & i = \mathrm{N}+1 \\ -\left(x_{i-1}(t) - x_i(t)\right)\left(\alpha_{off} - v(t)\right), & \mathrm{N}+2 \leq i \leq 2\mathrm{N} \end{cases} \tag{5.6}$$

and total power given by the same (5.5). Existence of terms such as $x_i(t)v(t)$ in the right-hand-side of (5.6) tells that the resulting state-space model is a bilinear one [33], where states of the system are $x_i(t) \forall\, i = 1, 2, 3, \ldots, 2\mathrm{N}$.

#### 5.1.1.3 Case 1C: Fast Moving Deadband

It is expected that the state-space model would become further complicated as some different scenarios are looked into, such as a fast moving deadband. Till the rate of deadband shift is “slow”, i.e. $\alpha_{off} < v(t) < \alpha_{on}$, the chargers would keep on hitting the two boundary walls, right boundary wall for the ON-state chargers and left bundary wall for the OFF-state chargers, and as a result all of the chargers would remain inside the moving deadband. But as soon as, the rate of deadband shift becomes too high, the switching between states would cease to operate normally. For example, if the deadband is moving towards right with a speed $v(t) > \alpha_{on}$, there would be no more switching at the boundary wall at the upper deadband limit, although the OFF-state chargers would keep on hitting the wall at the lower deadband limit with a rate $(v(t) - \alpha_{off})$. Consequently, the N$^{th}$ bin will get detached from the upper deadband limit and start to lag behind it, and equivalently some of ON-state chargers would lie outside the deadband (left of the lower limit). Therefore, structurally the model in such scenario becomes equivalent to the ones covered in Sections 5.1.2.1 and 5.1.2.2.

### 5.1.2 Case 2: Some or All Chargers Lying Outside the Deadband

It is assumed that initially all the chargers were inside the deadband and as the deadband moved faster than the natural rates, $\alpha_{on}$ and $-\alpha_{off}$, some or all of the chargers fell outside the shifted deadband. Fig. 5.3 shows a typical case where the deadband has effectively moved to right, and some of the ON-state chargers now lie left of the lower deadband limit. By looking at the dynamics in (5.6), it can be observerd that, as $v(t)$ increases and approaches $\alpha_{on}$, the rate of inter-bin migration of ON state chargers, proportional to $(\alpha_{on} - v(t))$, also decreases. As $v(t)$ increases beyond $\alpha_{on}$ both the inter-bin migration in ON state, as well as ON-to-OFF state switching at the right boundary completely stops and a "gap" is created between the N$^{th}$ bin and the right boundary wall. Equivalent situation happens in OFF-state when $v(t)$ decreases beyond $\alpha_{off}$, as shown in Fig. 5.4. Assuming that initially all the chargers were inside the deadband limits, the "gap" between the extreme end bins and boundary wall can be defined as,

$$u_{\Delta}^{rel}(t) := \begin{cases} 0, & t = 0 \\ \displaystyle\int_0^t f\left(\tau, v\left(\tau\right)\right)\, \mathrm{d}\tau, & t > 0 \end{cases} \tag{5.7}$$

where the $f : (0, \infty] \times \mathbb{R} \rightarrow \mathbb{R}$ is defined as

$$f\left(\tau, v\left(\tau\right)\right) := \begin{cases} 0, & \tau \in T_0 \\ v(\tau) - \alpha_{on}, & \tau \in T_1 \\ v(\tau) - \alpha_{off}, & \tau \in T_2 \end{cases} \tag{5.8}$$

and,

$$T_0 := \left\{\tau \,\middle|\, u_{\Delta}^{rel}(\tau^-) = 0 \bigwedge v(\tau) \in (\alpha_{off}, \alpha_{on})\right\} \tag{5.9a}$$

$$T_1 := \left\{\tau \,\middle|\, \left(u_{\Delta}^{rel}(\tau^-) = 0 \bigwedge v(\tau) \geq \alpha_{on}\right) \bigvee u_{\Delta}^{rel}(\tau^-) > 0\right\} \tag{5.9b}$$

$$T_2 := \left\{\tau \,\middle|\, \left(u_{\Delta}^{rel}(\tau^-) = 0 \bigwedge v(\tau) \leq \alpha_{off}\right) \bigvee u_{\Delta}^{rel}(\tau^-) < 0\right\} \tag{5.9c}$$

with $u_{\Delta}^{rel}(\tau^{-}) = \lim\limits_{\delta\tau \to 0+} u_{\Delta}^{rel}(\tau - \delta\tau)$, and $\bigvee$ and $\bigwedge$ denote standard Boolean operators. Clearly, assuming that initially all chargers were inside the deadband limits, the variable $u_{\Delta}^{rel}(t)$ would be zero till the time $v(t)$ is less than the natural rates of chargers. As $v(t)$ becomes higher than $\alpha_{on}$, $u_{\Delta}^{rel}(t)$ would be positive and the number of bins lying outside the deadband limits would be proportional to $u_{\Delta}^{rel}(t)$. Please note that, bins will lie below the lower deadband limit when $u_{\Delta}^{rel}(t) > 0$, and above the upper deadband limit when $u_{\Delta}^{rel}(t) < 0$. Let $n_t$ be the number of bins (either ON or OFF) lying outside the deadband limits at time $t$. Then,

$$n_t := \min\left(\left\lceil \frac{\left|u_{\Delta}^{rel}(t)\right|}{\delta_{bin}} \right\rceil, \mathrm{N}\right); \tag{5.10}$$

It is to be noted that while the actual deadband position may lie within a bin, thereby making a part of that bin outside the deadband limits and the rest inside, it suffices to consider the whole of that bin outside the bin, as "ceiling" function does in (5.10), because the width of the bin is a very small fraction, $1/\mathrm{N}$, of the deadband width.

*Note:If $u(t)$ undergoes a step change, then $v(t)$ will be undefined at that instant and (5.7) is no longer applicable, because $f(\tau, v(\tau))$ becomes undefined. One way to resolve this issue is to assume that practically all step changes can be approximated by a super-fast ramp signal, and this way $v(t)$ is defined everywhere. And with that, the gap $u_{\Delta}^{rel}(t)$ can be always computed using (5.7). Because there is no limit to how large the v(t) can be, a step input canl be smoothed into a sufficiently fast ramp input. Another way of looking at it is by decomposing the shift in deadband into one component $u(t)$ that varies continuously and another component $\Delta u(t)$ that is constant apart from step changes. The continuous component $u(t)$ is used to determine v(t), and thus drives variations in $u_{\Delta}^{rel}(t)$ according to (5.7). To account for the step-wise contribution given by $\Delta u(t)$, the total variation in $u_{\Delta}^{rel}(t)$ is given by,*

$$u_{\Delta}^{rel}(t) = u_{\Delta,5.7}^{rel}(t) + \Delta u(t)$$

*where $u_{\Delta,5.7}^{rel}(t)$ refers to the value of $u_{\Delta}^{rel}(t)$ given by (5.7).*

The aim is to be able to quantify the inter-bin migration of chargers in this scenario. In Section 5.1.1 the deadband was split into N equal parts and the number of chargers, both in ON- and OFF-state, lying in those equal parts were monitored to ultimately derive the total power demand $P_{tot}(t)$. This resulted in a state-space of length 2N. When the number of chargers lying outside the deadband is under consideration, a first logical extension could be to increase the number of bins so as to cover the shift in deadband. This would require a larger number of bins and hence a larger state-space to handle. It might even cause scalability and/or computational issues if the shifts in deadband are unpredictably large, e.g. a few times the deadband width itself. However a closer inspection reveals that stretching the state-space is not be necessary, and the same 2N number of states are able to

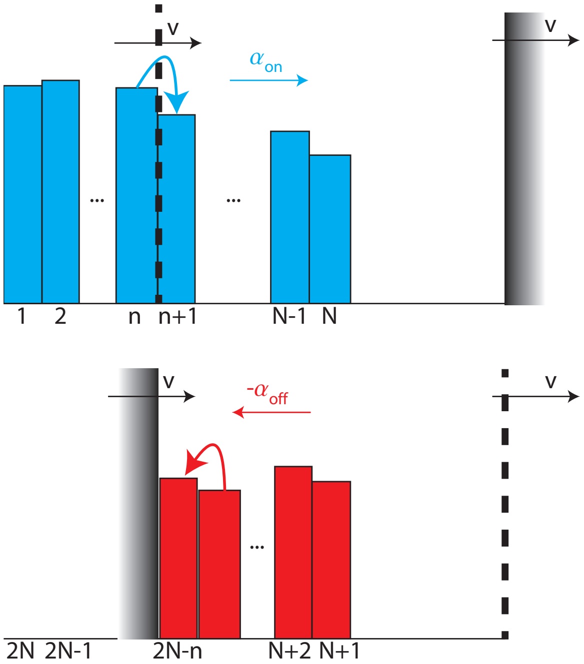

Figure 5.3: Inter-bin migration when some chargers lie left of the deadband.

capture the dynamics under situations such as Fig. 5.3.

Let us next state a result that establish mathematically that no matter what the control input is, the initial $2\mathrm{N}$ bins are sufficient in capturing the dynamics. In order to do that, let the following variables be defined:

$$\begin{aligned}
\widetilde{SoC}^{U}_{on}(t) &:= \text{Maximum SoC among all chargers in the ON-state at time } t \\
\widetilde{SoC}^{L}_{on}(t) &:= \text{Minimum SoC among all chargers in the ON-state at time } t \\
\widetilde{SoC}^{U}_{off}(t) &:= \text{Maximum SoC among all chargers in the OFF-state at time } t \\
\widetilde{SoC}^{L}_{off}(t) &:= \text{Minimum SoC among all chargers in the OFF-state at time } t \qquad (5.11)
\end{aligned}$$

**Theorem V.1.** *If there exists a time instant such that all the loads together (regardless of their state) span a width that is less than or equal to the width of the hysteresis band (not necessarily lying within the exact band limits), then for all subsequent time instants those loads will span a width that is less than or equal to the width of the hysteresis band. Mathematically,*

$$\exists\, t_0 \mid \max\left(\widetilde{SoC}^{U}_{on}(t_0), \widetilde{SoC}^{U}_{off}(t_0)\right) - \min\left(\widetilde{SoC}^{L}_{on}(t_0), \widetilde{SoC}^{L}_{off}(t_0)\right) \leq \Delta, \tag{5.12a}$$

$$\implies \forall\, t > t_0,\ \max\left(\widetilde{SoC}^{U}_{on}(t), \widetilde{SoC}^{U}_{off}(t)\right) - \min\left(\widetilde{SoC}^{L}_{on}(t), \widetilde{SoC}^{L}_{off}(t)\right) \leq \Delta. \tag{5.12b}$$

*Proof.* Please refer to Appendix D for the proof. ☐

Theorem V.1 shows that it is indeed possible to quantify the aggregate power dynamics by simply considering the state-space of 2N number of bins spanning a width, $\Delta$, equal to that of the deadband. Next two sections discuss how this can be achieved.

#### 5.1.2.1 Case 2A: Chargers Lying Left to the Lower Limit ($u_{\Delta}^{rel}(t) > 0$)

Let us consider the case when some (or all) of the chargers are lying to the left of the lower deadband limit. There is a gap between the right-most ON state charger and the upper deadband limit, as illustrated in Fig. 5.3. Thus there will be no hitting at the right boundary wall and hence no switching from ON-to-OFF state. Consequently all the ON state bins would move towards right with the same natural rate, $\alpha_{on}$ and there would be no inter-bin migration in the ON state. However there would be continued switching from OFF-to-ON state at the left boundary wall thereby increasing the height of the ON-state bin SoC of which coincides with the lower deadband limit.

When all the chargers were inside the deadband limits (Section 5.1.1) the positions of the bins were easily referenced with the help of the deadband. Even though the deadband moved with $v(t) \in (\alpha_{off}, \alpha_{on})$, the bins' position relative to the deadband remained fixed. In the case when chargers lie left to the lower deadband limit, it would be helpful to choose the positions of the ON-state bins as reference. That is, for the sake of analysis, an equivalent situation is considered where the ON state bins remain fixed and the deadband moves with relative rate $(v(t) - \alpha_{on})$, and the OFF state chargers change their SoC at a relative rate of $(\alpha_{off} - \alpha_{on})$. Due to absence of any boundary switching from ON-to-OFF state, the height of the $(N+1)^{th}$ bin in the OFF-state would simply decrease with rate proportional to $(\alpha_{on} - \alpha_{off})x_{N+1}(t)$, and the rate of OFF-to-ON state switching is proportional to $x_{2\mathrm{N}-n_t}(t)\ \max(0,\ v(t) - \alpha_{off})$, where $n_t$ is given by (5.10). It is to be noted that if $v(t) < \alpha_{off}$ there can be no OFF-to-ON switching. The state dynamics of the bins is then given by:

$$\dot{x}_i(t)\delta_{bin} = \begin{cases} x_{2\mathrm{N}-n_t}(t)\max\left(0,\ v\left(t\right) - \alpha_{off}\right), & i = n_t + 1 \\ x_i(t)\left(\alpha_{off} - \alpha_{on}\right), & i = \mathrm{N}+1 \\ -(x_{i-1}(t) - x_i(t))\left(\alpha_{off} - \alpha_{on}\right), & i = \mathrm{N}+2, \mathrm{N}+3, \\ & \quad \ldots, 2\mathrm{N} - n_t - 1 \\ \begin{array}{l} -x_i(t)\max\left(0,\ v\left(t\right) - \alpha_{off}\right) \\ \quad -x_{i-1}(t)\left(\alpha_{off} - \alpha_{on}\right) \end{array}, & i = 2\mathrm{N} - n_t \\ 0, & \text{all other } i \end{cases} \tag{5.13}$$

#### 5.1.2.2 Case 2B: Chargers Lying Right to the Upper Limit ($u_{\Delta}^{rel}(t) < 0$)

When some or all of the chargers lie to the right of the upper deadband limit, as illustrated in Fig. 5.4, similar formulation as in Section 5.1.2.1 can be excercised by considering

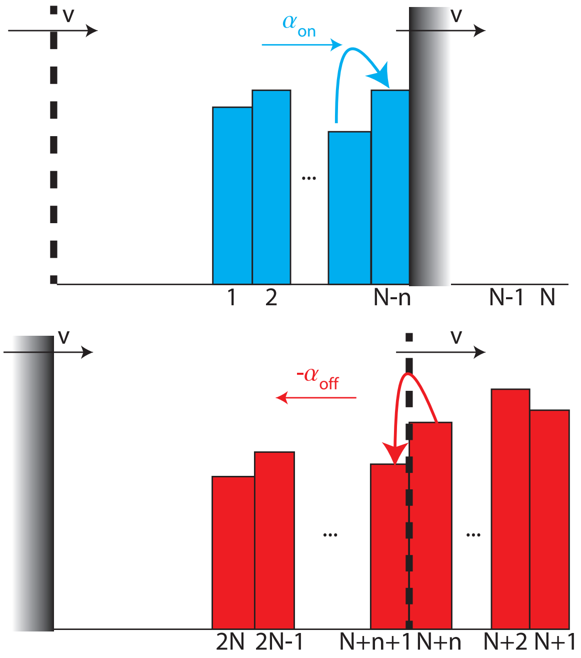

Figure 5.4: Inter-bin migration when some chargers lie right of the deadband.

the position of the OFF-state bins as reference. In this frame of reference, the OFF state chargers stand still resulting in no inter-“OFF bin” migration, while ON state chargers change SoC at rate $(\alpha_{on} - \alpha_{off})$, and the ON-to-OFF switching at the right boundary is proportional to $x_{\mathrm{N}-n_t}(t)\max\left(0, \left(\alpha_{on} - v\left(t\right)\right)\right)$, where $n_t$ is the number of OFF-state bins lying right of the upper deadband limit at time $t$, given by (5.10). The state equations become:

$$\dot{x}_i(t)\delta_{bin} = \begin{cases} -x_i(t)\left(\alpha_{on}-\alpha_{off}\right), & i=1\\ \left(x_{i-1}(t)-x_i(t)\right)\left(\alpha_{on}-\alpha_{off}\right), & i=2,3,\ldots,\mathrm{N}-n_t-1 \\ \begin{array}{l}-x_i(t)\max\left(0,\ \alpha_{on}-v\left(t\right)\right)\\ \quad +x_{i-1}(t)\left(\alpha_{on}-\alpha_{off}\right)\end{array}, & i=\mathrm{N}-n_t \\ x_{\mathrm{N}-n_t}(t)\max\left(0,\ \alpha_{on}-v\left(t\right)\right), & i=\mathrm{N}+n_t+1\\ 0, & \text{all other } i\end{cases} \tag{5.14a}$$

State equations in (5.6), (5.13) and (5.14) together represent the complete aggregate power model, where aggregate power is given by (5.5). To summarize, Table 5.2 shows how each of these state equations applies to different scenarios of control input and the hysteresis band positions.

Table 5.2: Aggregate non-linear model of hysteresis-based loads.

| $u_{\Delta}^{rel}(t)$<br>$v(t)$ | $< 0$ | $= 0$ | $> 0$ |
|---|---|---|---|
| $> \alpha_{on}$ | (5.14) | (5.13) | (5.13) |
| $\in [\alpha_{off}, \alpha_{on}]$ | (5.14) | (5.6) | (5.13) |
| $< \alpha_{off}$ | (5.14) | (5.14) | (5.13) |

## 5.2 Numerical Verification

The model built in Section 5.1 is verified against Monté-Carlo simulation of a homogeneous population of PEV chargers[1] each following the dynamics in (5.1). Fig. 5.5 illustrates a situation when the deadband moves slowly so that all the chargers stay within the deadband limits. The deadband is set to a sinusoidal oscillation (Fig. 5.5(a)) so that the rate of movement stays inside $(\alpha_{off}, \alpha_{on})$, as shown in Fig. 5.5(c). Since the deadband keeps moving at enough slow rate, the chargers always remain inside the deadband limits as supported by the fact that $u_{\Delta}^{rel}(t)$ stays at zero throughout (Fig. 5.5(a)). The resulting aggregate power demand is shown in Fig. 5.5(b) which verifies that the model output matches the Monté-Carlo simulation output. The case of fast movement of the deadband, resulting in chargers lying outside the deadband, is treated in Fig. 5.2. As the deadband position $u(t)$ moves faster than the natural rates, as shown in Fig. 5.6(c), some chargers start to fall outside the deadband limits as supported by the non-zero values of $u_{\Delta}^{rel}(t)$ in Fig. 5.6(a). Just as $v(t)$ increases beyond $\alpha_{on}$, the relative "gap" between the bins and the deadband $u_{\Delta}^{rel}(t)$ becomes positive and stays so until such a time $v(t)$ has dropped below $\alpha_{on}$ and the bins slowly catch up and get inside the deadband limits. The aggregate demand shows large oscillation which fluctuate between the maximum and zero (Fig. 5.6(b)). In Fig. 5.2, this effect of fast forced fluctuation is created by high frequency pulsating movement of the deadband (Fig. 5.7(a)) followed by a very slow sinusoidal oscillation. Fig. 5.7(b) shows that even after the deadband movement slows down, the total power keeps oscillating between maximum and zero but with a reduced frequency. Thus an exposure to high frequency, and relatively large, movements in the deadband position can render the system almost unresponsive to small and slow changes in the deadband position.

## 5.3 Nonlinear Dynamic Behavior

Hysteresis-based control mechanism introduces switching-induced nonlinearity in the system. Particularly interesting is the response of the system to control input signals that periodically ramp up and down.

---

[1] Parameters for the simulation are (Table 5.1): $\mathrm{N}_v = 1000$, $\mathrm{N} = 200$, $\Delta = 0.05$, $P_{max} = 4$ kW, $P_{nom} = 2.4$ kW, $E_{max} = 16$ kW-hr. The continuous dynamics in (5.1) was discretized using a time step of 0.2 min.

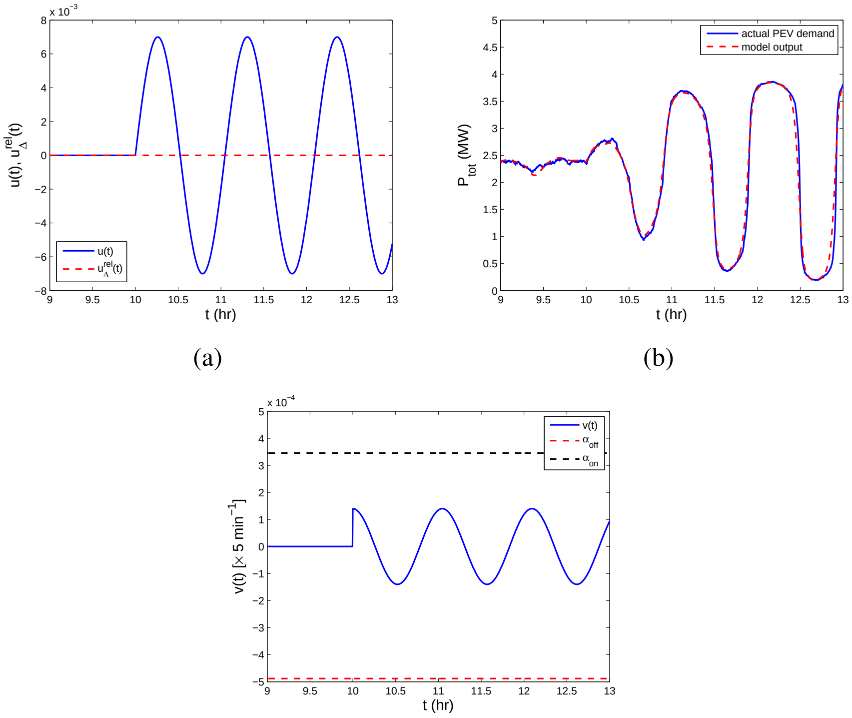

(a) (b)

(c)

Figure 5.5: System response when the deadband moves slowly and all the chargers are always within the deadband.

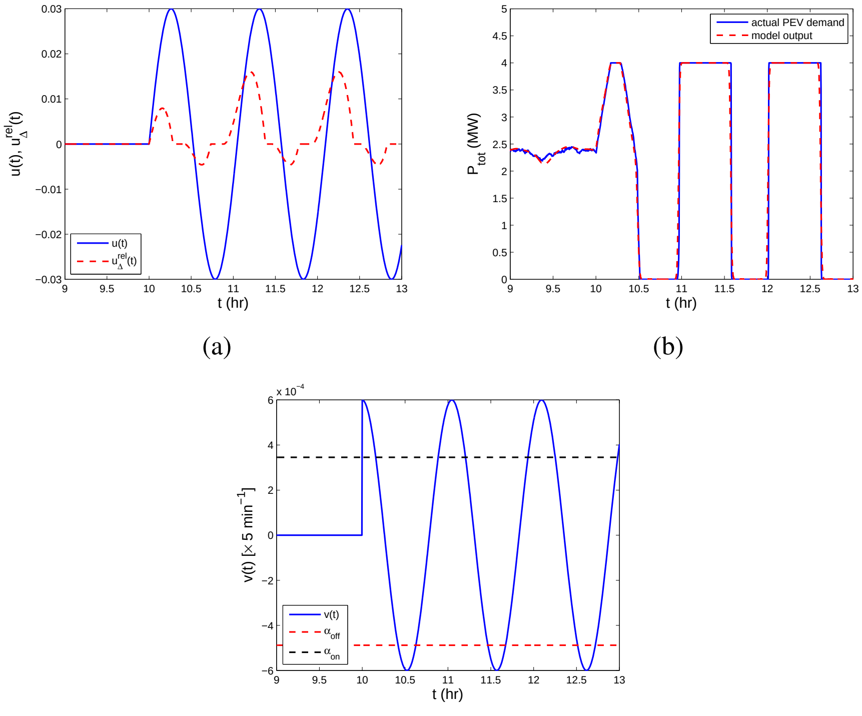

(a) (b)

(c)

Figure 5.6: System response when the deadband moves rapidly and some of the chargers fall outside the deadband.

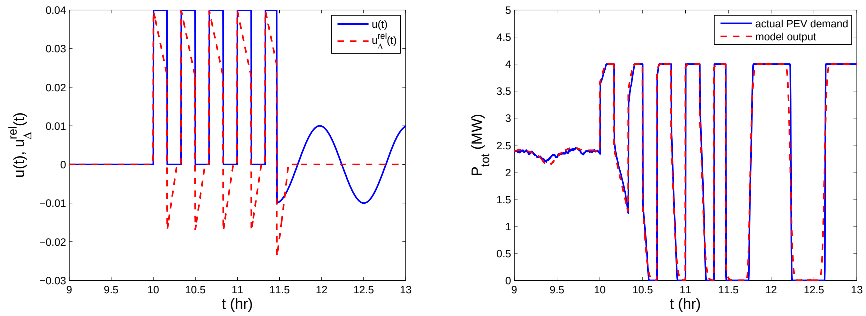

(a) (b)

Figure 5.7: Exposure to frequent deadband movement renders the system less responsive to slowly variations.

### 5.3.1 Response to Slow Ramps

Fig. 5.8(a) shows such an input which ramps up and down periodically. Each ramp up and ramp down sequence is of duration 15.4 min each and ramp rates less than ‘natural’ (Fig. 5.8(b)). Please note that the since the input varies at a slower than “natural” rate, the chargers always stay within the hysteresis band which is why $u_{\Delta}^{rel}(t)$ remains zero throughout. The resulting demand response is a period-1 waveform which keeps on oscillating closely between the maximum and zero (Fig. 5.8(c)). However interesting phenomena start

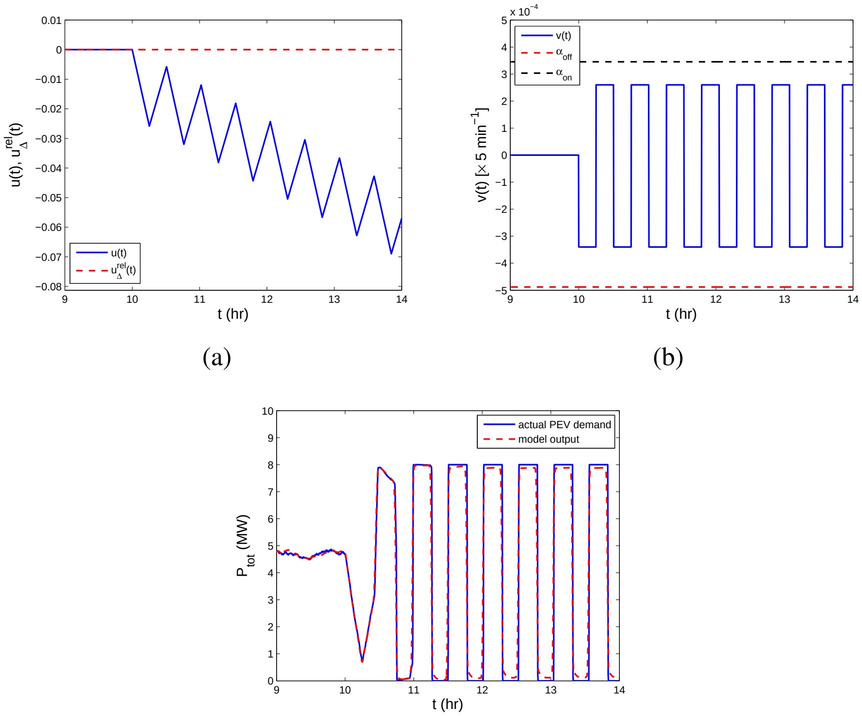

(a)

(b)

(c)

Figure 5.8: Period-1 response to a input of equally wide ramp up and down sequences with rates 0.0013 min$^{-1}$ and 0.0017 min$^{-1}$, respectively, and having a time period 30.8 min.

to happen as the time period of the control input is gradually decreased. Fig. 5.9 show one such scenario when the total time period of the input is reduced to 24.4 min while keeping the ramp rates unchanged. Aggregate demand, shown in Fig. 5.9(c), enters into a period-2 orbit, i.e. having a time period twice that of the input, with a reduction in amplitude as well. The Monté-Carlo simulation results are compared against the state-space model output by simulating (5.6), in Fig. 5.8(c) and Fig. 5.9(c).

To investigate this further, a bifucation diagram was plotted using a Monté Carlo simulation of individual dynamics in (5.1). Keeping other parameters fixed, the time period of the input, $T_u$, was varied over a wide range, and the intersections of the output with a

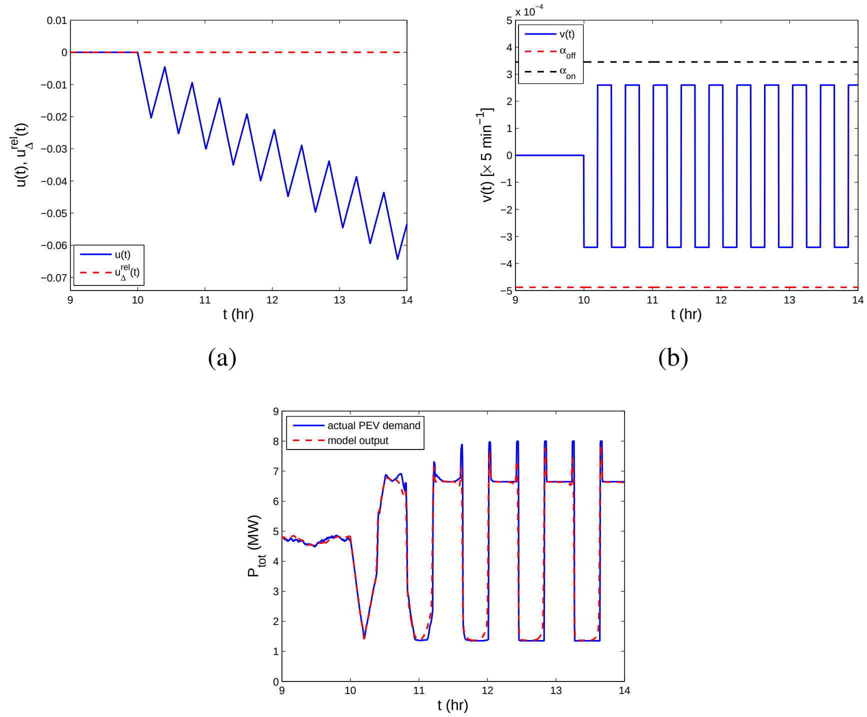

(a)

(b)

(c)

Figure 5.9: Period-2 response to a input of equally wide ramp up and down sequences with rates 0.0013 $\text{min}^{-1}$ and 0.0017 $\text{min}^{-1}$, respectively, and having a time period 24.4 min.

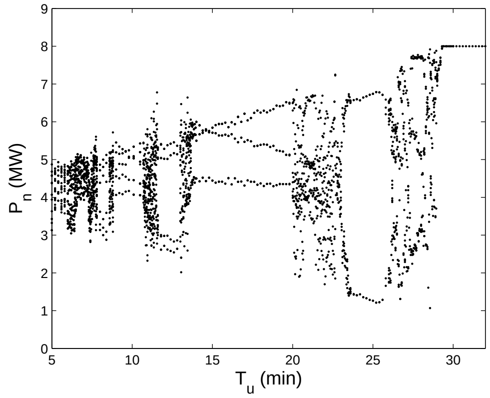

Figure 5.10: Bifurcation diagram when the input is a periodic ramp, with ramp up and down rates as 0.0013 $\text{min}^{-1}$ and as 0.0017 $\text{min}^{-1}$, respectively.

Poincaré plane, denoted by

$$P_n := P_{tot}\left(nT_u\right),\ n \in \mathbb{N}, \tag{5.15}$$

were plotted after discarding the transients, $n > n_0$ (a $n_0 = 5$ was found to be sufficient). The resulting bifurcation diagram is shown in Fig. 5.10. For time period, $T_u$, values over $\sim$30 min, the demand follows a period-1 orbit. Periodicity collapses as $T_u$ is reduced, until a period-2 orbit appears at $\sim$26 min, which again collapses as $T_u$ is reduced to $\sim$23 min. As $T_u$ keep on decreasing, such a sequence of period-adding cascade is observed with successive periodic regions interspersed by regions of aperiodicity. By carefully selecting the value of the parameter $T_u$, different higher periodic orbits can be generated in the system response. Figs. 5.11(a) & 5.11(b) respresent two such scenarios, at $T_u$ values of 15.6 min and 12.4 min, when, respectively, a period-3 and a period-4 orbit exist. It is to be noted that ramp rates are kept fixed at their previous values, ramp up rate at 0.0013 min$^{-1}$ and ramp down rate at 0.0017 min$^{-1}$, for all these figures.

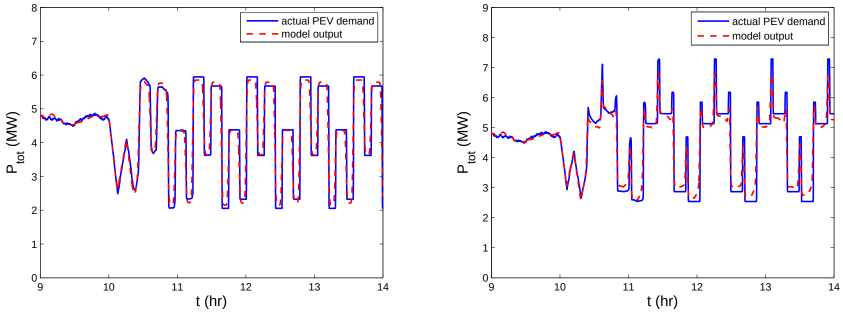

(a) At $T_u = 15.6$ min (b) At $T_u = 12.4$ min

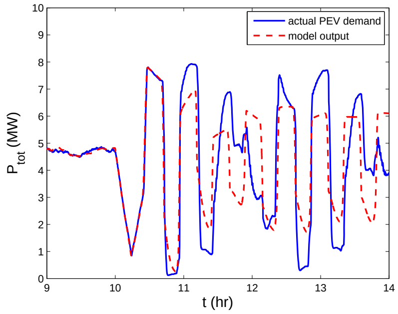

(c) At $T_u = 28.8$ min

Figure 5.11: Demand response at different $T_u$ values, with the ramp up and down rates fixed at 0.0013 min$^{-1}$ and as 0.0017 min$^{-1}$, respectively.

So far the model developed in Section 5.1 truly captured the complex response of the system. However, model accuracy reduces drastically as time period is chosen from within one of the aperiodic regions. Fig. 5.11(c) shows a typical such waveform when the input time period is chosen to be 28.8 min. In this case, the model output and the Monté-Carlo simulation start off pretty close to each other but soon, after about one of input cycle, deviate from each other by a significant large margin. This behavior is similar to what is observed in a chaotic orbit, where a small error in initial condition can quickly grow out of bounds. However, finding out exact nature of the time waveform in Fig. 5.11(c) requires further analysis and is beyond the scope of the present work.

### 5.3.2 Faster Ramp Rates

It appears that this nonlinear dynamic behavior is rather non-restrictive to any particular ramp rate. However, the exact nature of the nonlinear response varies as the ramp rates change. To investigate this, the nonlinear behavior of the demand response was studied under ramp rates that are faster than the natural rates, while comparing the Monté-Carlo simulation with the state-space equations in Section 5.1.

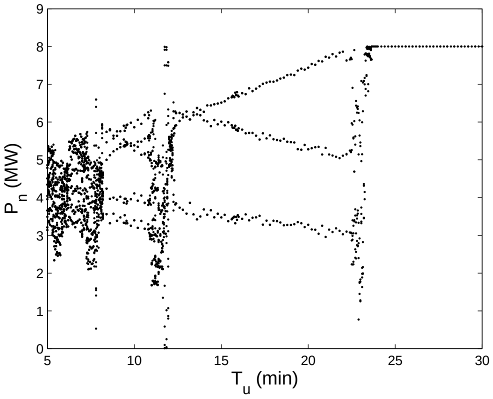

Figure 5.12: Bifurcation diagram when the input is a periodic ramp, with ramp up and down rates as 0.002 $\text{min}^{-1}$ and as 0.0028 $\text{min}^{-1}$, respectively.

Fig. 5.12 shows a bifurcation diagram when the ramp rates were chosen from beyond the natural rates, $\alpha_{on}$ and $\alpha_{off}$. It is found that the range of stability of period-1 orbit extends down to $T_u$ ≈24 min. Moreover the earlier observed (Fig. 5.10) period-2 orbit disappers. A period-3 orbit closely follows the period-1 orbit after narrow band of aperiodicity as $T_u$ is decreased. Subsequently a period-5 orbit exists followed by another band of aperiodcity, while no discernible existence of period-4 is observed. Fig. 5.13 confirms the existence of period-1 orbit at $T_u$ =24.4 min. Because the ramp rates are higher (in magnitude) than the natural rates (Fig. 5.13(b)), some chargers fall out of the hysteresis band as reflected in non-zero values of $u_{\Delta}^{rel}(t)$, as in Fig. 5.13(a). It might seem to the naked eye that very narrow bands of period-2 and period-4 orbit are present at $T_u$ values ∼13 min and ∼9.5 min, respectively. However, time waveforms in Fig. 5.14(c) and Fig. 5.14(a) reveal that it is not the case, while Fig. 5.14(b) shows the presence of an aperiodic region between the stable period-3 and period-5 regions.

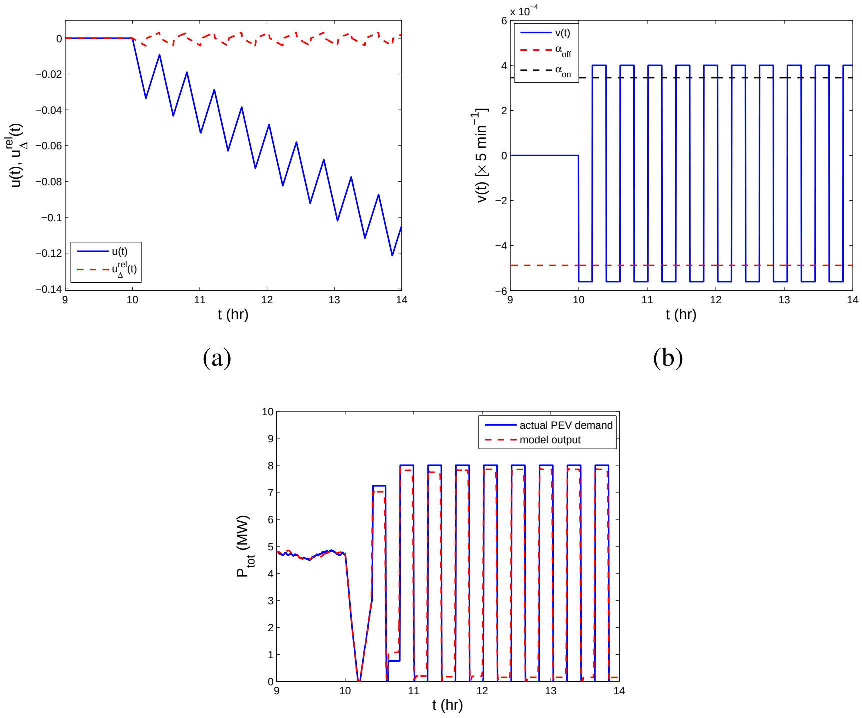

(a)

(b)

(c)

Figure 5.13: Period-1 response when input time period, $T_u$, is 24.4 min, and ramp up and down rates are 0.002 $\min^{-1}$ and as 0.0028 $\min^{-1}$, respectively.

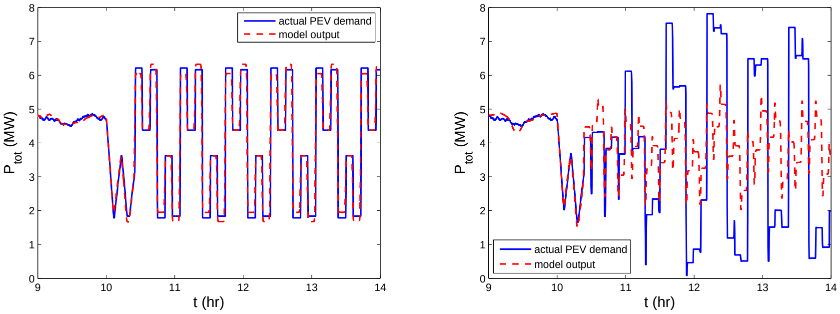

(a) At $T_u$ =13.2 min (b) At $T_u$ =11.93 min

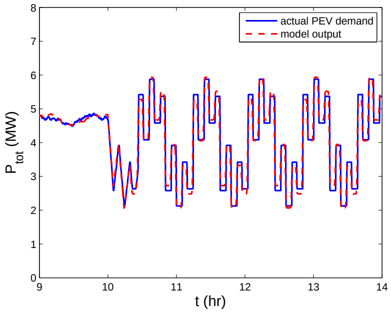

(c) At $T_u$ =9.6 min

Figure 5.14: Demand response at different $T_u$ values, with the ramp up and down rates fixed at 0.002 $\text{min}^{-1}$ and as 0.0028 $\text{min}^{-1}$, respectively.

The two important observations of the bifurcation analysis of faster ramp rates in Fig. 5.12 are that the period-1 orbit is stable for a larger parameter region and period-2 and period-4 orbits appear to be absent (or almost indiscernible). In priliminary analysis, these two findings seem to be quite general for all ramp input faster than natural rates. Fig. 5.15 illustrates this where a bifurcation diagram is plotted for ramp up and down rates 0.003 min$^{-1}$ and 0.004 min$^{-1}$, respectively. Period-1 orbit now extends down to $T_u = 20$ min, narrowly followed by a period-3 orbit, while the period-2 and period-4 orbits disappear.

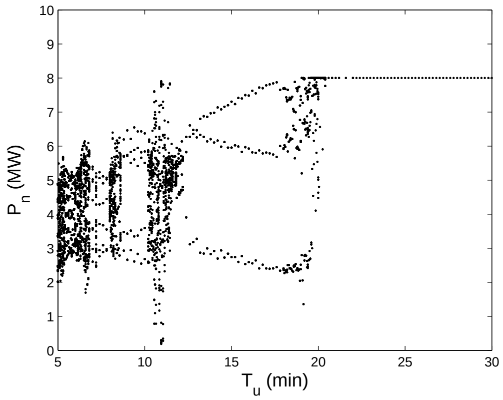

Figure 5.15: Bifurcation diagram when the input is a periodic ramp, with ramp up and down rates as 0.003 min$^{-1}$ and as 0.004 min$^{-1}$, respectively.

## 5.4 Summary

In this chapter, a hysteresis based charging process for PEVs is considered and detailed nonlinear state-space model is built to capture the aggregate population dynamics of a large number of PEV chargers in response to deadband movement. The model is shown to be able to truly replicate the dynamics even in the range of very large fluctuations in the deadband position. It also provides tool to understand the system behavior such as a frequent strong fluctuation in deadband position rendering the system unresponsive to following slow fluctuations typically generated from some control actions. The choice of PEV chargers as population is non-restrictive and similar modeling approach could be applied to other hysteresis-based processes, e.g. thermostatically-controlled-loads. The model developed is able to truly capture the rich dynamical behavior of hysteresis-based loads. It has been observed that stability of the system can be disrupted by changing a certain parameters of the control signal. Bifurcation diagrams are obtained by varying the time period of a periodic ramp input. When the ramp rates are kept to slower than the natural rates, a period adding cascade is observed. Stability region of the period-1 orbit is found to increase when the ramp rates are faster than natural. With a better understanding of the dynamics of the system, it would be easier to design effective demand control algorithms and ensure stable operations of the grid. However a lot of study is required to fully understand the dynamics. It would be interesting to obtain quantitative relations between the stability of the response and the control input parameters.

# CHAPTER VI

# Distributed Control of Reactive Power

Much like the way "deferrable' ' electrical loads offer increased control of grid operations, distributed generation units spread across power grid offer additional resources to the grid. Not only they provide support to the conventional power generation, these are also capable of extending reactive power support, to improve voltage profiles, minimize line losses. However one of the main differences between an electrical load and distributed generation is that distributed generation is heavily reliant upon weather conditions (uncontrollable by a central co-ordinator). Thus designing a centralized control for distributed generation is impractical! However while the standard optimizaiton proceedures can ensure optimality of a centralized control scheme, it is rather unclear how to provide such guarantee in a distributed control set-up.

The goal of this ongoing work presented in this chapter is to design a decentralized algorithm that regulates the reactive power output from highly distributed photovoltaic (PV) sources. A PV panel produces direct-current power, with production dependent upon the available solar irradiance. An inverter converts the DC power into alternating-current for supply to the grid. The rapid variations in net power flow can result in extensive voltage swings across the grid [59–62]. However PV inverters are capable of providing flexible reactive power support to the grid. The approach adopted here is to study solutions of a global optimization routine run under varied operating conditions, by simulating varying loading and weather scenarios, and then analytically derive a control law that performs (near-)optimally while taking only local measurements (such as voltage, power consumption, and/or local line flow). First part of this chapter presents how a completely local control law can be derived in a simplistic set up, while the later part of the chapter focuses on the modifications required to the control law to be applicable in a more realistic scenario.

## 6.1 Model Description

### 6.1.1 PV inverters without storage

The active and reactive power generated by an inverter attached to the $j$-th PV source will be denoted by $p_j^g$ and $q_j^g$, respectively. Without local storage, a PV inverter does not

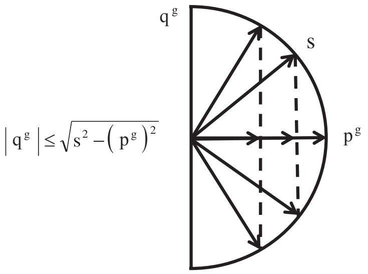

Figure 6.1: Dependence of PV inverter reactive power capability $q^g$ on active power generation $p^g$.

control $p_j^g$, but it can control $q_j^g$ to be either positive or negative. This reactive power capability is limited by the inverter's fixed apparent power capability $s_j$ and its variable active power generation $p_j^g$, and is given by [68, 95],

$$|q_j^g| \leq \sqrt{s_j^2 - (p_j^g)^2} := q_{j,max}^g. \tag{6.1}$$

This relationship is illustrated by the complex power diagram in Fig. 6.1. In [68], it was found that $s_j \approx 1.1 p_{max}^g$ provides sufficient freedom in $q_j^g$ to realize a substantial reduction in distribution losses. Under this condition, $|q_j^g| \leq 0.45 p_{max}^g$ when $p_j^g = p_{max}^g$. The choice of $s_j \approx 1.1 p_{max}^g$ is reasonable because inverters are available in discrete sizes and are likely to be slightly oversized relative to $p_{max}^g$. For the first part of this chapter, it will be assumed that the inverters at each node are identical and,

$$p_{j,max}^g = 2\,\text{kW}, \quad s_j = 2.2\,\text{kVA}, \quad \forall j. \tag{6.2}$$

This assumption will be relaxed later on.

### 6.1.2 Grid model

Initial part of this chapter would consider a simplistic grid model which is represented by a radial distribution feeder with no laterals, as shown in Fig. 6.2. The first node, at the substation, will be denoted as node $0$. Node number increases as the feeder is traversed away from the substation. The resistance and reactance between nodes $i$ and $i+1$ are given by $r_i$ and $x_i$, while $P_i$ and $Q_i$ denote the active and reactive power flowing from node $i$ towards node $i+1$. The active and reactive power consumed at node $i$ is given by $p_i^c$ and $q_i^c$, and the active and reactive power generated by a PV source at node $i$ is given by $p_i^g$ and $q_i^g$.

Consider a distribution feeder with $N+1$ nodes (in the following example, $N = 100$ is assumed), and with a PV source at each node. The feeder model can be written using the

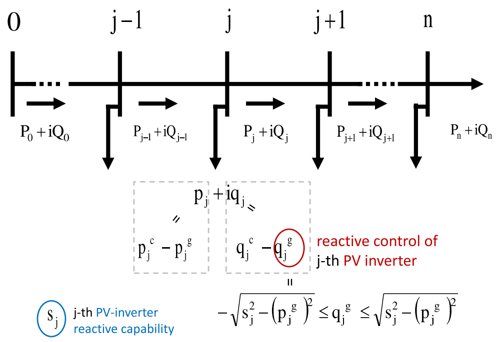

Figure 6.2: Distribution feeder with no laterals.

LinDistFlow form [85, 90, 96], where for each $i \in \{1, 2, ..., N\}$,

$$P_{i-1} = \sum_{j=i}^{N} p_j = \sum_{j=i}^{N} \left(p_j^c - p_j^g\right) \tag{6.3a}$$

$$Q_{i-1} = \sum_{j=i}^{N} q_j = \sum_{j=i}^{N} \left(q_j^c - q_j^g\right) \tag{6.3b}$$

$$V_i = V_0 - \sum_{j=0}^{i-1} \left(r_j P_j + x_j Q_j\right). \tag{6.3c}$$

This set of equations provides a simplified and approximate load flow computation. Assuming small line losses, the equations are quite accurate and provide appealing optimization properties. However, later in this chapter, a more accurate set of load flow equations would be considered.

### 6.1.3 Generating scenarios

Five levels of loading (L1-L5) will be considered, with the active load at each node $p_j^c$ drawn from a uniform distribution that has mean and width,

L1: 0.625 kW and 1.25 kW,

L2: 0.9375 kW and 1.875 kW,

L3: 1.25 kW and 2.5 kW,

L4: 1.5625 kW and 3.125 kW,

L5: 1.875 kW and 3.75 kW.

In each of these scenarios, the reactive load at each node $q_j^c$ is drawn from a uniform distribution with mean value of $0.25p_j^c$ and a width of $0.1p_j^c$. For each of the five loadings, three different solar irradiance conditions are considered,

A. *Sunny*: all PV systems are generating at $p_j^g = p_{j,max}^g$.

B. *Night time*: all PV systems generate $p_j^g = 0$.

C. *Partly cloudy*: the PV system at the first node away from the substation (i.e. at node 1) is assigned either $p_j^g = 0.2p_{j,max}^g$ or $p_j^g = p_{j,max}^g$ with equal probability, and each subsequent node is assigned,

$$p_{j+1}^g = \begin{cases} p_j^g, & \text{with probability 0.9} \\ p_{j+1,max}^g \left(1.2 - \frac{p_j^g}{p_{j,max}^g}\right), & \text{with probability 0.1.} \end{cases} \tag{6.4}$$

For each combination of loading and solar irradiance, twenty realizations were considered by randomly generating $p_j^g$, $q_j^g$, $p_j^c$, $q_j^c$. The line parameters $r_j$ were drawn from a uniform distribution with range $0.66\ \Omega$ to $0.99\ \Omega$, and $x_j = 1.15r_j$.

## 6.2 Central Optimization

For all $j \in \{0, 1, \ldots, N\}$ define,

$$\Delta V_j := V_j - 1 \tag{6.5a}$$

$$\Delta V_j^{eff} := \begin{cases} 0, & |\Delta V_j| \leq V_{sl} \\ \Delta V_j - V_{sl}, & \Delta V_j > V_{sl} \\ \Delta V_j + V_{sl}, & \Delta V_j < -V_{sl} \end{cases} \tag{6.5b}$$

where $V_{sl}$ is a soft limit for the voltage deviations from 1.0 pu. The desired control objective is expressed though the following minimization,

$$\begin{aligned} \min_{q_j^g, V_0} \mathcal{M}\left(q_{j\geq 1}^g; V_0\right) &= \sum_{j=1}^{N} \beta_j \left(\Delta V_j^{eff}\right)^2 + \sum_{j=0}^{N-1} r_j (P_j^2 + Q_j^2) \\ \text{s.t.,}\quad |V_j| &\leq 1.05, \quad \forall\, j \geq 0 \\ |q_j^g| &\leq \sqrt{s_j^2 - \left(p_j^g\right)^2}, \quad \forall\, j \geq 1. \end{aligned} \tag{6.6}$$

where $\beta_j > 0, \forall j \in \{1, 2, \ldots, N\}$ are weighing parameters associated with voltage deviations. In most distribution systems, the maximum allowable deviation of the voltage $V_j$ from 1.0 pu is 0.05. For subsequent investigations, the soft limit will be set to $V_{sl} = 0.02$. This allows the optimal control the latitude to minimize losses when the voltages $V_j$ are well within normal bounds, while smoothing the control action as the voltages begin to significantly deviate from 1.0 pu. It is also assumed that the substation voltage $V_0$ can be adjusted.

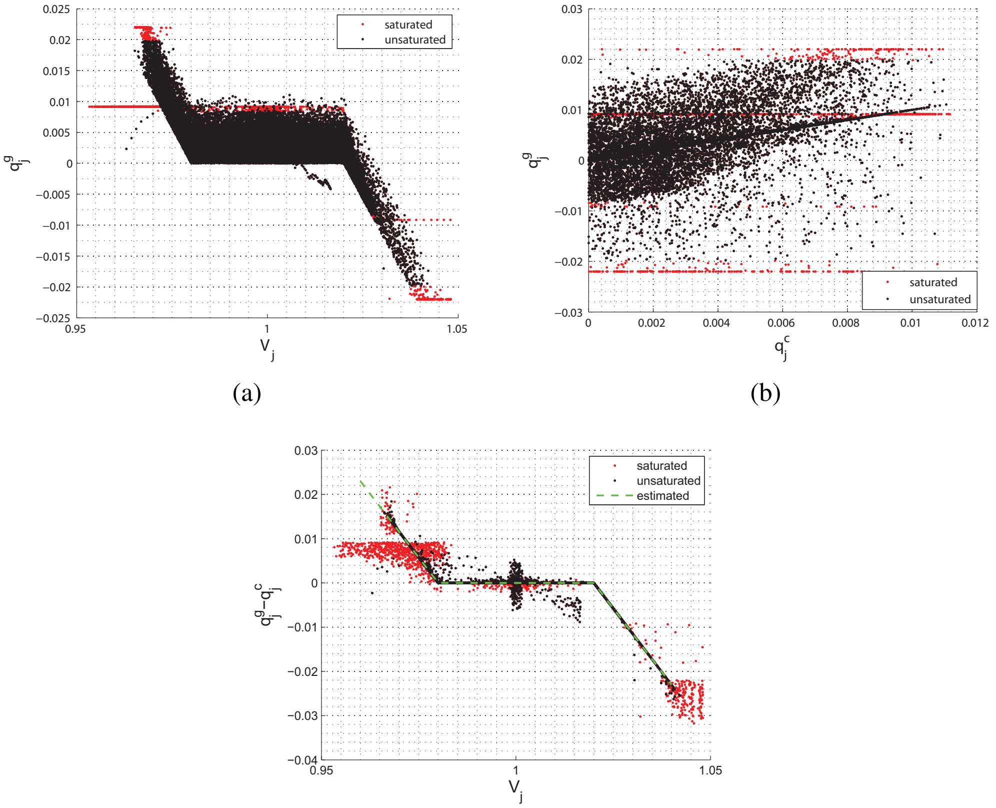

(a) (b)

(c)

Figure 6.3: Correlations between the local observables $V_j$ and $q_j^c$ and the optimal reactive dispatch $q_j^g$.

The central optimization (6.6) was evaluated, using $\beta_j = 1 \; \forall j \in \{1, 2, \ldots, N\}$, for 20 instances of each of the 15 cases discussed in Section 6.1.3. The goal was to identify any correlation between the optimal $q_j^g$ values and the locally observable (to the PV-node) quantities $V_j$, $p_j^c$, $p_j^g$, and $q_j^c$. Notice though that the load flow equations in (6.3) suggest that the $q_j^g$ values are directly linked with the reactive power flow in the system, which directly affects the voltage profile on the feeder. Thus a strong correlation is expected between $q_j^g$ and the locally observable variables $q_j^c$ and $V_j$.

Figs. 6.3(a)-6.3(b) show that some correlations exist between $q_j^g$ and the local variables $V_j$ and $q_j^c$. Red dots correspond to the $q_j^g$ that encounter their limit defined in (6.1) while black dots show those $q_j^g$ that are within their limit. Careful investigation reveals that $q_j^g$ is generally affine with $q_j^c$, with a slope that is approximately 1. Also $q_j^g$ increases or decreases linearly as $V_j$ deviates from its nominal value of 1 pu by more than $V_{sl} = 0.2$ pu. It remains fairly independent of any voltage deviations that are within the soft bounds.

## 6.3 Local Control Strategy

The imperfect correlations in Fig. 6.3 suggest that $q_j^g$ is often set to $q_j^c$ when the voltage deviations $(V_j - 1)$ are within soft limits, while responding linearly to voltage deviations beyond soft limits, $|V_j - 1| - V_{sl}$. This apparent strong correlation between the optimal $q_j^g$ and the locally observable $q_j^c$ and $V_j$ motivates a local control law of the form,

$$q_j^g = q_j^c - \alpha \Delta V_j^{eff}, \quad \forall\, j \geq 1 \tag{6.7}$$

where $\alpha$ is a design parameter chosen to optimize $q_j^g$. In fact it can be shown that if the ratio of line reactance and line resistance is constant over the entire feeder (and all $\beta_j$'s are equal to 1), the control law in (6.7) is optimal with $\alpha = x_j/r_j$. Fig. 6.3(c) illustrates the correlation between $q_j^g - q_j^c$ and $V_j$. Setting $\alpha$ to $x_j/r_j = 1.15$, which follows from the line parameter choice in Section 6.1.3, the suggested control law (6.7) closely replicates this observed correlation.

**Theorem VI.1.** *(Optimality of the local control law):*
*If all line impedances satisfy,*

$$\frac{x_j}{r_j} \triangleq \alpha, \quad \forall j \in \{0, 1, 2, \ldots, N-1\}, \tag{6.8}$$

*where $\alpha$ is a constant, then the optimal $q_j^g$ values that minimize the objective function $\mathcal{M}$ in (6.6) can be computed by observing only the local variables $V_j$ and $q_j^c$, and are given by,*

$$q_j^g = q_j^c - \alpha \beta_j \Delta V_j^{eff}, \quad \forall j \geq 1. \tag{6.9}$$

*Proof.* It is assumed that $V_0$ is set independent of the PV-inverters. The proof then follows by taking partial derivatives of the objective function $\mathcal{M}$ with respect to variables $q_j^g$ $\forall j \geq 1$ and using mathematical induction. Please refer to Appendix E for the details. ☐

## 6.4 Performance of the control law in (6.7)

Fig. 6.4 provides a comparison of the local control law (6.7) and the central optimization (6.6), for three distinct cases, 1) a *high import* case, Fig. 6.4(a), when the substation is supplying large active power to the feeder, 2) a *high export* case, Fig. 6.4(b), when the feeder is returning large active power back to the substation, and 3) a *balanced* situation, Fig. 6.4(c), when the generation from the PVs is almost balanced with the load consumption. It can be observed that the local control law almost always matches the optimal values, except when it has to compensate for neighboring PV sources that have encountered their limits, as seen in the extremities of Figs. 6.4(a) and 6.4(b).

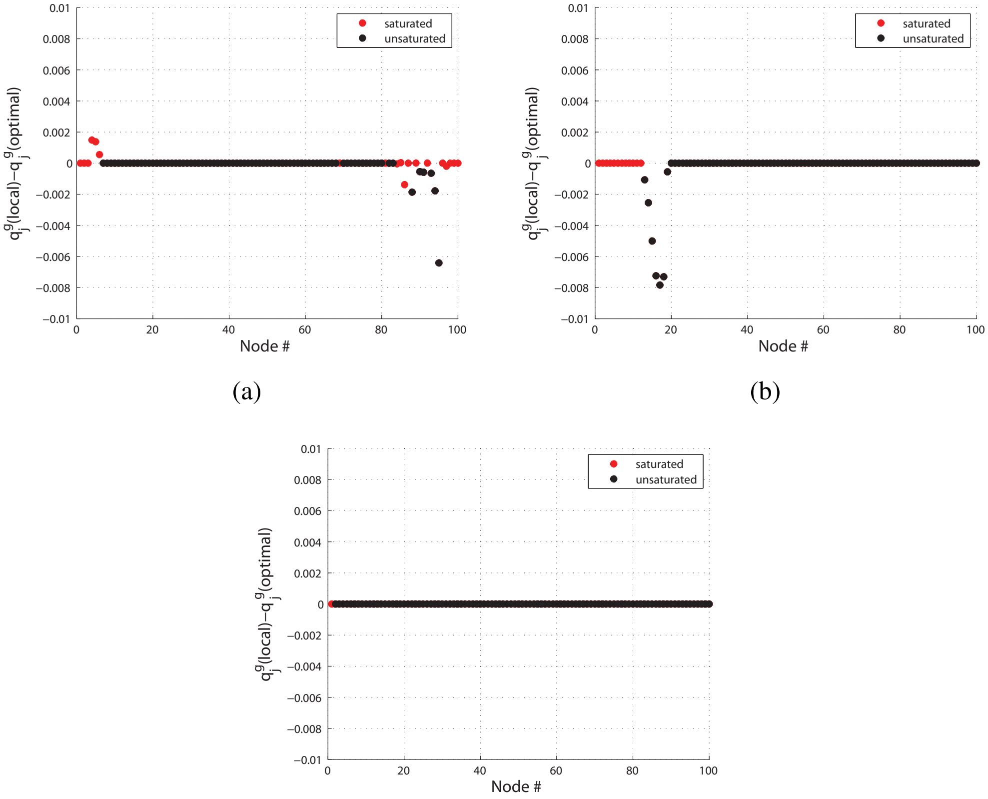

(a)

(b)

(c)

Figure 6.4: Testing optimality of the local control law in - (a) *high import*, (b) *high export*, and (c) *balanced* situation.

While the control law in (6.7) performs well in the simplistic feeder model in Section 6.1, further research is required to investigate more general situations. For example in a practical scenario it is expected that there would be less than 100% PV penetration, non-uniform ratio of line reactance to resistance ratio, and feeders with high line losses. Also it is likely that the feeder will have laterals, voltage regulators, and regulating transformers. To investigate some of these scenarios a modified IEEE-34 feeder model is considered.

## 6.5 Adjusted IEEE-34 Feeder

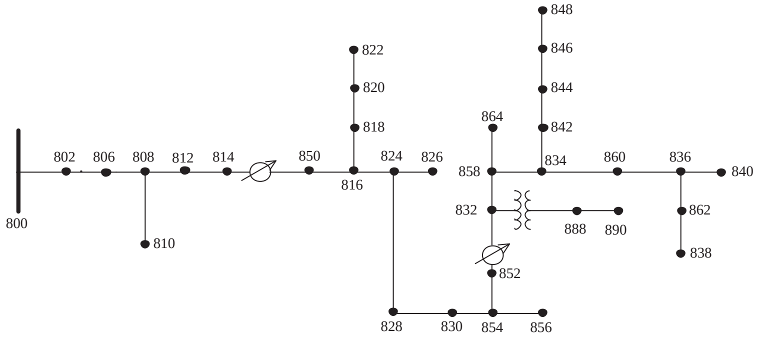

Figure 6.5: Comparison between the positive-sequence voltages for the three-phase model and the corresponding voltages for the single-phase equivalent model.

IEEE 34 node distribution, shown in Fig. 6.5, is an existing 24.9 kV feeder in Arizona [92,97]. To ease in our analysis, the three-phase feeder would be converted to an equivalent single-phase feeder. Fig. 6.6 shows a comparison of the positive sequence voltage of the actual IEEE-34 feeder and the voltage of the single-phase approximation of the feeder. It shows that the single phase approximation of the feeder is close to reality at most of the nodes except may be at nodes around 808-814 where the discrepancy can be attributed to signficant voltage imbalance (among three phases) at those locations.

In the previous example of a no-lateral feeder with 100 nodes, each of the nodes was assumed to be supplying a household and hence drawing active power of the order of a few kilo-Watts. However in IEEE-34 feeder, each node supplies a load that is a few order higher than a single household consumption. To take care of this mismatch, it is assumed that at each node, there are a number of houses (proportional to the amount of load at that node) each of which has an identical PV panel. Thus if we denote the average household active power consumption by $< p^c >$, maximum active power generation from a single PV panel by $p^g_{max}$ and size of a PV inverter as $s$, then at node $i$, there would be an "aggregated

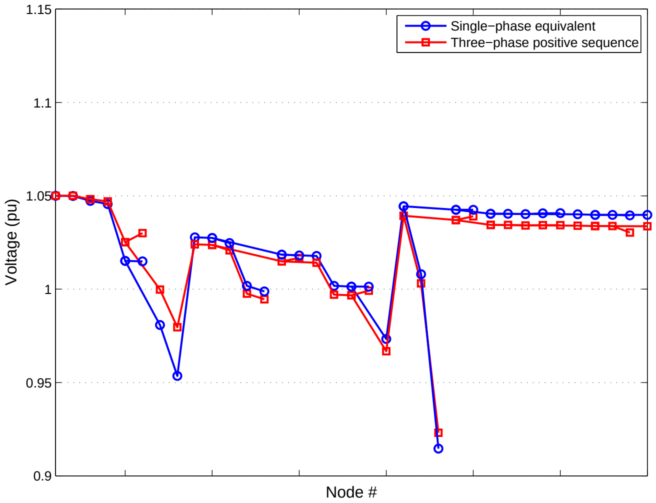

Figure 6.6: Comparison between the positive-sequence voltages for the three-phase model and the corresponding voltages for the single-phase equivalent model.

PV panel" with

$$\text{maximum generation, } p^g_{i,max} = p^g_{max} \frac{p^c_i}{< p^c >} \tag{6.10a}$$

$$\text{and size of inverter, } s_i = s \frac{p^c_i}{< p^c >} \tag{6.10b}$$

where, $p^c_i$ is the active power consumption at node $i$. For those nodes that do not draw any power, no PV panel is assumed to be present. Thus in contrast to the previous example, in this case we will have less than 100% penetration of PV panels. It is to be noted, that IEEE-34 feeder has quite a few "distributed loads" too. These distributed loads are converted to equivalent "spot loads" with the help of dummy nodes as discussed in [88].

One more important aspect of this feeder is the presence of voltage regulating elements - shunt capacitors at nodes 844 and 848, and the tap-changing transformers on the connecting lines 814-850 and 852-832. The presence of shunt capacitors can be handled easily by subtracting reactive power generation by the shunt capacitors from the consumer reactive load to obtain "net reactive power consumption" $q^c_i$ at node $i$.

## 6.6 Global Optimization

A central optimization problem is formulated in the same way as in (6.6). The optimization is run for three different loading scenarios, created by scaling the consumption level to - 50%, 100%, & 150% of the published data, and three representative weather conditions,

- *sunny*: all PV systems are generating at $p^g_j = p^g_{j,max}$,
- *night time*: all PV systems generate $p^g_j = 0$, and

- *partly cloudy*: first available PV system after substation, at some node 'j', is assigned either $p_j^g = 0.2\, p_{j,max}^g$ or $p_j^g = p_{j,max}^g$ both with probability 0.5, and each subsequent available PV system (also considering the lateral branches), at node 'k', is assigned

$$p_k^g = \begin{cases} p_{k,max}^g \dfrac{p_j^g}{p_{j,max}^g}, & \text{with probability } 0.9 \\ p_{k,max}^g \left(1.2 - \dfrac{p_j^g}{p_{j,max}^g}\right), & \text{with probability } 0.1 \end{cases} \tag{6.11}$$

Simulations are run for different loading and weather conditions, with five instances generated each time in a 'partly cloudy' scenario to evaluate possible PV generation sequences, and considering $\beta_j = 2\ \forall j$. The regulators between nodes 814 and 850, and between 832 and 852 are assumed to be simply maintaining equal voltages across their terminals. Optimal values of the reactive power from PV inverters, collected from all such simulations, were plotted together in Fig. 6.7 in order to find out any correlation between local variables. To compare with our findings on the no-lateral feeder of 100 nodes, a reference correlation, given in (6.9), is also shown in Fig. 6.7. While the actual line resistance over line reactance ratio varies throughout the IEEE-34 feeder, the ratios are relatively close, and a mean ratio is considered to obtain the reference correlation. When the size of a single PV unit is kept at 2.2 kW (Fig. 6.7(a)), a lot of the PV systems hit their saturation limits (marked by red dots). In such cases the rest of the PV systems would try to compensate and hence deviate from the local control strategy (6.9) which has no information of the other nodes. When simulations were re-run without the limits on reactive power support by the PV units (Fig. 6.7(b)), the optimal values come closer to the reference correlation. But even then the correlation is not quite clear, as opposed to the previously discussed main feeder case. This necessitates a re-evaluation of the local control strategy. In the next section, these aberrations would be investigated by obtaining some analytical insights into the globally

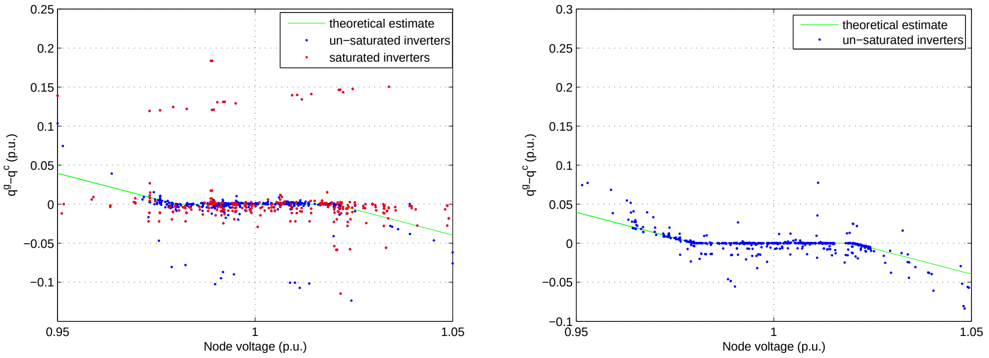

(a) Single PV inverter size, $s$ = 2.2 kW

(b) Single PV inverter size, $s = \text{inf}$

Figure 6.7: Correlations between the local observables $V_j$ and $q_j^c$ and the optimal reactive dispatch $q_j^g$, with voltage regulators maintaining equal voltage across terminals.

optimal solution.

## 6.7 Derivation of Optimal Solution

The case of IEEE-34 feeder presents a distinctive scenario in which many of the nodes do not participate in reactive power control. In fact this scenario is essentially similar to the effect a reactive power limit has on the optimal solutions, appearing as constraint in (6.6). Whenever a PV inverter at any node gets saturated by its reactive power limit, the node effectively ceases to provide any further reactive power support and hence should be treated as a simple non-PV node. Thus henceforth, for simplicity of analysis, it would be assumed that there are no limits to reactive power dispatch capability of the PV inverters. Additionally, as mentioned in Section 6.6, it is assumed that there is no voltage regulation along the length of the feeder, except the one at the substation (node $\#0$).

### 6.7.1 Grid Model

For simplicity, a main feeder structure with no lateral (Fig. 6.2) is considered as the grid model. The adjustments required to deal with branches would be discussed later. Let us denote the first node (the substation) as node $\#0$ and count up as we go farther, where $r_i$ and $x_i$ are the resistance and reactance of the edge between node $\#i$ and node $\#(i+1)$. $P_i$ and $Q_i$ are the real and reactive power coming out of node $\#i$ (entering the rest of the grid); $p_i^c$ and $q_i^c$ are the real and reactive power consumed at node $\#i$. As discussed in Section 6.5, the net reactive power consumption, $q_i^c$, is composed of the consumer reactive load, $q_i^L$, and the reactive power compensation, $q_i^{cap}$, through shunt capacitance (including line charging capacitance). $p_i^g$ and $q_i^g$ are the real and reactive power generated by photo-voltaic cells (PVs) sitting at node $\#i$. Thus,

$$q_i = q_i^c - q_i^g \tag{6.12a}$$

$$p_i = p_i^c - p_i^g \tag{6.12b}$$

$$\text{where,}\quad q_i^c = q_i^L - q_i^{cap}, \quad q_i^{cap} = q_{i,rated}^{cap} V_i^2 \tag{6.12c}$$

where, $q_{i,rated}^{cap}$ is the rated reactive power (in p.u.) supplied by the shunt capacitance at node $\#i$. Let us assume that there are $m \in \{1, 2, \ldots, N\}$, number of nodes having a PV system (with unlimited capacity of reactive support), and locations of the PV nodes form a set

$$\mathcal{K} = \{k_1, k_2, \ldots, k_m\}, \quad 1 \leq m \leq N \tag{6.13}$$

$$\text{where,}\ 1 \leq k_i < k_j \leq N, \quad \forall\, 1 \leq i < j \leq m$$

Consequently,

$$\forall\, i \notin \mathcal{K}, \quad s_i = q_i^g = p_i^g = p_{i,max}^g = 0 \tag{6.14}$$

### 6.7.2 Line Flow Properties

The power flow equations in a radial distribution feeder, with no laterals, can be simplified as, [85, 90, 96]

$$\forall i \in \{0,1,2,3,...,N-1\}, \quad P_i = P_{i+1} + r_i\left(P_i^2 + Q_i^2\right) + p_{i+1} \tag{6.15a}$$

$$Q_i = Q_{i+1} + x_i\left(P_i^2 + Q_i^2\right) + q_{i+1} \tag{6.15b}$$

$$V_{i+1}^2 = V_0^2 - 2\sum_{j=0}^{i}\left(r_j P_j + x_j Q_j\right) \tag{6.15c}$$

$$\text{with,} \quad P_N = Q_N = 0 \tag{6.15d}$$

where it is assumed that $V_i \approx 1$ (in p.u.), $\forall i$. In our case, the reactive power consumed at each node, $p_i$, is un-controllable while the reactive power, $q_i$, can be controlled at certain node locations $i \in \mathcal{K}$.

**Claim.** *Under all acceptable operating conditions, the following assumptions are valid*

$$\forall j \in \{0,1,\ldots,N-1\}, \; \forall k \in \mathcal{K}, \quad \frac{\partial P_j}{\partial q_k} = 0, \tag{6.16a}$$

$$\textit{and,} \quad \frac{\partial Q_j}{\partial q_k} = \begin{cases} 0, & k \le j \\ 1, & k \ge j+1 \end{cases} \tag{6.16b}$$

*Justification.* The relation (6.16a) follows from the fact that, in any distribution feeder, the active power losses are very small (usually less than 5%) and hence can be neglected in (6.15a). While in absence of any appreciable reactive power support, the reactive power losses could also be similarly be neglected in (6.15b), the argument fails in presence of reactive power control. Because of (6.16a), the line losses appearing in $\mathcal{M}$, (6.6), can be reduced by minimizing reactive power flows, $Q_i$. As $|Q_i| \to 0$, the reactive power losses in (6.15b) can no longer be neglected. However, in such scenarios, $(P_i^2 + Q_i^2) \approx P_i^2$ and (6.16b) follows rather trivially from (6.15b) and (6.16a). □

Also, the power flow equations in (6.15) can be rewritten as,

$$\forall i \in \{0,1,2,3,...,N-1\}, \quad P_i = P_{i+1} + p_{i+1} = \sum_{j=i}^{N-1} p_{j+1} \tag{6.17a}$$

$$Q_i = Q_{i+1} + x_i P_i^2 + q_{i+1} = \sum_{j=i}^{N-1}\left(x_j P_j^2 + q_{j+1}\right) \tag{6.17b}$$

$$V_{i+1}^2 = V_0^2 - 2\sum_{j=0}^{i}\left(r_j P_j + x_j Q_j\right) \tag{6.17c}$$

$$\text{with,} \quad P_N = Q_N = 0 \tag{6.17d}$$

Before moving on to solve the optimization problem, let us introduce the following notations,

$$\gamma_i := \frac{\sum_{n=k_i}^{k_{i+1}-1} x_n}{\sum_{n=k_i}^{k_{i+1}-1} r_n}, \qquad \forall i \in \{1, 2, \ldots, m-1\} \tag{6.18a}$$

$$\text{and, } \gamma_0 := \frac{\sum_{n=0}^{k_1-1} x_n}{\sum_{n=1}^{k_1-1} r_n} \tag{6.18b}$$

which would be helpful later on.

### 6.7.3 Solving the Optimization

With respect to the discussion in Section 6.7.1, the objective function can be rewritten as,

$$\min \mathcal{M}\left(q_k \,|k \in \mathcal{K}\right) = \sum_{j=0}^{N-1} \left(\beta_{j+1} \left(\Delta V_{j+1}^{eff}\right)^2 + r_j(P_j^2 + Q_j^2)\right) \tag{6.19}$$

where $\mathcal{K}$ was defined in (6.13). Optimal reactive power dispatch $q_i^g$'s can be computed uniquely from optimal $q_i$'s using (6.12). It is to be noted that, for ease of analysis, the voltage inequality constraints in (6.6) have been ignored. It would be assumed for the purpose of analytical computations, that generally, the objective function in (6.19) would keep the voltage deviations low, and any additional adjustment can be taken care of by the voltage regulator at the substation (node #0) and also by the weighing parameters $\beta_j$'s.

The optimization problem can be solved using the simultaneous equations,

$$\forall\, i \in \{1, 2, \ldots, m\}, \quad f_i := \frac{\partial \mathcal{M}\left(q_k \,|k \in \mathcal{K}\right)}{\partial q_{k_i}} = 0 \tag{6.20}$$

**Claim.** *Optimal solutions of (6.19) can be summarized as,*

$$
\begin{aligned}
&\forall\, i \in \{2,3,\dots,m-1\},\\
&q_{k_i} = -x_{k_i-1}P_{k_i-1}^2 - \sum_{j=k_{i-1}}^{k_i-2} \left(x_j P_j^2 + q_{j+1}\right) \left(\frac{\sum_{n=k_{i-1}}^{j} r_n}{\sum_{n=k_{i-1}}^{k_i-1} r_n}\right)\\
&\quad - \sum_{j=k_i}^{k_{i+1}-2} \left(x_j P_j^2 + q_{j+1}\right) \left(\frac{\sum_{n=j+1}^{k_{i+1}-1} r_n}{\sum_{n=k_i}^{k_{i+1}-1} r_n}\right) + \sum_{j=k_{i-1}}^{k_i-1} \frac{\beta_{j+1}\Delta V_{j+1}^{eff}}{V_{j+1}} \left(\frac{\sum_{n=k_{i-1}}^{j} x_n}{\sum_{n=k_{i-1}}^{k_i-1} r_n}\right)\\
&\quad + \sum_{j=k_i}^{k_{i+1}-2} \frac{\beta_{j+1}\Delta V_{j+1}^{eff}}{V_{j+1}} \left(\gamma_{i-1} - \frac{\sum_{n=k_i}^{j} x_n}{\sum_{n=k_i}^{k_{i+1}-1} r_n}\right) + (\gamma_{i-1} - \gamma_i) \sum_{j=k_{i+1}-1}^{N-1} \frac{\beta_{j+1}\Delta V_{j+1}^{eff}}{V_{j+1}}
\end{aligned}
\tag{6.21a}
$$

*and,*

$$
\begin{aligned}
&q_{k_1} = -x_{k_1-1}P_{k_1-1}^2 - \sum_{j=0}^{k_1-2} \left(x_j P_j^2 + q_{j+1}\right) \left(\frac{\sum_{n=1}^{j} r_n}{\sum_{n=1}^{k_1-1} r_n}\right)\\
&\quad - \sum_{j=k_1}^{k_2-2} \left(x_j P_j^2 + q_{j+1}\right) \left(\frac{\sum_{n=j+1}^{k_2-1} r_n}{\sum_{n=k_1}^{k_2-1} r_n}\right) + \sum_{j=0}^{k_1-1} \frac{\beta_{j+1}\Delta V_{j+1}^{eff}}{V_{j+1}} \left(\frac{\sum_{n=1}^{j} x_n}{\sum_{n=1}^{k_1-1} r_n}\right)\\
&\quad + \sum_{j=k_1}^{k_2-2} \frac{\beta_{j+1}\Delta V_{j+1}^{eff}}{V_{j+1}} \left(\gamma_0 - \frac{\sum_{n=k_1}^{j} x_n}{\sum_{n=k_1}^{k_2-1} r_n}\right) + (\gamma_0 - \gamma_1) \sum_{j=k_2-1}^{N-1} \frac{\beta_{j+1}\Delta V_{j+1}^{eff}}{V_{j+1}}
\end{aligned}
\tag{6.21b}
$$

$$
\begin{aligned}
&q_{k_m} = -x_{k_m-1}P_{k_m-1}^2 - \sum_{j=k_{m-1}}^{k_m-2} \left(x_j P_j^2 + q_{j+1}\right) \left(\frac{\sum_{n=k_{m-1}}^{j} r_n}{\sum_{n=k_{m-1}}^{k_m-1} r_n}\right)\\
&\quad - \sum_{j=k_m}^{N-1} \left(x_j P_j^2 + q_{j+1}\right) + \sum_{j=k_{m-1}}^{k_m-2} \frac{\beta_{j+1}\Delta V_{j+1}^{eff}}{V_{j+1}} \left(\frac{\sum_{n=k_{m-1}}^{j} x_n}{\sum_{n=k_{m-1}}^{k_m-1} r_n}\right)\\
&\quad + \gamma_{m-1} \sum_{j=k_m-1}^{N-1} \frac{\beta_{j+1}\Delta V_{j+1}^{eff}}{V_{j+1}}
\end{aligned}
\tag{6.21c}
$$

*Proof.* The proof follows in a similar way as in Theorem VI.1. Detailed calculations are in Appendix F. □

The optimal reactive power dispatch from PV inverters can be computed directly from (6.21) using the relations in (6.12).

## 6.8 Realizability Issues

The optimal solutions in (6.21) require the knowledge of system variables (power flow, node voltages) that are non-local with respect to the location of the PV inverter of concern. Thus it is not possible to compute the globally optimal $q_i^g$ values, simply by observing local quantities such as node voltage and nodal power consumption. To derive a reasonable local control law, it is necessary to estimate some of the global variables as well. Let us assume that the impedances are fixed and known to all the PV-nodes participating in control. Denoting by $f_i\left(.\right), \forall\, i \in \{1, 2, \ldots, m-1\}$, the dependence of optimal solutions $q_{k_i}$ on system variables, the following relations can be noted from (6.21), (6.12) and (6.14),

$$\begin{aligned} &\forall\, i \in \{2, 3, \ldots, m-1\}, \\ &\quad q^g_{k_i} = f_i\left(\left\{P_j, q^c_{j+1}\,|k_{i-1} \le j \le k_{i+1}-2\right\}; \{V_j\,|k_{i-1}+1 \le j \le N\}\right) \qquad (6.22a) \\ &\text{and,} \\ &\quad q^g_{k_1} = f_1\left(\left\{P_j, q^c_{j+1}\,|0 \le j \le k_2-2\right\}; \{V_j\,|1 \le j \le N\}\right) \qquad (6.22b) \\ &\quad q^g_{k_m} = f_m\left(\left\{P_j, q^c_{j+1}\,|k_{m-1} \le j \le N-1\right\}; \{V_j\,|k_{m-1}+1 \le j \le N\}\right) \qquad (6.22c) \end{aligned}$$

It is assumed that, if necessary, measurements can be made about the line power flow, node voltage, and load drawn at a PV-node [98]. Let us consider the decision to be taken by the PV-inverter at node $k_i, i \in \{1, 2, \ldots, m\}$, based on only local measurements: $V_{k_i}, q^c_{k_i}, p^g_{k_i}, p^c_{k_i}, P_{k_i}$ and $Q_{k_i}$. It can be argued that, with this set of local measurements, a reasonable estimation of the optimal reactive power dispatch, henceforth denoted as $\widehat{q^g_{k_i}}, \forall\, i \in \{1, 2, \ldots, m\}$, can be made with the help of fixed system parameters $x_j, r_j, \forall\, j \in \{0, 1, 2, \ldots, N-1\}$ and flow equations in (6.17). Different methods have been suggested to estimate the load at different nodes on a distribution feeder [99–101]. Therefore it would be fair to assume that reasonable estimates of the active and reactive power consumption: $\widehat{p^c_j},\ \widehat{q^c_j}, \forall j \in \{0, 1, 2, \ldots, N-1\}$, at different nodes can be made.

**Claim.** *Let us assume that real-time estimates of nodal power consumptions, $\widehat{p^c_j}$ and $\widehat{q^c_j}$, are available at each node $j \in \{0, 1, 2, \ldots, N-1\}$. Then, based on measurements of the quantities $V_{k_i}, q^c_{k_i}, p^g_{k_i}, p^c_{k_i}, P_{k_i}$ and $Q_{k_i}$ at PV-node $k_i,\ i \in \{1, 2, \ldots, m\}$, it is possible to compute estimates of the quantities:*

$$\left\{\widehat{V_l}, \widehat{P_l}, \widehat{Q_l}\,|\, k_{i-1} \le l \le k_{i+1}-1\right\}, \quad \textit{when, } i \in \{2, 3, \ldots, m-1\}, \qquad (6.23a)$$

$$\left\{\widehat{V_l}, \widehat{P_l}, \widehat{Q_l}\,|\, 0 \le l \le k_2-1\right\}, \quad \textit{when, } i = 1, \textit{ and,} \qquad (6.23b)$$

$$\left\{\widehat{V_l}, \widehat{P_l}, \widehat{Q_l}\,|\, k_{i-1} \le l \le N\right\}, \quad \textit{when, } i = m. \qquad (6.23c)$$

*where, $\widehat{P_N} = \widehat{Q_N} = 0$, by construction.*

*Proof.*

- Up-stream nodes:

From the power flow equations in (6.17), it follows that

$$\widehat{P_{k_i-1}} = P_{k_i} + p^c_{k_i} - p^g_{k_i} \tag{6.24a}$$

$$\widehat{Q_{k_i-1}} = Q_{k_i} + q^c_{k_i} - q^g_{k_i} + x_{k_i-1}\widehat{P_{k_i-1}}^2 \tag{6.24b}$$

$$\text{and, } \widehat{V_{k_i-1}} = \sqrt{V^2_{k_i} + x_{k_i-1}\widehat{Q_{k_i-1}} + r_{k_i-1}\widehat{P_{k_i-1}}} \tag{6.24c}$$

This way the estimates: $\widehat{V_{k_i-1}}, \widehat{q^c_{k_i-1}}, \widehat{p^c_{k_i-1}}, \widehat{P_{k_i-1}}$, and $\widehat{Q_{k_i-1}}$ become available for node $(k_i-1)$. Now if the node $(k_i-1)$ is a non-PV node, then further using the knowledge of $p^g_{k_i-1} = q^g_{k_i-1} = 0$ the corresponding quantities can be estimated at the node $(k_i-2)$, and continually at nodes $(k_i-n), n = \{1,2,3,\dots\}$. However, the estimation process stops at the node $(k_i-n) \equiv k_{i-1} \in K$ in which case accurate estimation of the quantities $p^g_{k_{i-1}}$ and $q^g_{k_{i-1}}$ is not possible, or if $(k_i-n) \equiv 0$ (occurs when $i=1$).

- Down-stream nodes:

  Similarly, if $(k_i+1) \notin K$ (i.e. $p^g_{k_i+1} = q^g_{k_i+1} = 0$ is known), the following computations are possible,

$$\widehat{P_{k_i+1}} = P_{k_i} - \widehat{p^c_{k_i+1}} \tag{6.25a}$$

$$\widehat{Q_{k_i+1}} = Q_{k_i} - \widehat{q^c_{k_i+1}} - x_{k_i}P^2_{k_i} \tag{6.25b}$$

$$\text{and, } \widehat{V_{k_i+1}} = \sqrt{V^2_{k_i} - x_{k_i}Q_{k_i} - r_{k_i}P_{k_i}} \tag{6.25c}$$

  This way the estimates: $\widehat{V_{k_i+1}}, \widehat{q^c_{k_i+1}}, \widehat{p^c_{k_i+1}}, \widehat{P_{k_i+1}}$, and $\widehat{Q_{k_i+1}}$ become available for node $(k_i+1) \notin K$. It is to be noted, that if instead $(k_i+1) \equiv k_{i+1} \in K$ (where, $i < m$), the estimates $\widehat{P_{k_i+1}}$ and $\widehat{Q_{k_i+1}}$ can not be computed because of lack of information on $p^g_{k_{i+1}}$ and $q^g_{k_{i+1}}$ (although the estimate of $\widehat{V_{k_{i+1}}}$ can still be computed). Thus, when $i < m$, all the estimates $\widehat{V_l}, \widehat{P_l}, \widehat{Q_l}, l \in \{k_i+1, k_i+2, \dots, k_{i+1}-1\}$ are possible. Of course, if $i = m$ , then the estimates $\widehat{V_l}, \widehat{P_l}, \widehat{Q_l}$ are possible all the way up to $l = N$ (with $\widehat{P_N} = \widehat{Q_N} = 0$).

The claim follows from combining the conclusions of above discussions. □

But the optimal solutions require the knowledge of voltages at all down-stream nodes, as noted in (6.22). However, in distribution feeders, it is very likely that the ratios of line reactance and line resistance of different long sections of the feeder would be almost equal to each other. Let us assume that,

$$\gamma_i = \gamma_j \qquad \forall\, i,j \in \{0,1,2,\dots,m-1\}\,. \tag{6.26}$$

Using (6.26) in (6.21), the dependence of the optimal solution, at PV-node $k_i$, on node voltage values can be shrunk to the set of nodes:

$$\begin{aligned}
\{k_{i-1}+1, k_{i-1}+2, \ldots, k_{i+1}-1\}, &\qquad \text{when } i \in \{2,3,\ldots,m-1\}, \\
\{1,2,\ldots,k_2-1\}, &\qquad \text{when } i = 1, \text{ and }, \\
\{k_{m-1}+1, k_{m-1}+2, \ldots, N\}, &\qquad \text{when } i = m;
\end{aligned}$$

at each of which the node voltages can be estimated from local measurements done at node $k_i \forall i$, as discussed in Claim 6.8. Hence it is possible to estimate the reactive power dispatch at each PV-node $k_i \in K$, based on only local measurement of the quantities $V_{k_i}, q^c_{k_i}, p^g_{k_i}, p^c_{k_i}, P_{k_i}$ and $Q_{k_i}$.

Finally, there is the issue of lateral branches. While a rigorous derivation of the optimal control law in such a case is tedious, and require to conisder numerous different configurations, a quick look at some simple examples can help in identifying the general modifications to be applied on the optimal control law in (6.21). To illustrate this, let us consider the Fig. 6.8 in which there are two PV-nodes (marked by red dot) at node# 3 and 5, and there are two lateral branches, 1-2 and 1-3, connected at node 1 to the main feeder (0-1-4-5). The node 0 is the substation node. The line flows, line impedances, and the voltage and (net) reactive power consumption at PV-nodes can be noted in the Fig. 6.8. Under the assumption of fixed line resistance to line reactance ratio throughout the feeder, the objective function in (6.19) can be solved for optimal values of net reactive power consumptions at the PV-nodes, i.e. the optimal values of $q_3$ and $q_5$, where in this case $\mathcal{K} = \{3, 5\}$. The

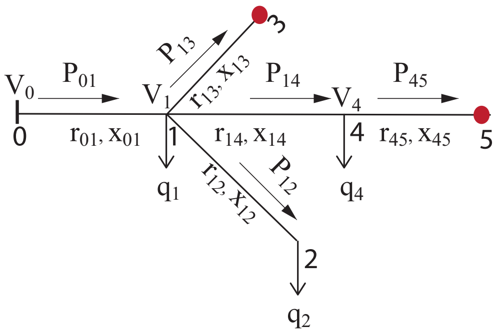

Figure 6.8: Examples of radial feeder structure with laterals.

optimal values can be found out to be,

$$\begin{aligned}
q_3 = &- x_{13}P_{13}^2 - \left(\left(x_{01}P_{01}^2 + q_1\right) + \left(x_{12}P_{12}^2 + q_2\right)\right) \frac{r_{01}||(r_{14} + r_{45})}{r_{01}||(r_{14} + r_{45}) + r_{13}} \\
&- \left(x_{14}P_{14}^2 + q_4\right) \frac{r_{45}}{r_{45} + r_{14}} \frac{r_{01}||(r_{14} + r_{45})}{r_{01}||(r_{14} + r_{45}) + r_{13}} + \frac{\beta_3 \Delta V_3^{eff}}{V_3} \frac{x_{01}||(x_{14} + x_{45}) + x_{13}}{r_{01}||(r_{14} + r_{45}) + r_1 3} \\
&+ \left( \frac{\beta_1 \Delta V_1^{eff}}{V_1} + \frac{\beta_2 \Delta V_2^{eff}}{V_2} \right) \frac{x_{01}||(x_{14} + x_{45})}{r_{01}||(r_{14} + r_{45}) + r_{13}} \\
&+ \frac{\beta_4 \Delta V_4^{eff}}{V_4} \frac{x_{45}}{r_{45} + r_{14}} \frac{x_{01}||(x_{14} + x_{45})}{r_{01}||(r_{14} + r_{45}) + r_{13}}
\end{aligned} \tag{6.27a}$$

$$\begin{aligned}
q_5 = &- x_{45}P_{45}^2 - \left(\left(x_{01}P_{01}^2 + q_1\right) + \left(x_{12}P_{12}^2 + q_2\right)\right) \frac{r_{01}||r_{13}}{r_{01}||r_{13} + r_{14} + r_{15}} \\
&- \left(x_{14}P_{14}^2 + q_4\right) \frac{r_{01}||r_{13} + r_{14}}{r_{01}||r_{13} + r_{14} + r_{15}} + \frac{\beta_5 \Delta V_5^{eff}}{V_5} \frac{x_{01}||x_{13} + x_{14} + x_{15}}{r_{01}||r_{13} + r_{14} + r_{15}} \\
&+ \left( \frac{\beta_1 \Delta V_1^{eff}}{V_1} + \frac{\beta_2 \Delta V_2^{eff}}{V_2} \right) \frac{x_{01}||x_{13}}{r_{01}||r_{13} + r_{14} + r_{15}} + \frac{\beta_4 \Delta V_4^{eff}}{V_4} \frac{x_{01}||x_{13} + x_{14}}{r_{01}||r_{13} + r_{14} + r_{15}}
\end{aligned} \tag{6.27b}$$

where, the symbol || is used to represent equivalent parallel impedance (resistance and/or reactance), i.e. $z_1||z_2 := z_1 z_2 / (z_1 + z_2)$. Interesting thing to note here is that with only local measurements at nodes 3 and 5, the respective optimal values can be computed if a good estimate of the quantities $q_1, q_2$ and $q_4$ are available, and the line parameters are known. This observation is consistent with the discussions earlier in this section. Furthermore, a closer look at the multiplying terms associated with $\left(x_{ij}P_{ij}^2 + q_j\right)$ reveal a nice pattern. For example, the multiplier associated with $(x_{14}P_{14}^2 + q_4)$ in (6.27a) can be thought of as the voltage (in Volt) that would have appeared at node 4, if a DC voltage source of 1 Volt magnitude was connected at node 3 and the other power sources in the grid (e.g. sub-station node, voltage regulators, other PV-nodes, etc.) were connected to 'ground', i.e. zero voltage. Similar observation holds with the voltage deviation terms, with the difference that the numerator has corresponding reactance values. While this is true for all 'up-stream' nodes with respect to the concerned PV-node, similar observation can be made with 'down-stream' nodes too, in which case too the factor is directly related to potential-divider type of setup. For a quick check, please refer to the optimal $q_{k_i}$ in (6.21). The multipliers associated the voltage deviation terms for nodes $(k_i + 1)$ to $(k_{i+1} - 1)$ can be computed directly using the potential-divider analogy. Thus it is possible to extend the result of (6.21) to feeders with lateral branches, under the assumption that line reactance and resistance ratios are same within the feeder.

## 6.9 Numerical Results

### 6.9.1 No active voltage regulator, no active voltage constraint

Three typical scenarios - when a active large power is drawn from the grid through the sub-station node; when a large active power is fed back into the grid; and when a there is a party cloudy condition with a random sequence of solar power generation between PV-nodes, have been studies on the modified IEEE-34 feeder (Section 6.5). The $\beta_j$ values in (6.6) are generally chosen to be equal to 2, except at the node 890 at the which the weighting factor of the voltage is assigned a value 7.

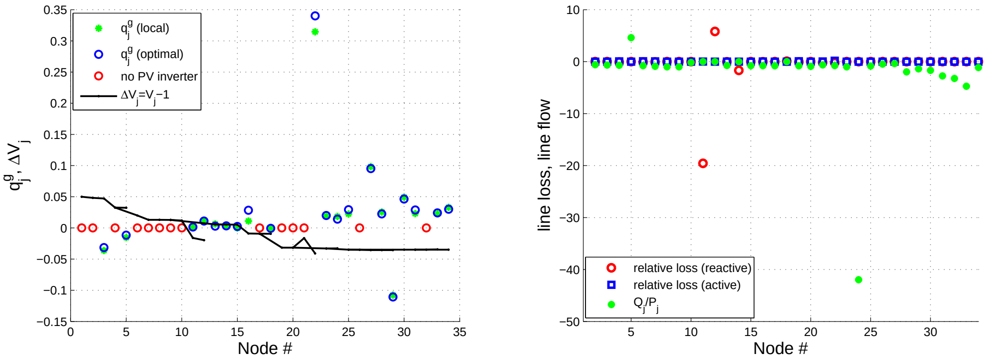

(a) Reactive power dispatch at PV-nodes

(b) Ratio of reactive to active power flow, and relative line losses

Figure 6.9: High consumption, night sky (no generation).

Fig. 6.9 presents results from a numerical simulation when the consumption of power is at 150% of the rated value, with none of the PV-units generating any solar power. The first node is the sub-station node, marked as 800 in the feeder diagram, and all other nodes are placed subsequently in the same order as in the feeder diagram. As expected, this scenario causes a generally decreasing voltage profile away from the sub-station (node 800, or the first node), in Fig. 6.9(a). The reactive power dispatch from the PV-inverters, as calculated using the strategy developed in this work, compares fairly well with the values computed through a global (central) optimization routine. Fig. 6.9(b) shows three ratios along the feeder length - the ratios between reactive line loss and reactive line flow; between active line loss and active line flow; and between reactive and active line flows. The values support the claims in Section 6.7.2 that - active line loss is negligible compared to active line flow; and reactive line loss can safely be attributed to the corresponding active line flow.

Fig. 6.10 shows a scenario when the consumption is at a low level - 50% of rated, and the PV-generation is at its maximum, with a generally increasing voltage profile away from the sub-station. Reactive power dispatch values computed from the local strategy and the global optimization are in generally close agreement (Fig. 6.10(a)). While Fig. 6.10(b)

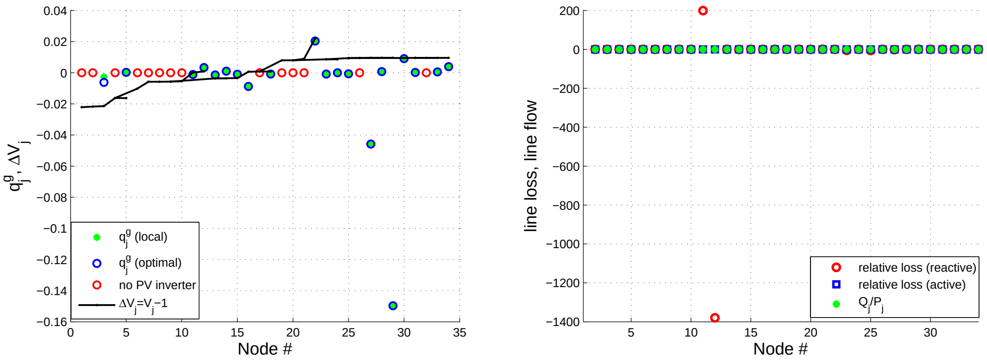

(a) Reactive power dispatch at PV-nodes

(b) Ratio of reactive to active power flow, and relative line losses

Figure 6.10: Low consumption, sunny sky (maximum generation).

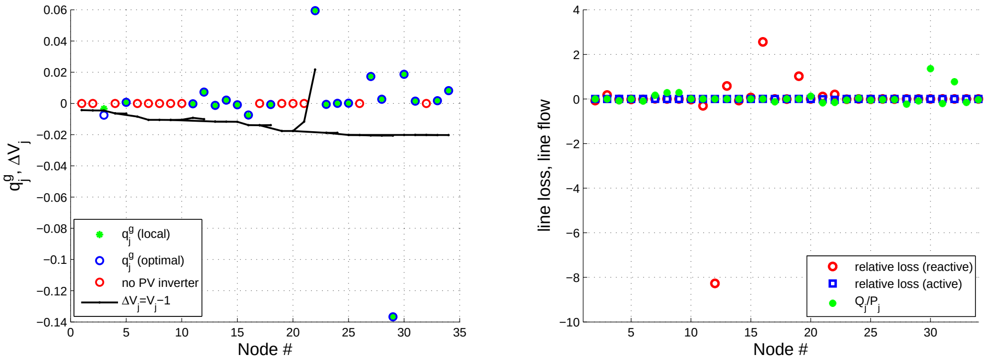

(a) Reactive power dispatch at PV-nodes

(b) Ratio of reactive to active power flow, and relative line losses

Figure 6.11: Moderate consumption, partly cloudy sky (non-uniform generation).

justifies the claims in Section 6.7.2. Finally a typical scenario with a moderate consumption (100% of rated) and partly cloudy sky condition is presented in Fig. 6.11.

### 6.9.2 Effect of active voltage regulator and active voltage constraints

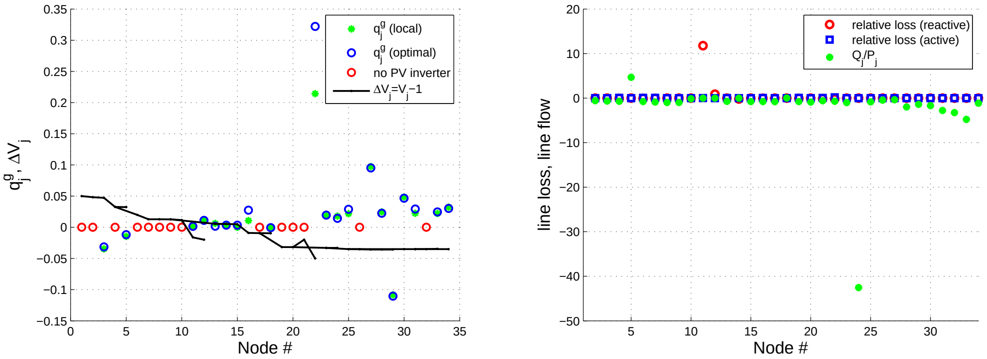

(a) Reactive power dispatch at PV-nodes

(b) Ratio of reactive to active power flow, and relative line losses

Figure 6.12: High consumption, night sky (no generation), with $\beta_j = 2 \forall j$.

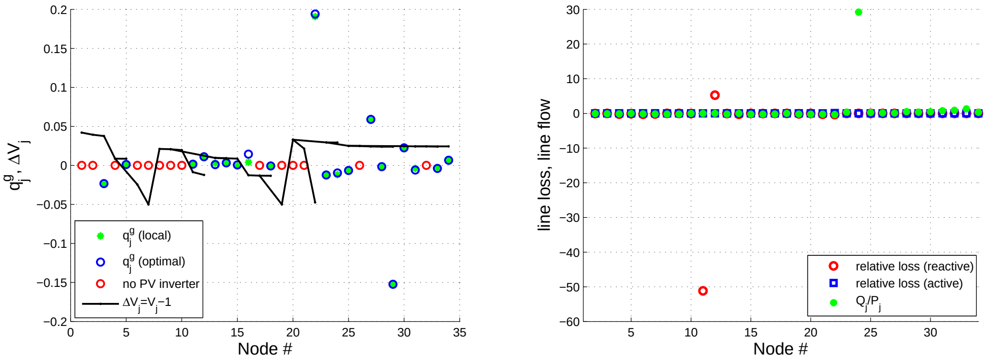

(a) Reactive power dispatch at PV-nodes

(b) Ratio of reactive to active power flow, and relative line losses

Figure 6.13: High consumption, night sky (no generation), with $\beta_j = 2 \forall j$ and active line-voltage-regulators.

Before concluding this section, let us explore the issue of voltage constraints in the optimization problem (6.6). Fig. 6.12 shows the scenario when there is a large import of active power, as in Fig. 6.9, except that now the weighting factors, $\beta_j$, are all equal to 2. As a result the voltage at node 890 (marked as node# 22 in the x-axis) is allowed to decrease further and hits the minimum allowed value 0.95 p.u.. Thus the voltage constraint in (6.6) now becomes active the reactive power dispatch has to increase further to keep satisfying the voltage constraint. This results in a significant mis-match, at node 890, between the reactive dispatch values computed from global optimitization and the local strategy which does not consider active constraints. However, this mis-match can be removed by carefully choosing $\beta_j$'s so that none of the voltage constraints becomes active. Alternatively, presence of active line-voltage-regulators (between nodes 852 and 832, and nodes 814 and 850) can provide required additional reactive power support, thereby reducing the burden on PV-inverters. Shown in Fig. 6.13 is a typical such situation. In this case, the $\beta_j$ values are all set to 2, but the voltage regulators are now actively operating to minimize the objective function in (6.6). As a result the globally optimal and the locally computed values of reactive power dispatch, even at node 890, are very closely matched.

## 6.10 Summary

In this chapter a solution is proposed for designing realizable strategy that can locally control the reactive power dispatch from PV-inverters using the measurements made only at the PV-node. Both the line losses and the voltage deviations across the feeder have been considered to evaluate globally optimal reactive power dispatch solutions. Numerical studies have been done to validate the applicability of the designed distributed control algorithm. Various issues affecting the decision have been discussed. It is shown that if each node of the feeder has an installed PV-inverter and the line reactance and line resistance ratio remains constant throughout the feeder, then strictly local control law can be derived that guarantees optimal performance in terms of minimizing a weighted combination of power losses and voltage deviations. It is also shown that an exact optimal solution can be computed in a more practical scenario under the presence of other voltage regulating elements, less than 100% penetration of PV-inverters. With reasonable assumptions, a locally computable control law is derived from the optimal solution. Simulation results are presented to compare the performance of this derived local control law that under varying conditions. It is observed that although this derived local control law may not be truly optimal, but with good choice of weights in the optmization function, the local control law can be made to perform satisfyingly close to the global optimal.

# CHAPTER VII

# Conclusions

## 7.1 Accomplishments

In the scope of this thesis work, different aspects and challenges of integration of renewable energy resources and plug-in electric vehicles have been looked at. This dissertation addresses the key challenges in integrating a large number of electrical loads, which have been shown to be prone to synchronization leading to instability in the grid. Analytical model-based control has been developed that can prevent such synchronizations, and efficiently shape the aggregate demand. It has been shown that such control can help in providing ancillary services to the grid, such as mitigating large and fast fluctuations in renewable generation, or filling the overnight valley in electricity demand. Distributed control algorithms have been developed that can effectively control the reactive power output from photo-voltaic inverters, under varying solar irradiance and varying electricity demand. A more detailed account of the accomplishments is provided below.

Based on a probabilistic approach, a linearized state-space model has been developed to capture the aggregate demand response of a large homogeneous group of thermostatically-controlled-loads when the temperature set-point of all the thermostats is disturbed by the same magnitude. This could be done in a centralized set-up where a common signal to change set-point would be broaadcast to all the participating loads. Based on this aggregate linear model, a linear feedback controller has been designed, which is shown to perform satisfactorily in terms of tracking a fluctuating reference power profile possibly coming from a renewable energy source. Although the model is based on a homogeneity assumption, the control action works well for a slightly heterogeneous ensemble.

A hysteresis-based charging scheme has been proposed for plug-in electric vehicle charging, such that actual charge of a battery would follow certain nominal charge profile within the tolerance of a deadband around it. Based on the charge dynamics generated by such hysteresis, a probabilistic approach has been adopted to model the aggregate demand response of a large homogeneous population of vehicle chargers to uniform change in nominal charging profile. A nonlinear (sliding mode) feedback control is shown to force aggregate charging demand into tracking valley filling trajectory, and fluctuating generation.

The impact of voltage sag induced synchronized tripping of plug-in electric vehicle chargers on voltage profile in the grid has been studied. It has been show that in realistic scenarios such synchronized behavior could potentially result in dangerous overvoltage situations. An analysis tool has been developed to identify a safe penetration level of plug-in electric vehicles that guarantee against such overvoltage events. It has also been stressed that a modification in current standard is required to safe-guard against such potential hazards.

When considering a large number of electrical loads, a synchronizing event (such as a set point change, or a fault-induced voltage sag) can lead to undesirable power and/or voltage swings in the grid. Analysis has been carried out to build a model that can truly capture the demand response to a hysteresis-based control signal. Using an initial estimation/information of the probability distribution of the electrical loads (e.g. temperature distribution of thermostats, normalized state-of-charge distribution of plug-in electric vehicle chargers), the model is shown to accurately predict the system behavior under a non-restrictive set of control inputs. Strange behaviors, such as high periodicity, have been reported to occur when certain types of control input is applied to a large aggregation hysteresis-based PEV chargers. Bifurcation diagrams are plotted to show that a period-adding cascade occurs as the control inputs periodicity is varied.

Distributed control algorithms have been studied to control reactive power output from photo-voltaic inverters in a distribution feeder. It has been shown under simplifying assumption, e.g. constant line resistance to line reactance ratios, optimal local control law can be derived. While this control law matches the globally optimal control algorithm in a linear radial feeder (with no laterals) and 100% penetration, it needs to be modified to be applied in the real-life scenario. Taking the example of a standard IEEE-34 distribution feeder, a global optimal solution has been derived. From this global optimal solution, it is then shown that an effective locally computable control law can be synthesized. Performance of this modified local control law is verified against varying conditions, and in a realistic set up. It has been shown how this locally computable control law can satisfactorily peform near-optimally with some smart choice of optimization parameters, and effective estimation of neighborhood load consumption.

## 7.2 Future Works

There are some interesting issues that need to be taken care of for a successful deployment of demand side control, or distributed generation control. For practical application of any control design, it needs to be made sure that the model used for analysis is as accurate as possible and that the controller is robust against any modeling uncertainties. Further research is required in these directions.

Hysteresis-based control of plug-in electric vehicle chargers is fundamentally different from that of the thermostats. For example, there is a limitation on controllability of vehicle chargers posed by their charge capacity. Simulations show loss of controllability both at the start and end of the charging duration. On the other hand, it may be observed that towards the end as more and more chargers become full, the effective population size decreases and demand response gets weaker. It would be interesting to model the response as the total populations size changes (increases during start up, while decreases during charging completion), possibly by formulating the problem as a Markov process by taking into account the random plug-in and plug-off process of PEVs. Another important direction is to quantify the effect of system heterogeneity into the analytical model. As discussed in this dissertation, heterogeneity among the PEV chargers leads to damped oscillatory response to step input. While in [34] a method was developed to quantify the effect of heterogeneity in a single parameter, it becomes increasingly difficult to model the effect multiple heterogeneous parameters. Also further research needs to be done to characterize the nonlinear phenomena observed in Chapter V. It might be useful to apply Poincaré map analysis to record the movement of eigen values of the system.

The models developed in this thesis work require very good knowledge of the population of loads. Information such as the number of loads “interested in/available for” control action, load parameters such as thermal capaitance and resistance for thermostats, and charge requirement of vehicle batteries are often difficult to exactly know. Most likely, in practial scenarios an online estimation of parameters would have to be done at certain intervals. One scheme is to inject pseudo-random noise and look for cross-correlation with changes in the total load [29]. The injected signal would need to be consistent with the control bandwidth. Robustness analysis needs to be done to test the controller performance under model uncertainties. Robustness is very important for the distributed control algorithm developed in Chapter VI. The control law depends on reliable estimate of the load consumption by non-photo-voltaic nodes in a closed neighborhood. As in practice, this estimate may not always be true, care must be taken to ensure the distributed control still remains robust.

## 7.3 List of Publications

Some of the works presented or discussed in this dissertation can be found in the following publications (including those under review, and in preparation):

### Refereed Journals

- Soumya Kundu, Ian A. Hiskens and Scott Backhaus, “Local Control of Photo-voltaic Inverters in a Distribution Feeder”. (in preparation for IEEE Transactions on Power Systems)

- Soumya Kundu and Ian A. Hiskens, “Overvoltages due to Plug-in Electric Vehicle Charger Response to Voltage Dips”, *IEEE Transactions on Power Delivery*. (under review)

- Nikolai A. Sinitsyn, Soumya Kundu and Scott Backhaus, “Safe protocols for generating power pulses with heterogeneous populations of thermostatically controlled loads”, *Energy Conversion and Management*, vol. 67, pp. 297-308, Mar 2013

**Conference Proceedings**

- Soumya Kundu and Ian A. Hiskens, “Nonlinear Dynamics of Hysteresis-based Load Controls”, $52^{nd}$ *IEEE Conference on Decision and Control.* (under review)
- Soumya Kundu and Ian A. Hiskens, “State-space Modeling of Hysteresis-based Control Schemes”, $12^{th}$ *European Control Conference*, Zürich, Switzerland, Jul 2013. (accepted)
- Soumya Kundu, Scott Backhaus and Ian A. Hiskens, “Distributed Control of Reactive Power from Photovoltaic Inverters”, *2013 IEEE International Symposium on Circuits and Systems (ISCAS)*, Beijing, China, May 2013. (to be published)
- Soumya Kundu and Ian A. Hiskens, “Hysteresis-based Charging Control of Plug-in Electric Vehicles”, $51^{st}$ *IEEE Conference on Decision and Control*, Maui, Hawaii, USA, Dec 2012.
- Soumya Kundu and Nikolai Sinitsyn, “Safe protocol for controlling power consumption by a heterogeneous population of loads”, *The* 2012 *American Control Conference*, Montréal, Canada, Jun 2012.
- Soumya Kundu, Nikolai Sinitsyn, Scott Backhaus and Ian A. Hiskens, “Modeling and control of thermostatically-controlled-loads”, $17^{th}$ *Power Systems Computation Conference*, Stockholm, Sweden, Aug 2011.

# APPENDICES

# APPENDIX A

# Computation of $\mathbf{G}_a(s, \tau_a)$ and $\mathbf{G}_b(s, \tau_b)$ in Chapter II

This appendix provides an outline of the steps involved in deriving the expressions for $\mathbf{G}_a(s, \tau_a)$ and $\mathbf{G}_b(s, \tau_b)$. Derivation of the expressions for $\mathbf{G}_c(s, \tau_c)$ and $\mathbf{G}_d(s, \tau_d)$ is similar to that of $\mathbf{G}_a(s, \tau_a)$ and hence is not included.

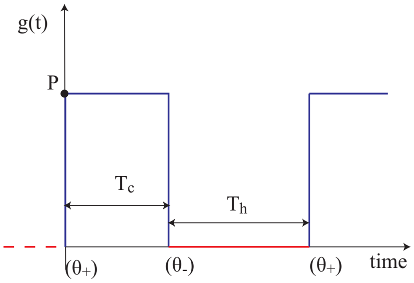

Figure A.1: The reference square-wave $g(t)$.

A. Derivation of $\mathbf{G}_a(s, \tau_a)$

We note that the waveform $g_a(t, \tau_a)$ shown in Figure 2.6 is a time-shifted square-wave. Considering the waveform $g(t)$ in Figure A.1, where $g(t) = 0$ for $t < 0$, we can express $g_a(t, \tau_a)$ as $g_a(t, \tau_a) = g(t - \tau_a)\mathbf{1}(t)$, where $\mathbf{1}(t)$ is the unit-step function, defined as

$$\mathbf{1}(t) = \begin{cases} 1, & t \geq 0 \\ 0, & t < 0. \end{cases} \tag{A.1}$$

The Laplace transform of the square-wave $g(t)$ is $\mathbf{G}(s) = \frac{P(1-e^{-sT_c})}{s(1-e^{-s(T_c+T_h)})}$. Hence, the Laplace transform of $g_a(t, \tau_a)$ is

$$\begin{aligned} \mathbf{G}_a(s, \tau_a) &= \int_0^\infty g_a(t, \tau_a) e^{-st} dt \\ &= e^{-s\tau_a} \mathbf{G}(s) \end{aligned} \tag{A.2}$$

The expressions for $\mathbf{G}_c(s,\tau_c)$ and $\mathbf{G}_d(s,\tau_d)$ can be derived similarly.

B. Derivation of $\mathbf{G}_b(s,\tau_b)$

The square-wave $g_b(t,\tau_b)$ can be expressed as $g_b(t,\tau_b) = g(t+T_c-\tau_b)\mathbf{1}(t)$ and its Laplace transform as

$$\begin{aligned}\mathbf{G}_b(s,\tau_b) &= \int_0^\infty g_b(t,\tau_b)e^{-st}dt \\ &= \int_0^\infty g(t+T_c-\tau_b)\mathbf{1}(t)e^{-st}dt \\ &= \int_0^\infty g(t+T_c-\tau_b)e^{-st}dt \\ &= \int_{T_c-\tau_b}^\infty g(t^*)e^{-s(t^*-T_c+\tau_b)}dt^*\end{aligned}$$

where $t^* = t+T_c-\tau_b$. Therefore,

$$\begin{aligned}\mathbf{G}_b(s,\tau_b) =& e^{s(T_c-\tau_b)}\int_{T_c-\tau_b}^\infty g(t^*)e^{-st^*}dt^* \\ =& e^{s(T_c-\tau_b)}\int_0^\infty g(t^*)e^{-st^*}dt^* \\ & \quad - e^{s(T_c-\tau_b)}\int_0^{T_c-\tau_b} g(t^*)e^{-st^*}dt^* \\ =& e^{s(T_c-\tau_b)}\mathbf{G}(s) \\ & \quad - e^{s(T_c-\tau_b)}\int_0^{T_c-\tau_b} Pe^{-st^*}dt^* \\ =& e^{s(T_c-\tau_b)}\mathbf{G}(s) \\ & \quad - e^{s(T_c-\tau_b)}P\frac{\left(1-e^{-s(T_c-\tau_b)}\right)}{s} \\ =& e^{s(T_c-\tau_b)}\mathbf{G}(s) - P\frac{\left(e^{s(T_c-\tau_b)}-1\right)}{s}. \qquad \text{(A.3)}\end{aligned}$$

# APPENDIX B

# Proof of convergence of the control Law in Chapter III

A proof of convergence of the error $e(t)$ in (3.23) to zero is presented here. Using the control law in (3.25)-(3.26), we can write from (3.23),

$$\begin{aligned}
\dot{S}(t) &= \dot{e}(t) + c_i e(t) \\
&= \dot{y}(t) - \dot{y}_d(t) + c_i e(t) \\
&= \mathbf{CA}x(t) + \mathbf{CB}u(t) + D\dot{u}(t) - \dot{y}_d(t) + c_i e(t) \\
&= \mathbf{CB}u(t) - \mathbf{CB}\hat{u}(t) - \eta S(t) \\
&= \mathbf{CB}u(t) - \frac{\mathbf{CB}}{D}\left(y_d(t) - \mathbf{C}x(t)\right) - \eta S(t) \\
&= \frac{\mathbf{CB}}{D} e(t) - \eta S(t) \\
&= -\left(\eta - \frac{\mathbf{CB}}{D}\right) e(t) - \eta c_i \int_0^t e(\tau)\, d\tau \\
\Rightarrow \dot{e}(t) + c_i e(t) &= -\left(\eta - \frac{\mathbf{CB}}{D}\right) e(t) - \eta c_i \int_0^t e(\tau)\, d\tau
\end{aligned}$$

Differentiating both sides gives,

$$\ddot{e}(t) + \left(c_i + \eta - \frac{\mathbf{CB}}{D}\right)\dot{e}(t) + \eta c_i e(t) = 0. \tag{B.1}$$

The error $e(t)$ will converge exponentially to zero if the roots of the following quadratic equation

$$s^2 + \left(c_i + \eta - \frac{\mathbf{CB}}{D}\right) s + \eta c_i e(t) = 0 \tag{B.2}$$

have negative real parts. This is true if the design variables $\eta$ and $c_i$ are chosen so that,

$$\left(c_i + \eta - \frac{\mathbf{CB}}{D}\right) > 0 \tag{B.3}$$

$$\left(c_i + \eta - \frac{\mathbf{CB}}{D}\right)^2 < 4\eta c_i \tag{B.4}$$

The control error $e(t)$ will then exhibit damped oscillations. For (B.4) to hold, $c_i$ must be positive. Hence integral control plays an important role in achieving successful tracking performance.

# APPENDIX C

# An outline of the derivation of (4.1)

Basic circuit relationships give,

$$\frac{V_\infty \angle 0 - V\angle\theta}{r+jx} = \frac{p-jq}{V\angle-\theta}$$

where $q=-bV^2$. Therefore,

$$\begin{aligned} V_\infty\angle 0 &= V\angle\theta + \frac{(p-jq)(r+jx)}{V\angle-\theta} \\ &= \frac{V^2+pr+qx+j(px-qr)}{V\angle-\theta}. \end{aligned}$$

The magnitude squared of both sides is,

$$V_\infty^2 = \frac{(V^2+pr+qx)^2+(px-qr)^2}{V^2}$$

which simplifies to,

$$V_\infty^2 = V^2 + 2(pr+qx) + \frac{(p^2+q^2)(r^2+x^2)}{V^2}.$$

Substituting $q=-bV^2$ and simplifying gives,

$$V_\infty^2 = \Big((1-bx)^2+(br)^2\Big)V^2 + 2pr + \frac{p^2\big(r^2+x^2\big)}{V^2}.$$

Multiplying throughout by $V^2$ and grouping terms gives (4.1).

## APPENDIX D

# Proof of the Theorem V.1

Before proceeding to the proof, let us define,

$$\Delta^U(t) := \text{Position of the upper deadband limit (right wall) at time } t \tag{D.1a}$$
$$\Delta^L(t) := \text{Position of the lower deadband limit (left wall) at time } t \tag{D.1b}$$
$$\Rightarrow\ \Delta^U(t) = \Delta^L(t) + \Delta, \quad \forall\, t. \tag{D.1c}$$

Also it would be assumed that the control input $u(t)$ is a continuous function in $t$, i.e. $v(t)$ always exists. Although in theory, this assumption puts a restriction on the use of 'instantaneous' jumps (e.g. step change) in control input, this is usually true in all practical situations where any centrally dispatched control signal can be effectively interpolated into a continous one. For example, a step change in the control input between two subsequent discrete time instants can be approximated by a very fast ramp signal.

*Proof.* It can be noted that the time interval $t \in (t_0, \infty)$ could be divided into different sub-intervals each characterized by either of the four different scenarios: no switching at either of the boundaries, switching at only the upper boundary (or, equivalently, only at the lower boundary), and switching at both the boundaries. The modified goal here is to prove that, for any such sub-interval denoted by $(t_1, t_2]$, the following is true:

$$\exists\, t_1 \geq t_0 \mid \max\left(\widetilde{SoC}^U_{on}(t_1), \widetilde{SoC}^U_{off}(t_1)\right) - \min\left(\widetilde{SoC}^L_{on}(t_1), \widetilde{SoC}^L_{off}(t_1)\right) \leq \Delta, \tag{D.2a}$$

$$\implies \forall\, t \in (t_1, t_2],\ \max\left(\widetilde{SoC}^U_{on}(t), \widetilde{SoC}^U_{off}(t)\right) - \min\left(\widetilde{SoC}^L_{on}(t), \widetilde{SoC}^L_{off}(t)\right) \leq \Delta. \tag{D.2b}$$

Then the proof of the Theorem V.1 follows by simple application of induction. Next, each of the four different possibilities would be considered individually. Before dealing with individual cases, let us note this relation that comes from the definitions (D.1),

$$\forall\, t, \quad \widetilde{SoC}^{U}_{on}(t) \leq \Delta^U(t) = \Delta^L(t) + \Delta \leq \widetilde{SoC}^{L}_{off}(t) + \Delta \tag{D.3}$$

A. <u>No switching during $(t_1, t_2]$</u>

Since the system is homogeneous, and there is no switching, the following holds,

$$\begin{aligned} &\forall\, t \in (t_1, t_2], \\ &\quad \widetilde{SoC}^{U}_{on}(t) - \widetilde{SoC}^{L}_{on}(t) = \widetilde{SoC}^{U}_{on}(t_1) - \widetilde{SoC}^{L}_{on}(t_1) \leq \Delta \quad \text{[from (D.2a)]} \end{aligned} \tag{D.4}$$

and similarly,

$$\widetilde{SoC}^{U}_{off}(t) - \widetilde{SoC}^{L}_{off}(t) \leq \Delta \tag{D.5}$$

Also, because $\alpha_{off} < \alpha_{on}$,

$$\begin{aligned} \forall\, t \in (t_1, t_2], \quad \widetilde{SoC}^{U}_{off}(t) &= \widetilde{SoC}^{U}_{off}(t_1) + \alpha_{off}\,(t - t_1) \\ &\leq \widetilde{SoC}^{L}_{on}(t_1) + \Delta + \alpha_{off}\,(t - t_1) \quad \text{[applying (D.2a)]} \\ &< \widetilde{SoC}^{L}_{on}(t_1) + \Delta + \alpha_{on}\,(t - t_1) \\ &< \widetilde{SoC}^{L}_{on}(t) + \Delta \end{aligned} \tag{D.6}$$

Combining the relations (D.3) and (D.5),

$$\forall\, t \in (t_1, t_2], \qquad \max\left(\widetilde{SoC}^{U}_{on}(t), \widetilde{SoC}^{U}_{off}(t)\right) < \widetilde{SoC}^{L}_{off}(t) + \Delta \tag{D.7}$$

while from (D.4) and (D.6),

$$\forall\, t \in (t_1, t_2], \qquad \max\left(\widetilde{SoC}^{U}_{on}(t), \widetilde{SoC}^{U}_{off}(t)\right) < \widetilde{SoC}^{L}_{on}(t) + \Delta \tag{D.8}$$

On applying (D.7) and (D.8), the relation (D.2b) is proven for the no switching case.

B. <u>Only ON-to-OFF switching (constantly) during $(t_1, t_2]$</u>

In this case,

$$\forall\, t \in (t_1, t_2], \quad \widetilde{SoC}^{U}_{on}(t) = \Delta^U(t), \text{ and, } \quad \widetilde{SoC}^{L}_{off}(t) > \Delta^L(t). \tag{D.9}$$

Thus,

$$\begin{aligned}\forall\, t \in (t_1, t_2], \quad \widetilde{SoC}^{L}_{on}(t) &= \widetilde{SoC}^{L}_{on}(t_1) + \alpha_{off}\,(t - t_1) \\ &\geq \widetilde{SoC}^{U}_{on}(t_1) - \Delta + \alpha_{off}\,(t - t_1) \qquad \text{[from (D.2a)]} \\ &> \widetilde{SoC}^{U}_{on}(t) - \Delta \end{aligned} \tag{D.10}$$

Because of constant switching at the upper boundary,

$$\begin{aligned}&\forall\, t \in (t_1, t_2], \\ &\widetilde{SoC}^{U}_{off}(t) = \max\left\{\widetilde{SoC}^{U}_{off}(t_1) + \alpha_{off}\,(t - t_1)\,,\ \Delta^{U}(t)\right\} \\ &\qquad \leq \max\left\{\widetilde{SoC}^{L}_{off}(t_1) + \Delta + \alpha_{off}\,(t - t_1)\,,\ \Delta^{U}(t)\right\} \qquad [\because (\text{D.}2a)] \\ &\qquad = \max\left\{\widetilde{SoC}^{L}_{off}(t_1) + \alpha_{off}\,(t - t_1)\,,\ \Delta^{L}(t)\right\} + \Delta \\ &\qquad = \widetilde{SoC}^{L}_{off}(t_1) + \alpha_{off}\,(t - t_1) + \Delta \qquad [\because (\text{D.9})] \\ &\qquad = \widetilde{SoC}^{L}_{off}(t) + \Delta \end{aligned} \tag{D.11}$$

Also,

$$\begin{aligned}&\forall\, t \in (t_1, t_2], \\ &\widetilde{SoC}^{U}_{off}(t) = \max\left\{\widetilde{SoC}^{U}_{off}(t_1) + \alpha_{off}\,(t - t_1)\,,\ \Delta^{U}(t)\right\} \\ &\qquad \leq \max\left\{\widetilde{SoC}^{L}_{on}(t_1) + \Delta + \alpha_{off}\,(t - t_1)\,,\ \Delta^{U}(t)\right\} \qquad [\because (\text{D.}2a)] \\ &\qquad = \max\left\{\widetilde{SoC}^{L}_{on}(t_1) + \alpha_{off}\,(t - t_1)\,,\ \Delta^{L}(t)\right\} + \Delta \\ &\qquad < \max\left\{\widetilde{SoC}^{L}_{on}(t),\ \Delta^{L}(t)\right\} + \Delta \qquad [\because \alpha_{off} < \alpha_{on}] \\ &\qquad = \widetilde{SoC}^{L}_{on}(t) + \Delta, \qquad \text{[applying (D.9) and (D.10)]} \end{aligned} \tag{D.12}$$

Combining (D.3), (D.10), (D.11) and (D.12), the relation (D.2b) is proven for the case when there is constant ON-to-OFF switching but no OFF-to-ON switching in the conerned time interval.

C. Only OFF-to-ON switching (constantly) during $(t_1, t_2]$

This situation is equivalent to the previous case (only ON-to-OFF switching), and can be treated similarly. For example, in this case,

$$\begin{aligned} \forall\, t \in (t_1, t_2], \quad & \widetilde{SoC}^{L}_{off}(t) = \Delta^L(t), \\ & \widetilde{SoC}^{U}_{on}(t) < \Delta^U(t), \\ \text{and,} \quad & \widetilde{SoC}^{L}_{on}(t) = \min\left\{\widetilde{SoC}^{L}_{on}(t_1) + \alpha_{on}\,(t - t_1)\,,\; \Delta^L(t)\right\} \end{aligned}$$

Following equivalent steps, (D.2b) can be proved for the case when there is constant OFF-to-ON switching, but no ON-to-OFF switching during $(t_1, t_2]$.

D. <u>Constant switching at both the boundaries during $(t_1, t_2]$</u>

In this case,

$$\forall\, t \in (t_1, t_2], \quad \widetilde{SoC}^{L}_{off}(t) = \Delta^L(t), \tag{D.13a}$$

$$\widetilde{SoC}^{U}_{on}(t) = \Delta^U(t), \tag{D.13b}$$

$$\widetilde{SoC}^{L}_{on}(t) = \min\left\{\widetilde{SoC}^{L}_{on}(t_1) + \alpha_{on}\,(t - t_1)\,,\; \Delta^L(t)\right\} \tag{D.13c}$$

$$\text{and,} \quad \widetilde{SoC}^{U}_{off}(t) = \max\left\{\widetilde{SoC}^{U}_{off}(t_1) + \alpha_{off}\,(t - t_1)\,,\; \Delta^U(t)\right\} \tag{D.13d}$$

Now,

$$\begin{aligned} & \widetilde{SoC}^{L}_{on}(t_1) \geq \widetilde{SoC}^{U}_{on}(t_1) - \Delta = \Delta^L(t_1) \qquad [\because \text{(D.2}a\text{) \& (D.13)}] \\ \text{and,} \quad & \widetilde{SoC}^{U}_{off}(t_1) \leq \widetilde{SoC}^{L}_{off}(t_1) + \Delta = \Delta^U(t_1) \end{aligned} \tag{D.14}$$

Hence from (D.13), $\widetilde{SoC}^{L}_{on}(t) \geq \Delta^L(t)$ and $\widetilde{SoC}^{U}_{off}(t) \leq \Delta^U(t)$, for all $t \in (t_1, t_2]$. Rest of the proof of the relation (D.2b) for $t \in (t_1, t_2]$ follows trivially.

Thus for all possible scenarios, it can be proved that if the width of the span of SoCs is less than $\Delta$ at the start of the time interval $[t_1, t_2]$, then the same is true for the rest of time interval as well. Hence the Theorem V.1 is proved by considering the time interval $[t_0, \infty)$ as a summation of many such sub-intervals in each of which the relation holds.

$\square$

# APPENDIX E

# Proof of the Theorem VI.1

It is assumed, for simplicity, that $V_0$ is set by some external method and hence is beyond the regime of local control action. From (6.3) and (6.5a), it can be written

$$\frac{\partial Q_j}{\partial q_k^g} = \begin{cases} 0, & k \leq j \\ -1, & k \geq j+1 \end{cases} \tag{E.1a}$$

$$\text{and,} \quad \frac{\partial \Delta V_j}{\partial q_k^g} = -\sum_{i=0}^{j-1} x_i \frac{\partial Q_i}{\partial q_k^g} = -\sum_{i=0}^{\min(j,k)-1} x_i \frac{\partial Q_i}{\partial q_k^g} \tag{E.1b}$$

where the second equality in (E.1b) follows from (E.1a). Furthermore,

$$\frac{\partial \left(\Delta V_j^{eff}\right)^2}{\partial q_k^g} = 2\Delta V_j^{eff} \frac{\partial \Delta V_j}{\partial q_k^g}, \quad \forall\, j \geq 0, \forall\, k \geq 1. \tag{E.2}$$

*Note: From the definition (6.5a),(6.5b),*

$$\forall j \geq 0, k \geq 1,$$

$$\frac{\partial \left(\Delta V_j^{eff}\right)^2}{\partial q_k^g} = 2\Delta V_j^{eff} \frac{\partial \Delta V_j^{eff}}{\partial q_k^g} = \begin{cases} 0, & |\Delta V_j| \leq V_{sl} \\ 2(\Delta V_j - V_{sl})\frac{\partial \Delta V_j}{\partial q_k^g}, & \Delta V_j > V_{sl} \\ 2(\Delta V_j + V_{sl})\frac{\partial \Delta V_j}{\partial q_k^g}, & \Delta V_j < -V_{sl} \end{cases}$$

*But it also follows directly from (6.5b) that,*

$$\forall j \geq 0, k \geq 1, \quad 2\Delta V_j^{eff} \frac{\partial \Delta V_j}{\partial q_k^g} = \begin{cases} 0, & |\Delta V_j| \leq V_{sl} \\ 2(\Delta V_j - V_{sl})\frac{\partial \Delta V_j}{\partial q_k^g}, & \Delta V_j > V_{sl} \\ 2(\Delta V_j + V_{sl})\frac{\partial \Delta V_j}{\partial q_k^g}, & \Delta V_j < -V_{sl} \end{cases}$$

*Hence the relation (*E.2*) holds.*

The optimal values of $q_j^g$ are given by the stationary points of (6.6),

$$f_k := \frac{\partial \mathcal{M}\left(q_{j\geq 1}^g; V_0\right)}{\partial q_k^g} = 0, \quad \forall k = \{1, 2, \ldots, N\} \tag{E.3a}$$

which implies

$$\begin{aligned} f_k &= 2\left(\sum_{j=1}^{N} \beta_j \Delta V_j^{eff} \frac{\partial \Delta V_j}{\partial q_k^g} + \sum_{j=0}^{N-1} r_j Q_j \frac{\partial Q_j}{\partial q_k^g}\right) \\ &= 2\left(-\sum_{j=1}^{N} \beta_j \Delta V_j^{eff} \sum_{i=0}^{\min(j,k)-1} x_i \frac{\partial Q_i}{\partial q_k^g} - \sum_{j=0}^{k-1} r_j Q_j\right) \\ &= 0, \quad \forall\, k \geq 1. \end{aligned} \tag{E.3b}$$

Optimal $q_N^g$ can be solved using $f_N$ and $f_{N-1}$. From (E.3b), $f_N - f_{N-1} = 0$ implies,

$$-2\beta_N \Delta V_N^{eff} \left(\sum_{i=0}^{N-1} x_i \frac{\partial Q_i}{\partial q_N^g} - \sum_{i=0}^{N-2} x_i \frac{\partial Q_i}{\partial q_{N-1}^g}\right) - 2r_{N-1} Q_{N-1} = 0$$

and using (E.1a) gives,

$$\beta_N \Delta V_N^{eff} \left(\sum_{i=0}^{N-1} x_i - \sum_{i=0}^{N-2} x_i\right) - r_{N-1} Q_{N-1} = 0$$

$$\Rightarrow \quad Q_{N-1} = \frac{x_{N-1}}{r_{N-1}} \beta_N \Delta V_N^{eff} \tag{E.4a}$$

$$\Rightarrow \quad q_N^g = q_N^c - \frac{x_{N-1}}{r_{N-1}} \beta_N \Delta V_N^{eff} \tag{E.4b}$$

where the final step follows from (6.3). Thus the optimal $q_N^g$ can be computed using only the local $V_N$ and $q_N^c$, and satisfies the control law in (6.7) with $\alpha = x_{N-1}/r_{N-1}$.

The remainder of the proof follows from induction. It will be shown that if there exists an $M \in \{1, 2, \ldots, N-1\}$ such that for all $k \geq M+1$,

$$q_k^q = q_k^c - \frac{x_{k-1}}{r_{k-1}} \beta_k \Delta V_k^{eff} \tag{E.5a}$$

then,

$$q_M^q = q_M^c - \frac{x_{M-1}}{r_{M-1}} \beta_M \Delta V_M^{eff}. \tag{E.5b}$$

It has already been shown in (E.4b) that there is an $M = N - 1$ for which (E.5a) holds. To prove (E.5b), refer back to (E.3b), from which $f_M - f_{M-1} = 0$ implies,

$$-2\sum_{j=M}^{N}\beta_j \Delta V_j^{eff}\left(\sum_{i=0}^{M-1} x_i \frac{\partial Q_i}{\partial q_M^g} - \sum_{i=0}^{M-2} x_i \frac{\partial Q_i}{\partial q_{M-1}^g}\right) - 2r_{M-1}Q_{M-1} = 0.$$

Using (E.1a), this gives,

$$Q_{M-1} = \frac{x_{M-1}}{r_{M-1}} \sum_{j=M}^{N} \beta_j \Delta V_j^{eff}$$

and hence from (6.3),

$$\begin{aligned} \sum_{j=M}^{N}\left(q_j^c - q_j^g\right) &= \frac{x_{M-1}}{r_{M-1}} \sum_{j=M}^{N} \beta_j \Delta V_j^{eff} \\ \Rightarrow \quad q_M^g &= q_M^c - \frac{x_{M-1}}{r_{M-1}} \beta_M \Delta V_M^{eff} \end{aligned} \tag{E.6}$$

where the final step makes use of (E.5a) and (6.8). Hence the claim in (E.5) is proved. The claim (E.5) together with (E.4b) complete the proof that each optimal $q_j^g$ can be computed by observing local variables $V_j$ and $q_j^c$, and its optimal value is given by (6.7) with $\alpha = x_{j-1}/r_{j-1}$.

This concludes the proof of Theorem VI.1.

# APPENDIX F

# Deriving the optimal solutions in (6.21)

From (6.17c) and (6.16),

$$V_{i+1}\frac{\partial V_{i+1}}{\partial q_k} = -\sum_{j=0}^{\min(i,k-1)} x_j \frac{\partial Q_j}{\partial q_k}, \qquad \forall\, i \in \{0,1,2,\ldots,N-1\}, \forall\, k \in K \tag{F.1}$$

Following similar steps as in (E.2), and using (F.1) and the definition (6.5a),

$$\begin{aligned}&\forall\, i \in \{0,1,2,\ldots,N-1\}, \forall\, k \in K,\\ &\Delta V_{i+1}^{eff}\frac{\partial \Delta V_{i+1}^{eff}}{\partial q_k} = \Delta V_{i+1}^{eff}\frac{\partial V_{i+1}}{\partial q_k} = -\frac{\Delta V_{i+1}^{eff}}{V_{i+1}}\sum_{j=0}^{\min(i,k-1)} x_j \frac{\partial Q_j}{\partial q_k}\end{aligned} \tag{F.2}$$

Moreover from the definition of $f_i$'s in (6.20),

$$\begin{aligned} f_i &= 2\sum_{j=0}^{N-1}\left(\beta_{j+1}\Delta V_{j+1}^{eff}\frac{\partial \Delta V_{j+1}^{eff}}{\partial q_{k_i}} + r_j\left(P_j\frac{\partial P_j}{\partial q_{k_i}} + Q_j\frac{\partial Q_j}{\partial q_{k_i}}\right)\right)\\ &= 2\left(-\sum_{j=0}^{N-1}\frac{\beta_{j+1}\Delta V_{j+1}^{eff}}{V_{j+1}}\sum_{n=0}^{\min(j,k_i-1)} x_n + \sum_{j=0}^{k_i-1} r_j Q_j\right) \qquad [\because \text{ (F.2) \& (6.16)}]\end{aligned} \tag{F.3}$$

and hence using $f_m - f_{m-1} = 0$, derived from (6.20), the following is obtained,

$$\begin{aligned}&\sum_{j=0}^{k_m-1} r_j Q_j - \sum_{j=0}^{k_{(m-1)}-1} r_j Q_j = \sum_{j=0}^{N-1}\frac{\beta_{j+1}\Delta V_{j+1}^{eff}}{V_{j+1}}\left(\sum_{n=0}^{\min(j,k_m-1)} x_n - \sum_{n=0}^{\min(j,k_{m-1}-1)} x_n\right)\\ &\implies \sum_{j=k_{m-1}}^{k_m-1} r_j Q_j = \sum_{j=k_{m-1}}^{N-1}\frac{\beta_{j+1}\Delta V_{j+1}^{eff}}{V_{j+1}}\sum_{n=k_{m-1}}^{\min(j,k_m-1)} x_n\end{aligned} \tag{F.4}$$

Using the relations (6.17b) and (F.4),

$$\begin{aligned}
&\sum_{j=k_{m-1}}^{N-1}\left(x_jP_j^2+q_{j+1}\right)\sum_{n=k_{m-1}}^{\min(j,k_m-1)} r_n = \sum_{j=k_{m-1}}^{N-1}\frac{\beta_{j+1}\Delta V_{j+1}^{eff}}{V_{j+1}}\sum_{n=k_{m-1}}^{\min(j,k_m-1)} x_n \\
&\implies q_{k_m} = -x_{k_m-1}P_{k_m-1}^2 - \sum_{j=k_{m-1}}^{k_m-2}\left(x_jP_j^2+q_{j+1}\right)\left(\frac{\sum_{n=k_{m-1}}^{j} r_n}{\sum_{n=k_{m-1}}^{k_m-1} r_n}\right) \\
&\qquad - \sum_{j=k_m}^{N-1}\left(x_jP_j^2+q_{j+1}\right) + \sum_{j=k_{m-1}}^{k_m-2}\frac{\beta_{j+1}\Delta V_{j+1}^{eff}}{V_{j+1}}\left(\frac{\sum_{n=k_{m-1}}^{j} x_n}{\sum_{n=k_{m-1}}^{k_m-1} r_n}\right) \\
&\qquad + \gamma_{m-1}\sum_{j=k_m-1}^{N-1}\frac{\beta_{j+1}\Delta V_{j+1}^{eff}}{V_{j+1}} \qquad \text{[using (6.18)]} \qquad \text{(F.5)}
\end{aligned}$$

Similarly the optimal value of $q_{k_{m-1}}$ can be solved as,

$$\begin{aligned}
&f_{m-1} - f_{m-2} = 0 \\
&\implies \sum_{j=k_{m-2}}^{k_{m-1}-1} r_jQ_j = \sum_{j=k_{m-2}}^{N-1}\frac{\beta_{j+1}\Delta V_{j+1}^{eff}}{V_{j+1}}\sum_{n=k_{m-2}}^{\min(j,k_{m-1}-1)} x_n \qquad \text{[from (F.4)]} \\
&\implies \sum_{j=k_{m-2}}^{N-1}\left(x_jP_j^2+q_{j+1}\right)\sum_{n=k_{m-2}}^{\min(j,k_{m-1}-1)} r_n = \sum_{j=k_{m-2}}^{N-1}\frac{\beta_{j+1}\Delta V_{j+1}^{eff}}{V_{j+1}}\sum_{n=k_{m-2}}^{\min(j,k_{m-1}-1)} x_n \\
&\implies q_{k_{m-1}} = -x_{k_{m-1}-1}P_{k_{m-1}-1}^2 - \sum_{j=k_{m-2}}^{k_{m-1}-2}\left(x_jP_j^2+q_{j+1}\right)\left(\frac{\sum_{n=k_{m-2}}^{j} r_n}{\sum_{n=k_{m-2}}^{k_{m-1}-1} r_n}\right) \\
&- \sum_{j=k_{m-1}}^{k_m-2}\left(x_jP_j^2+q_{j+1}\right)\left(\frac{\sum_{n=j+1}^{k_m-1} r_n}{\sum_{n=k_{m-1}}^{k_m-1} r_n}\right) \\
&+ \sum_{j=k_{m-2}}^{k_{m-1}-1}\frac{\beta_{j+1}\Delta V_{j+1}^{eff}}{V_{j+1}}\left(\frac{\sum_{n=k_{m-2}}^{j} x_n}{\sum_{n=k_{m-2}}^{k_{m-1}-1} r_n}\right) \\
&+ \sum_{j=k_{m-1}}^{k_m-2}\frac{\beta_{j+1}\Delta V_{j+1}^{eff}}{V_{j+1}}\left(\gamma_{m-2} - \frac{\sum_{n=k_{m-1}}^{j} x_n}{\sum_{n=k_{m-1}}^{k_m-1} r_n}\right) \\
&+ \left(\gamma_{m-2} - \gamma_{m-1}\right)\sum_{j=k_m-1}^{N-1}\frac{\beta_{j+1}\Delta V_{j+1}^{eff}}{V_{j+1}} \qquad \text{(F.6)}
\end{aligned}$$

Continuing this way, all the optimal values $q_{k_i}$ $\forall i \in \{1, 2, \ldots, m\}$, can be computed as summarized in (6.21).

# BIBLIOGRAPHY

# BIBLIOGRAPHY

[1] "Annual Energy Outlook 2012 Early Release," *U.S. Energy Information Administration*, Feb. 2012.

[2] "Annual Energy Outlook 2011," *U.S. Energy Information Administration*, Apr. 2011.

[3] "IEA Key World Energy Statistics 2011," *International Energy Agency*, Oct. 2011.

[4] "Annual Energy Outlook 2010," *U.S. Energy Information Administration*, Apr. 2010.

[5] "Sixth Northwest Conservation and Electric Power Plan," *Northwest Power and Conservation Council*, Feb. 2010.

[6] "Annual Energy Review 2011," *U.S. Energy Information Administration*, Oct. 2011.

[7] "Renewable energy: Growth and challenges in the electric power industry," *Edison Electric Institute*, 2008.

[8] G. Sinden, "Assessing the costs of intermittent power generation," UK Energy Research Centre (Online material: http://www.ukerc.ac.uk/Downloads/PDF/05/050705TPASindenpres.pdf), July 2005.

[9] Kuntz, Mark T. and Justin Dawe, "Renewable. Rechargeable. Remarkable.," in *VRB Power Systems*, Mechanical Engineering, 2005.

[10] E. S. Huse, "Power generation scheduling: A free market based procedure with reserve constraints included," *PhD Dissertation*, 1998.

[11] "Integration of renewable resources: Operational requirements and generation fleet capability at 20% RPS," *California ISO*, Aug. 2010.

[12] G. Strbac, "Demand side management: Benefits and challenges," *Energy Policy*, vol. 36, pp. 4419–4426, Aug. 2008.

[13] M. Klobasa, "Analysis of demand response and wind integration in Germanys electricity market," *IET Renewable Power Generation*, vol. 4, no. 1, pp. 55–63, 2010.

[14] Heffner G., Goldman C., Kirby B. J., and Kintner-Meyer M., "Loads providing ancillary services: Review of international experience," *Lawrence Berkeley National Laboratory, Berkeley*, 2007.

[15] "2005 Residential Energy Consumption Survey," *U.S. Energy Information Administration*, 2005.

[16] B. Kirby, J. Kueck, T. Laughner, and K. Morris, "Spinning reserve from hotel load response," *Electricity Journal*, vol. 21, Dec. 2008.

[17] B. Kirby, "Load response fundamentally matches power system reliability requirements," *IEEE Power Engineering Society General Meeting*, June 2007.

[18] B. Kirby, "Spinning reserve from responsive loads," *Technical Report ORNL/TM-2003/19, Oak Ridge National Laboratory, USA*, Mar. 2003.

[19] Chellury Sastry, Viraj Srivastava, Rob Pratt, and Shun Li, "Use of residential smart appliances for peak-load shifting and spinning reserves: Cost/benefit analysis," Dec. 2010.

[20] A. Damon, "Smart meters spawn conspiracy talk: They know what you're watching on TV," *Las Vegas SUN*, Mar. 2012.

[21] "Stop smart meters: The film," (Online material: http://www.stopsmartmetersnow.com/?p=132), Mar. 2012.

[22] "Big brother: The insidious smart meter," *Radio Patriot (Online material: http://radiopatriot.wordpress.com/2011/07/10/big-brother-the-insidious-smart-meter/)*, July 2011.

[23] "No more privacy: Smart meters are surveillance devices that monitor the behavior in your home every single minute of every single day," in *The American Dream (Online material: http://endoftheamericandream.com/archives/no-more-privacy-smart-meters-are-surveillance-devices-that-monitor-the-behavior-in-your-home-every-single-minute-of-every-single-day).*

[24] S. Ihara and F. C. Schweppe, "Physically based modelling of cold load pickup," *IEEE Transactions on Power Apparatus and Systems*, vol. 100, pp. 4142–4150, Sept. 1981.

[25] C. Y. Chong and A. S. Debs, "Statistical synthesis of power system functional load models," *Proceedings of the 18th IEEE Conference on Decision and Control*, vol. 18, pp. 264–269, Dec. 1979.

[26] R. Malhamé and C. Y. Chong, “Electric load model synthesis by diffusion approximation of a high-order hybrid-state stochastic system,” *IEEE Transactions on Automatic Control*, vol. 30, pp. 854–860, Sept. 1985.

[27] R. E. Mortensen and K. P. Haggerty, “A stochastic computer model for heating and cooling loads,” *IEEE Transactions on Power Systems*, vol. 3, pp. 1213–1219, Aug. 1988.

[28] C. Uçak and R. Çağlar, “The effects of load parameter dispersion and direct load control actions on aggregated load,” *POWERCON’98*, vol. 1, pp. 280–284, 1998.

[29] D. S. Callaway, “Tapping the energy storage potential in electric loads to deliver load following and regulation, with application to wind energy,” *Energy Conversion and Management*, vol. 50, pp. 1389–1400, May 2009.

[30] D. Angeli and A. Astolfi, “A stochastic approach to distributed power frequency control by means of smart appliances,” in *Decision and Control (CDC), 2012 IEEE 51st Annual Conference on*, pp. 6896–6901, 2012.

[31] F. Koch, J. L. Mathieu, and D. S. Callaway, “Modeling and control of aggregated heterogeneous thermostatically controlled loads for ancillary services,” *17th Power Systems Computations Conference*, 2011.

[32] J. L. Mathieu and D. Callaway, “State estimation and control of heterogeneous thermostatically controlled loads for load following,” *Hawaii International Conference on System Sciences*, pp. 2002–2011, 2012.

[33] S. Bashash and H. K. Fathy, “Modeling and control insights into demand-side energy management through setpoint control of thermostatic loads,” *American Control Conference*, pp. 4546 – 4553, 2011.

[34] C. Perfumo, E. Kofman, J. H. Braslavsky, and J. K. Ward, “Load management: Model-based control of aggregate power for populations of thermostatcally controlled loads,” *Energy Conversion and Management*, vol. 55, pp. 36–48, Mar. 2012.

[35] M. Book, X. Mosquet, G. Sticher, M. Groll, and D. Rizoulis, “The comeback of the electric car? How real, how soon, and what must happen next,” *Focus Report, Boston Consulting Group*, Jan. 2009.

[36] R. Lache, D. Galves, and P. Nolan, “Electric cars: Plugged in,” *Autos Research Team, Deutsche Bank*, June 2008.

[37] S. Hadley, “Impact of plug-in hybrid vehicles on the electric grid,” in *Tech. Rep. ORNL/TM-2006/554*, Oak Ridge Nat. Lab., Oak Ridge, TN, Oct. 2006.

[38] Z. Ma, D. Callaway, and I. A. Hiskens, "Decentralized charging control for large populations of plug-in electric vehicles," in *49th IEEE Conference on Decision and Control*, 2010.

[39] "Fault-induced delayed voltage recovery," *NERC Technical Reference Paper, Transmission Issues Subcommittee*, Dec. 2008.

[40] P. Fairley, "Speed bumps ahead for electric-vehicle charging," *Spectrum, IEEE*, vol. 47, no. 1, pp. 13–14, 2010.

[41] L. Kelly, A. Rowe, and P. Wild, "Analyzing the impacts of plug-in electric vehicles on distribution networks in british columbia," in *Electrical Power Energy Conference (EPEC), 2009 IEEE*, pp. 1–6, 2009.

[42] E. Sortomme, M. Hindi, S. MacPherson, and S. Venkata, "Coordinated charging of plug-in hybrid electric vehicles to minimize distribution system losses," *Smart Grid, IEEE Transactions on*, vol. 2, no. 1, pp. 198–205, 2011.

[43] K. Clement-Nyns, E. Haesen, and J. Driesen, "The impact of charging plug-in hybrid electric vehicles on a residential distribution grid," *IEEE Transactions on Power Systems*, vol. 25, no. 1, pp. 371–380, 2010.

[44] P. Richardson, D. Flynn, and A. Keane, "Optimal charging of electric vehicles in low-voltage distribution systems," *IEEE Transactions on Power Systems*, vol. 27, no. 1, pp. 268–279, 2012.

[45] A. O'Connell, D. Flynn, P. Richardson, and A. Keane, "Controlled charging of electric vehicles in residential distribution networks," in *Innovative Smart Grid Technologies (ISGT Europe), 2012 3rd IEEE PES International Conference and Exhibition on*, pp. 1–7, 2012.

[46] S. Deilami, A. Masoum, P. Moses, and M. A. S. Masoum, "Real-time coordination of plug-in electric vehicle charging in smart grids to minimize power losses and improve voltage profile," *IEEE Transactions on Smart Grid*, vol. 2, no. 3, pp. 456–467, 2011.

[47] R. Verzijlbergh, M. Grond, Z. Lukszo, J. Slootweg, and M. Ilic, "Network impacts and cost savings of controlled EV charging," *IEEE Transactions on Smart Grid*, vol. 3, no. 3, pp. 1203–1212, 2012.

[48] R. Hermans, M. Almassalkhi, and I. Hiskens, "Incentive-based coordinated charging control of plug-in electric vehicles at the distribution-transformer level," in *American Control Conference (ACC), 2012*, pp. 264–269, 2012.

[49] G. C. Chargers, “Aerovironment licenses pnnl ev smart charger controller technology,” *(http://www.greencarcongress.com/2013/03/pnnl-20130306.html)*, mar 2013.

[50] P. Denholm and W. Short, “An evaluation of utility system impacts and benefits of optimality dispatched plug-in hybrid vehicles,” in *Technical Report NREL-TP-620-40293*, National Renewable Energy Laboratory, USA, Oct. 2006.

[51] C. Roe, F. Evangelos, J. Meisel, S. Meliopoulos, and T. Overbye, “Power system level impacts of PHEVs,” in *42nd Hawaii International Conference on System Sciences*, 2009.

[52] D. S. Callaway and I. A. Hiskens, “Achieving controllability of electric loads,” *Proceedings of IEEE*, vol. 99, pp. 184–199, Jan. 2011.

[53] C.-T. Li, C. Ahn, H. Peng, and J. Sun, “Decentralized charging of plug-in electric vehicles,” in *Proceedings of the ASME 2011 Dynamic Systems and Control Conference*, pp. 1–5, oct 2011.

[54] L. Zhu, F. Yu, B. Ning, and T. Tang, “Optimal charging control for electric vehicles in smart microgrids with renewable energy sources,” in *Vehicular Technology Conference (VTC Spring), 2012 IEEE 75th*, pp. 1–5, 2012.

[55] L. Gan, U. Topcu, and S. H. Low, “Optimal decentralized protocols for electric vehicle charging,” in *50th IEEE Conference on Decision and Control*, 2011.

[56] Z. Yuan, H. Xu, H. Han, and Y. Zhao, “Research of smart charging management system for electric vehicles based on wireless communication networks,” in *Information and Automation for Sustainability (ICIAfS), 2012 IEEE 6th International Conference on*, pp. 242–247, 2012.

[57] U. Reiner, C. Elsinger, and T. Leibfried, “Distributed self organising electric vehicle charge controller system: Peak power demand and grid load reduction with adaptive ev charging stations,” in *Electric Vehicle Conference (IEVC), 2012 IEEE International*, pp. 1–6, 2012.

[58] G. Jóos, B. Ooi, D. McGillis, F. Galiana, and R. Marceau, “The potential of distributed generation to provide ancillary services,” in *Proc. IEEE PES Summer Meeting*, vol. 3, pp. 1762–1767, 2000.

[59] A. F. Povlsen, “Impacts of power penetration from photovoltaic power systems in distribution networks,” *International Energy Agency*, Feb. 2002.

[60] M. A. Kashem and G. Ledwich, “Multiple distributed generators for distribution feeder voltage support,” *IEEE Transactions on Energy Conversion*, vol. 20, pp. 676–684, Sept. 2005.

[61] A. Woyte, V. V. Thong, R. Belmans, and J. Nijs, "Voltage fluctuations on distribution level introduced by photovoltaic systems," *IEEE Transactions on Energy Conversion*, vol. 21, pp. 202–209, Mar. 2006.

[62] J. V. Paatero and P. D. Lund, "Effects of large-scale photovoltaic power integration on electricity distribution networks," *Renewable Energy*, vol. 32, pp. 216–234, Feb. 2007.

[63] M. Prodanovic, K. De Brabandere, J. Van Den Keybus, T. Green, and J. Driesen, "Harmonic and reactive power compensation as ancillary services in inverter-based distributed generation," *Generation, Transmission Distribution, IET*, vol. 1, no. 3, pp. 432–438, 2007.

[64] "IEEE 1547 Standard for Interconnecting Distributed Resources With Electric Power Systems," Online material: http://grouper.ieee.org/groups/scc21/1547/1547_index.html.

[65] A. Dimeas and N. Hatziargyriou, "Operation of a multiagent system for microgrid control," *IEEE Transactions on Power Systems*, vol. 20, no. 3, pp. 1447–1455, 2005.

[66] M. Baran and I. El-Markabi, "A multiagent-based dispatching scheme for distributed generators for voltage support on distribution feeders," *IEEE Transactions on Power Systems*, vol. 22, pp. 52–59, Feb. 2007.

[67] A. D. Dominguez-Garcia and C. N. Hadjicostis, "Coordination and control of distributed energy resources for provision of ancillary services," in *2010 First IEEE International Conference on Smart Grid Communications*, pp. 537–542, 2010.

[68] K. Turitsyn, P. Sulc, S. Backhaus, and M. Chertkov, "Distributed control of reactive power flow in a radial distribution circuit with high photovoltaic penetration," in *IEEE Power and Energy Society General Meeting*, pp. 1–6, July 2010.

[69] K. Turitsyn, P. Sulc, S. Backhaus, and M. Chertkov, "Options for control of reactive power by distributed photovoltaic generators," in *Proceedings of the IEEE*, vol. 99, pp. 1063–1073, 2011.

[70] S. Bolognani and S. Zampieri, "Distributed control for optimal reactive power compensation in smart microgrids," in *Decision and Control and European Control Conference (CDC-ECC), 2011 50th IEEE Conference on*, pp. 6630–6635, 2011.

[71] B. D. O. Anderson and J. B. Moore, *Optimal Control: Linear Quadratic Methods*. Prentice-Hall, 1990.

[72] S. Kundu and N. Sinitsyn, "Safe protocol for controlling power consumption by a heterogeneous population of loads," *American Control Conference*, 2012.

[73] S. Kundu and I. A. Hiskens, “Hysteresis-based charging control of plug-in electric vehicles,” *51st IEEE Conference on Decision and Control*, Dec. 2012.

[74] H. K. Khalil, *Nonlinear Systems.* Prentice-Hall, 3 ed., 2002.

[75] Z. Ma, D. S. Callaway, and I. A. Hiskens, “Decentralized charging control of large populations of plug-in electric vehicles,” *IEEE Transactions on Control Systems Technology*, vol. 21, pp. 67–78, jan 2013.

[76] “Power quality requirements for plug-in electric vehicle chargers,” *SAE International Surface Vehicle Recommended Practice J2894-1*, Dec. 2011.

[77] “EV charging equipment operational recommendations for power quality,” *Electric Power Research Institute Final Report TR-109023*, Nov. 1997.

[78] D. Kosterev, A. Meklin, J. Undrill, B. Lesieutre, W. Price, D. Chassin, R. Bravo, and S. Yang, “Load modeling in power system studies: WECC progress update,” in *Proceedings of the IEEE Power and Energy Society General Meeting*, July 2008.

[79] C. A. Colopy, *Chapter 8: Electric Power Transformer Engineering, Second Edition.* CRC Press, May 2007.

[80] *Inverse time delay on LTC/regulator controls (Tapchanger controls: Application note #29).* Beckwith Electric Co. Inc., Sept. 2007.

[81] J. H. Harlow, “Load tap changing control.” National Rural Electric Cooperative Association, Mar. 1996.

[82] G. Price, “A generalized circle diagram approach for global analysis of transmission system performance,” *IEEE Transactions on Power Apparatus and Systems*, pp. 2881–2890, Oct. 1984.

[83] I. Hiskens and R. Davy, “Exploring the power flow solution space boundary,” *IEEE Transactions on Power Systems*, vol. 16, pp. 389–395, Aug. 2001.

[84] I. T. F. Report, “Standard load models for power flow and dynamic performance simulation,” *IEEE Transactions on Power Systems*, vol. 10, p. 13021313, Aug. 1995.

[85] M. Baran and F. Wu, “Optimal sizing of capacitors placed on a radial distribution system,” *IEEE Transactions on Power Delivery*, vol. 4, p. 735743, Jan. 1989.

[86] “Voltage tolerance boundary,” *Pacific Gas & Electric Company*, Jan. 1999.

[87] J. Grainger and S. Lee, “Optimum size and location of shunt capacitors for reduction of losses on distribution feeders,” *IEEE Transactions on Power Apparatus and Systems*, pp. 1105–1118, Mar. 1981.

[88] W. Kersting, *Distribution System Modeling and Analysis.* CRC Press, 2002.

[89] H. Willis, *Power Distribution Planning Reference Book.* CRC Press, 2 ed., 2004.

[90] M. Baran and F. Wu, "Optimal capacitor placement on radial distribution systems," *IEEE Transactions on Power Delivery*, vol. 4, p. 725734, Jan. 1989.

[91] M. Grant and S. Boyd, "CVX: Matlab software for disciplined convex programming," *Version 1.21, Build 808*, Apr. 2011.

[92] W. Kersting, "Radial distribution test feeders," in *Proceedings of the IEEE Power Engineering Society Winter Meeting*, vol. 2, pp. 908–912, Jan. 2001.

[93] C. Garcia and W. Zangwill, *Pathways to Solutions, Fixed Points and Equilibria*. Englewood Cliffs, NJ: Prentice Hall, 1981.

[94] S. Kundu, N. Sinitsyn, S. Backhaus, and I. A. Hiskens, "Modeling and control of thermostatically-controlled-loads," *17th Power Systems Computations Conference*, 2011.

[95] E. Liu and J. Bebic, "Distribution system voltage performance analysis for high-penetration photovoltaics," *NREL/SR-581-42298, Tech. Rep.*, Apr. 2008.

[96] K. Turitsyn, P. Sulc, S. Backhaus, and M. Chertkov, "Local control of reactive power by distributed photovoltaic generators," in *1st IEEE Internationl Conference on Smart Grid Communications*, pp. 79–84, 2010.

[97] "IEEE 34 node test feeder." Distribution System Analysis Subcommittee, IEEE Power and Energy Society, ewh.ieee.org/soc/pes/dsacom/testfeeders/index.html, Sept. 2010.

[98] I. Paprotny, E. Leland, C. Sherman, R. M. White, and P. K. Wright, "Self-powered MEMS sensor module for measuring electrical quantities in residential, commercial, distribution and transmission power systems," in *The 2010 IEEE Energy Conversion Congress and Exposition (ECCE)*, 2010.

[99] M. E. Baran and A. W. Kelley, "State estimation for real-time monitoring of distribution systems," *IEEE Transactions on Power Systems*, vol. 9, pp. 1601 – 1609, Aug. 1994.

[100] A. K. Ghosh, D. L. Lubkeman, and R. H. Jones, "Load modeling for distribution circuit state estimation," *IEEE Transactions on Power Delivery*, vol. 12, pp. 999 –1005, apr 1997.

[101] H. C. Kuo and Y. Y. Hsu, "Distribution system load estimation and service restoration using a fuzzy set approach," *IEEE Transactions on Power Delivery*, vol. 8, pp. 1950 –1957, oct 1993.